

Summer 8-13-2021

Dynamics of Protein-DNA Interactions Characterized by Atomic Force Microscopy

Yaqing Wang
University of Nebraska Medical Center

Tell us how you used this information in this [short survey](#).

Follow this and additional works at: <https://digitalcommons.unmc.edu/etd>

 Part of the [Biophysics Commons](#), and the [Pharmacy and Pharmaceutical Sciences Commons](#)

Recommended Citation

Wang, Yaqing, "Dynamics of Protein-DNA Interactions Characterized by Atomic Force Microscopy" (2021).
Theses & Dissertations. 572.
<https://digitalcommons.unmc.edu/etd/572>

This Dissertation is brought to you for free and open access by the Graduate Studies at DigitalCommons@UNMC. It has been accepted for inclusion in Theses & Dissertations by an authorized administrator of DigitalCommons@UNMC. For more information, please contact digitalcommons@unmc.edu.

DYNAMICS OF PROTEIN-DNA INTERACTIONS CHARACTERIZED BY ATOMIC FORCE MICROSCOPY

by

Yaqing Wang

A DISSERTATION

Presented to the Faculty of
the University of Nebraska Graduate College
in Partial Fulfillment of the Requirements
for the Degree of Doctor of Philosophy

Pharmaceutical Sciences Graduate Program

Under the Supervision of Professor Yuri L. Lyubchenko

University of Nebraska Medical Center
Omaha, Nebraska

July, 2021

Supervisory Committee:

Tatiana Bronich, PhD

Gloria Borgstahl, PhD

Don Ronning, PhD

Luis Marky, PhD

Dedicated to my parents

And grandparents

For their unconditional love and encouragement.

ACKNOWLEDGMENTS

This work would not have been possible without the help, support, and guidance of many people. First and foremost, I would like to thank my advisor, Yuri Lyubchenko, for his support, encouragement, and guidance throughout my research work. I am grateful for the opportunity to work on exciting and challenging projects. He saw my potential as a beginner in academic research and has helped me develop as an independent scientist. His motivation and encouragement have been instrumental in producing all the work, including this dissertation. I would not have received the postdoctoral training opportunities without his inspiration and support. I am sure that his efforts will continue to influence my life, both within and beyond science, for many years to come.

I would extend my gratitude to the members of my supervisory committee, Tatiana Bronich, Gloria Borgstahl, Luis Marky, and Don Ronning, for their expert guidance and constructive criticism. I would also like to thank Piero Bianco, our collaborator, for his generosity in sharing the proteins with us and his suggestions for my research projects. My sincere gratitude to Tatiana Bronich and Piero Bianco. They were always willing and ready when I bothered them for letters of recommendation. I got many opportunities because of their letters, and I cannot thank them enough.

I am grateful to all past and present members in the Lyubchenko lab for their friendship, guidance, support, and encouragement during my graduate journey, especially Lyudmila Shlyakhtenko, Siddhartha Banerjee, Sibaprasad Maity, Yuliang Zhang, Mohtadin Hashemi, Zhiqiang Sun, Karen Zagorski, Tommy Stormberg, Shaun Filliaux, and Sridhar Vemulapalli. I will miss the group meetings, journal clubs, movie nights, lunch

breaks, and parties. I would like to express my sincere gratitude to Luda, who has always been patient with me and guided me through my studies. There were days, I found myself frustrated with life and work, but she was always there to listen, never judged, and offered her invaluable advice. I will always cherish our conversations. I would also like to thank Zhiqiang Sun for his instructions in protocol development, AFM imaging, and manuscript revisions, which helped bring this dissertation into existence.

I would like to thank all my friends who made my life in Omaha enjoyable and memorable, including Yuanyuan Sun, Damian Daszynski, Bowen Qi, Xiaoxiao Qi, Sarah Li, and Jennifer Ye. A special thank you to the UNMC Graduate Studies and Department of Pharmaceutical Sciences, especially to Renee Kaszynski and Cody Phillips, for their assistance.

I would like to acknowledge the National Institute of Health funding sources for making my research possible. Furthermore, I would like to thank the China Scholarship Council for providing financial support during my research.

I would like to express my sincere gratitude to my best friends Xiaolin Jiang, Chen Dong, and Lijin Yang. Their drive and hard work motivated me throughout this journey. I have shared difficult moments and celebrated successes with them, and I feel lucky to have friends turned family.

Last but certainly not least, I would like to thank all my family. I am forever grateful to my parents, Minghui Zhuang and Liguang Wang, for their unconditional love, never-ending support, and constant encouragement. I admire my grandparents, who have lived through tough times and truly know the meaning of grit and kindness.

DYNAMICS OF PROTEIN-DNA INTERACTIONS

CHARACTERIZED BY ATOMIC FORCE MICROSCOPY

Yaqing Wang, Ph.D.

University of Nebraska Medical Center, 2021

Supervisor: Yuri L. Lyubchenko, Ph.D., D.Sc.

This thesis describes the nanoscale studies of protein-DNA interactions with different complexities using atomic force microscopy (AFM). One of the systems deals with DNA replication rescue. To maintain the genetic integrity, replication machinery needs to minimize the error rate, repair the damages, and restart the stalled replication caused by the attacks from the environment and inside the cell. The stalled replication rescue is orchestrated by a series of proteins- for example, the DNA helicases PriA and RecG and the ssDNA binding protein (SSB).

We demonstrated that SSB stimulates the restart process in two aspects. First, SSB facilitates the binding of PriA to the DNA substrates. Second, SSB remodels PriA, allowing the loading of PriA onto the duplex strands and the thermally driven and ATP-independent translocation of PriA. Importantly, we discovered that PriA changes the moving direction during translocation, which increases the residence time for PriA to bind to the vicinity of the replication fork. We hypothesize that PriA alters the direction by switching to the other DNA strand, a novel property of PriA that ensures the rescue at the fork position on various stalled replication forks.

Based on previous studies in the lab that revealed the remodeling of RecG by SSB, we hypothesize that the ATP-independent translocation of RecG can be stopped by the lesions in template DNA, leading to the dissociation of RecG from the DNA substrates. The results confirmed that DNA mispairings damage the binding of RecG and limit the translocation of remodeled RecG. Furthermore, the characterization of RecG dynamics on a mobile fork substrate suggests that RecG can couple the ATP-dependent fork regression with the SSB displacement during the fork rescue.

Another system focuses on the assembly of nucleosome arrays. To test the hypothesis that DNA sequence is a factor in the compaction of nucleosomes, we assembled nucleosomes on DNA substrates with different sequences. Our data showed that nucleosomes are often positioned close to each other, suggesting that non-specific sequence allows nucleosomes to communicate actively, and the internucleosomal interactions could compact nucleosomes into higher-ordered structures.

TABLE OF CONTENTS

ACKNOWLEDGMENTS.....	ii
ABSTRACT	iv
TABLE OF CONTENTS	vi
LIST OF FIGURES.....	x
LIST OF TABLES	xii
LIST OF ABBREVIATIONS.....	xiii
LIST OF CONTRIBUTIONS.....	xv
 Chapter 1. INTRODUCTION.....	 1
1.1 DNA replication	1
1.2 Stalled replication fork rescue	2
1.3 Nucleosome array.....	9
1.4 Significance	10
Chapter 2. METHODS.....	12
2.1 Introduction	12
2.2 Materials and reagents	16
2.3 AFM sample preparation	17
2.3.1 Assemble the DNA substrates	17
2.3.2 Functionalize the mica surface	20
2.3.3 Prepare the protein-DNA complex	20
2.3.4 Deposit the samples on the APS-mica.....	21
2.4 AFM imaging and Data analysis	21

Chapter 3. CHARACTERIZATION OF THE BINDING INTERACTION OF PRIA WITH STALLED REPLICATION FORKS.....	27
3.1 Introduction	27
3.2 Methods	28
3.2.1 Purify the proteins.....	28
3.2.2 Assemble the DNA substrates	29
3.2.3 Prepare the AFM sample of protein-DNA complex	31
3.2.4 Acquire and analyze the AFM images	32
3.3 Results	32
3.3.1 The binding preference of PriA to the DNA substrates	33
3.3.2 The interactions between PriA and SSB on the stalled DNA fork	41
3.3.3 The interactions of PriA and SSB in the absence of DNA	49
3.3.4 The role of the C-terminal of SSB in the protein-protein interaction.....	51
3.4 Discussion	55
3.4.1 The role of ssDNA and fork in PriA binding activity.....	55
3.4.2 Remodeling of PriA by SSB on the stalled fork	56
3.4.3 The protein-protein interaction and the effect of SSB tail region on it.....	57
3.4.4 Conclusion.....	59
Chapter 4. DYNAMICS OF PRIA AT STALLED DNA REPLICATION FORKS	60
4.1 Introduction	60
4.2 Methods.....	61
4.2.1 Purify the proteins.....	61
4.2.2 Assemble the DNA substrates	61
4.2.3 Preparation of protein-DNA complex	63
4.2.4 Dry sample imaging and imaging in aqueous solution with time-lapse AFM.....	63
4.3 Results	63
4.3.1 The ATP-dependent translocation of PriA on the fork substrates	63

4.3.2 The visualization of PriA translocation in the presence of ATP	70
4.4 Discussion	77
4.4.1 The specificity of PriA in binding to fork DNA	77
4.4.2 The ATP-dependent translocation and dynamics of PriA	78
4.4.3 The strand-switching property of PriA.....	80
4.4.4 Conclusion.....	81
Chapter 5. RESTRICTION OF RECG TRANSLOCATION BY DNA MISPAIRING	82
5.1 Introduction	82
5.2 Methods	83
5.2.1 Purify the proteins.....	83
5.2.2 Assemble the DNA substrates	84
5.2.3 Prepare the protein-DNA complexes.....	84
5.2.4 Acquire and analyze the AFM images	85
5.3 Results	86
5.3.1 The interaction between SSB and RecG on the designed fork DNA substrates	88
5.3.2 The restriction of RecG translocation by the mispairing on the parental duplex.....	90
5.4 Discussion	94
5.4.1 The effects of SSB on RecG binding to the fork DNA substrates.....	94
5.4.2 The translocation of RecG limited by the lesions in the parental duplex.....	95
5.4.3 Conclusion.....	96
Chapter 6. DNA FORK REGRESSION DYNAMICS INDUCED BY RECG HELICASE	97
6.1 Introduction	97
6.2 Methods.....	97
6.2.1 Purify the proteins.....	97
6.2.2 Assemble the DNA substrates	98
6.2.3 Prepare the protein-DNA complexes.....	98

6.2.4 Acquire and analyze the AFM images	99
6.3 Results	99
6.3.1 The two dynamic states of the F12 fork substrate.....	99
6.3.2 The assembly of a Holliday Junction on the F12 DNA substrate.....	104
6.3.3 The fork regression of the F12 DNA substrate by RecG.....	108
6.4 Discussion	114
6.4.1 The fork regression by RecG in the presence of ATP	114
6.4.2 Conclusion.....	115
Chapter 7. ASSEMBLY OF NUCLEOSOME ARRAY INTO HIGHER-ORDER STRUCTURES	116
7.1 Introduction	116
7.2 Methods.....	117
7.2.1 Prepare the DNA substrate	117
7.2.2 Assemble the nucleosome.....	118
7.2.3 AFM imaging and data analysis	118
7.3 Results and discussion	119
7.3.1 The assembly of oligo-nucleosome on the DNA substrate.....	119
7.3.2 The internucleosomal distance of the trinucleosome	128
7.3.3 Discussion	130
Chapter 8. SUMMARY.....	131
8.1 The PriA helicase at the stalled replication fork	131
8.2 The RecG helicase at the stalled replication fork.....	132
8.3 The nucleosome array	132
8.4 Prospects.....	133
Chapter 9. REFERENCES.....	135

LIST OF FIGURES

Figure 1.1. Schematic of the unbroken stalled fork rescue initiated by RecG.	5
Figure 1.2. Schematic of PriA replication restart initiation.	8
Figure 2.1. Schematic of the principle of AFM.....	14
Figure 2.2. Assembly of the fork DNA substrates.	19
Figure 2.3. Measurement of the protein position.	23
Figure 2.4. Measurement of the protein distribution of the complexes containing PriA and SSB proteins.	25
Figure 2.5. Measurement of the size of the protein.....	26
Figure 3.1. DNA substrates designed for this chapter.....	30
Figure 3.2. AFM results of DNA substrates.	34
Figure 3.3. AFM results of DNA and SSB complexes.	36
Figure 3.4. In the absence of SSB, PriA binds preferentially to the F3 DNA substrate.	38
Figure 3.5. In the presence of SSB, PriA can be localized to duplex regions of forks.	42
Figure 3.6. AFM results of DNA and PriA complexes.....	44
Figure 3.7. The distributions of proteins in double-feature complexes on each fork DNA substrate, with the SSB position corresponding to zero value on the maps.	46
Figure 3.8. Volume analysis for samples of fork DNA mixed with SSB and PriA.....	48
Figure 3.9. Size analysis for free protein: volume distributions fitted by Gaussian for PriA, and SSB, respectively.....	50
Figure 3.10. AFM results of fork DNA and SSB Δ C8 complexes.	52
Figure 3.11. SSB Δ C8 does not load PriA.....	54
Figure 4.1. DNA substrates designed for this chapter.....	62
Figure 4.2. The control experiment of PriA mixed with fork DNA substrates in the absence of ATP.....	65
Figure 4.3. The ATP-dependent translocation of PriA on the fork DNA substrates.....	67

Figure 4.4. The control experiment of PriA mixed with duplex DNA substrate (1036 bp in length).....	69
Figure 4.5. Time-lapse AFM data of PriA translocation on the lagging strand arm of the F13 DNA substrate.	72
Figure 4.6. Time-lapse AFM data of PriA translocation on the parental duplex of the F13 DNA substrate.	74
Figure 4.7. Time-lapse AFM data of PriA translocation on the lagging strand arm of the F13 DNA substrate.	76
Figure 5.1. The design for the lesions in the stalled replication fork.....	87
Figure 5.2. AFM analyses of the RecG-SSB-DNA complexes on each DNA substrate in the absence of ATP.....	89
Figure 5.3. The mapping of protein positions on each DNA substrate.	91
Figure 5.4. The analysis for the RecG-SSB distance.	93
Figure 6.1. Dynamic fork design for this chapter.....	101
Figure 6.2. AFM analysis for the fork position of the F12 DNA substrate (the kinked DNA molecules).....	103
Figure 6.3. AFM analysis of the fork position on the F12 DNA substrate probed by annealing with a complimentary 69-nt ssDNA.	105
Figure 6.4. AFM results of SSB-F12 DNA substrates in the absence of ATP.....	107
Figure 6.5. AFM analyses of the RecG-SSB-F12 complexes in the absence and presence of ATP.	109
Figure 6.6. The SSB position in the complex.....	111
Figure 6.7. The RecG position in the RecG-DNA complex.	113
Figure 7.1. The AFM image of the nucleosome array.	121
Figure 7.2. Gallery of the subpopulations in the oligo-nucleosome.	123
Figure 7.3. AFM analyses for the arm length of the “2-1” subpopulation in the trinucleosome.	127
Figure 7.4. The measurement for the distance between the nucleosomes in the “2-1” subpopulation of the trinucleosome.	129

LIST OF TABLES

Table 3.1. The binding yield of DNA with PriA at the molar ratio of 1:8.	40
Table 7.1. The yield of each oligo-nucleosome.	124

LIST OF ABBREVIATIONS

AFM	Atomic Force Microscopy
SSB	Single-Stranded DNA Binding Protein
ssDNA	Single-Stranded DNA
ORC	Origin Recognition Complex
<i>E.coli</i>	<i>Escherichia coli</i>
NCP	Nucleosome core particle
STM	Scanning Tunneling Microscopy
PSD	Position-Sensitive Photodetector
IC-AFM	Intermittent Contact Mode Atomic Force Microscopy
AC-AFM	Alternating Contact Mode Atomic Force Microscopy
TM-AFM	Tapping Mode Atomic Force Microscopy
HS-AFM	High-Speed Atomic Force Microscopy
APS	1-(3-Aminopropyl) silatrane
DBD	DNA Binding Domain
HD	Helicase Domain
3'BD	3'-Binding Domain
WHD	Winged-Helix Domain
CTD	C-terminal domain
WT	Wild Type Protein
OB-fold	oligonucleotide-oligosaccharide binding fold

EM	Electron Microscopy
Cryo-EM	Cryo-Electron Microscopy

LIST OF CONTRIBUTIONS

Chapter 2 is quoted from the source “Wang, Y., Sun, Z., Bianco, P. R., and Lyubchenko, Y. L. (2021) Characterize the Interaction of the DNA Helicase PriA with the Stalled DNA Replication Fork Using Atomic Force Microscopy. Bio-protocol 11, e3940-e3940” with permission.

Chapter 3 is reformatted from our published paper “Wang, Y., Sun, Z., Bianco, P. R., and Lyubchenko, Y. L. (2020) Atomic force microscopy-based characterization of the interaction of PriA helicase with stalled DNA replication forks. Journal of Biological Chemistry 295, 6043-6052” with permission.

Chapter 4 is based on the publication “Sun, Z., Wang, Y., Bianco, P. R., and Lyubchenko, Y. L. (2021) Dynamics of the PriA Helicase at Stalled DNA Replication Forks. The Journal of Physical Chemistry B 125, 4299-4307” with permission. Zhiqiang and I did the experiments and analyses.

Chapter 5 and 6 are adapted from the source “Sun, Z., Wang, Y., Bianco, P. R., and Lyubchenko, Y. L. (2020) Nanoscale interaction of RecG with mobile fork DNA. Nanoscale Advances 2, 1318-1324” with permission, and a submitted manuscript.

Chapter 6 is the preliminary data for the nucleosome array project that Tommy and I are working on.

Chapter 1. INTRODUCTION

Protein-DNA interactions are of fundamental importance to living cells involved in key biological processes such as packaging, replication, recombination, restriction, and transcription. Therefore, it is crucial to understand the nature of protein-DNA interactions and their role in gene expression, cell division, and differentiation. Many proteins, such as repressors and restriction endonucleases, have high specificity for their particular target sites. In contrast, others, especially those involved in packaging or replication, have low or no sequence specificity. Significant progress has been made in the detailed analysis of specific protein-DNA interactions, opening avenues in the treatment of numerous diseases. However, DNA-protein interactions are far from being completely understood despite numerous techniques that have been developed.

This thesis focuses on the protein-DNA interactions involved in stalled replication rescue (SSB, RecG, and PriA) and DNA packaging in chromatin. The use of atomic force microscopy (AFM), a method for direct nanoscale visualization of label-free molecular systems, provided insights into questions relating to PriA interactions with stalled replication forks and the formation of the nucleosome array depending on the DNA sequence.

1.1 DNA replication

Replication is the process in which two identical DNA molecules are produced from the double-stranded DNA molecule. DNA replication is the fundamental genetic process that defines the fate of the cell (1-5). Each strand of existing DNA acts as a template for replication during cell division, and the resulting daughter cells contain the same genetic information as the parental cell (6,7). This phenomenon of the old strand serving as a template for the new strand makes the DNA replication semi-conservative. The DNA replication in eukaryotes and prokaryotes proceeds bidirectionally

(8,9). In eukaryotes, the replication machinery is more complicated due to the differences in the DNA sizes, presence of telomeres, and packing of DNA with complexes of histones (10).

DNA replication in eukaryotes requires extracellular signals to coordinate specialized cell divisions in different tissues of multicellular organisms (11,12). It must be completed with the time available during the S phase of the cell cycle. Therefore, the replication process is initiated at multiple origins by forming multiple replication forks (13,14). Initiation of DNA replication in eukaryotes begins with the formation of the origin recognition complex (ORC) at the origin of replication, which recruits other essential DNA replication proteins. The DNA double helix at the origin is then unwound by the helicase activity, resulting in the strand separation into a Y shape replication fork. The replication fork is bidirectional from the origin of the replication; one strand oriented in the 3'-to-5' direction is called the leading strand, and the other strand oriented in the 5'-to-3' direction is called the lagging strand. On the leading strand, DNA polymerase moves toward helicase. However, on the lagging strand, DNA polymerase moves away from the replication fork, and the lagging strand is copied as a series of short fragments (Okazaki fragments). Each of the Okazaki fragments is later fused by DNA ligase to produce the full, unfragmented strand. The leading and lagging strands are replicated in different processes to compensate for the differences in their replication directions (15).

During the entire replication process, replication forks frequently encounter obstacles that cause fork stalling. Such events cause incompletely replicated chromosomes that prevent the segregation of full genomes to daughter cells if left unrepaired. Under normal conditions, several proteins around the replication region serve to repair, stabilize and restart the stalled forks and complete the process (16,17). It is important to know that many of the components involved in the replication process are encoded by the tumor suppressor genes (18,19). A loss of function due to deletion or mutation could lead to genomic instability, a hallmark of cancer.

1.2 Stalled replication fork rescue

Even though several studies have been performed over the years to understand the activity of different protein networks in the rescue of the stalled replication forks, the process is still unclear. Because of the comparative simplicity, prokaryotes are ideal for investigating the basic mechanisms of molecular biology. *Escherichia coli* (*E.coli*) has been the long-studied model system to understand the complex molecular mechanisms in eukaryotic biological processes. Similar to eukaryotes, the replication initiates at the *oriC* in prokaryotes (15,20-22). The initiation of the replication generates two replication forks in a bidirectional way that move away from each other until it encounters the terminus region. After that, the site-specific recombination or decatenation resolves the division of two daughter molecules at the end of the replication process. Each replication fork stalls or collapses at least once during the cell cycle (23,24), which could be deleterious to the cell if replication failed to restart. Fork stalling could result from the replisome facing a physical barrier to progression or the replisomes encountering a shortage of DNA synthesis precursors (25-27). Impediment also includes the other proteins bound to the DNA ahead of the replication forks, such as DNA repair enzymes, RNA polymerase, DNA polymerase and the coupled ribosomes, non-coding lesions on the DNA, abnormal structure of DNA, RNA-DNA loops (R loops), and single- or double-stranded DNA breaks (25,26,28-33). The rescue of the stalled forks is required to protect further lethal events to the cell. Genome duplication depends on the coordination between the DNA replication, repair, and recombination machinery (15,34). In some cases, the replisome components rescue the stalled forks, since this process does not require recombinational repair machinery (28,35-38).

Here we mainly focus on the stalled replication fork at which DNA remains intact, but the replisome progression is blocked. Figure 1.1 shows a possible pathway for the rescue of stalled forks, which involves the DNA helicase RecG-regulated regression of the newly replicated strands of DNA at the stalled fork to form a Holliday junction-like structure intermediate (39-42). This structure will be processed with branch migration by the multi-subunit enzyme RuvAB. The

junction may be cleaved by the dimeric Holliday Junction resolvase RuvC to form a substrate for the DNA helicase PriA to process (43-45). However, when the replisome encounters a double-strand DNA break or a nick in the leading strand, the impeded fork will undergo rescue by RecBCD (46-48). Alternatively, the impeded fork with double-strand breaks can be rescued by homologous recombination through the RecF pathway (49-51). Similar to the RecBCD pathway, the RecF pathway also requires RecA for strand invasion (51-55). In some instances, stalled forks can be directly restarted by components of the replisome itself (56-59).

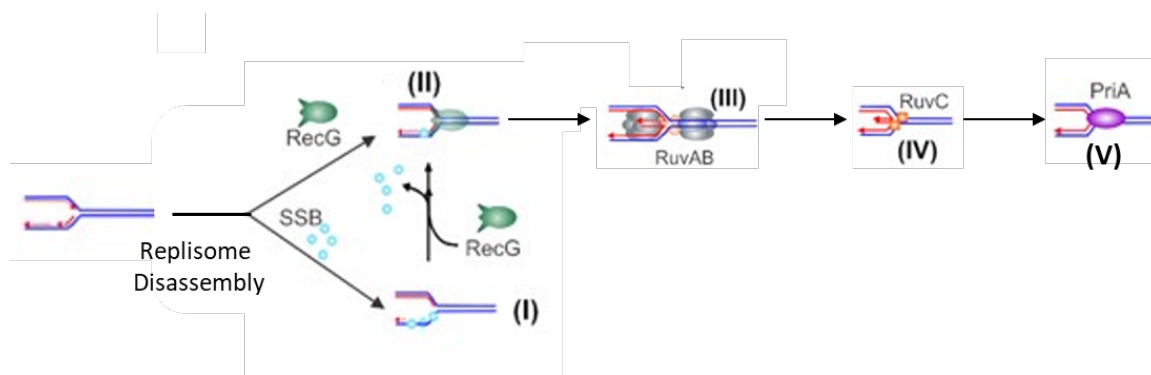


Figure 1.1. Schematic of the unbroken stalled fork rescue initiated by RecG. After replisome disassembly from the impeded replication fork, SSB (blue spheres) binds to the ssDNA gap rapidly (step I) if there is any. RecG then binds and regresses the fork to form a Holiday Junction, displacing SSB from the fork (step II). This structure can be further processed by RuvAB (step III) or RuvC (step IV) that cleave the substrate for PriA to restart the replication (step V). Meanwhile, RecG can directly bind to the stalled fork and initiate the rescue. This schematic is adapted from reference (17).

In addition to the enzymes, the single-stranded DNA binding protein (SSB) is also important to the stalled replication rescue. SSB binds and protects exposed single-stranded DNA (ssDNA) and interacts with multiple proteins at forks, including replisome components and repair enzymes (60-64). It is a homo-tetramer with two domains in each monomer; the N-terminal domain that is responsible for tetramer formation and DNA binding and the C-terminal domain that mediates protein-protein interactions (65,66). SSB binds tightly and cooperatively to ssDNA while still providing access to the protein partners (63). When protein-protein interactions occur between an SSB tetramer and an interactome partner, loading that protein onto DNA can take place, which increases access of that protein to the needed sites on the DNA (67,68).

In this thesis, we focus on the interactions of RecG and PriA helicases with stalled forks and the role of SSB protein in these interactions. RecG is a monomeric DNA helicase that catalyzes fork regression on nascent stalled forks. At the stalled fork, RecG catalyzes simultaneous annealing of nascent and template strands, which leads to the formation of four-way DNA junctions (Holliday Junctions) during the regression process (41,42,69,70). It was demonstrated by our lab that SSB also affects fork regression by stimulating RecG binding to the fork and remodeling RecG so that the helicase scans the parental duplex ahead of the fork by thermal sliding to test the integrity of the fork (71-73). After the fork regression, the stalled replication fork can be further branch migrated by RuvAB and cleaved by RuvC into a substrate for PriA (74-76). Alternatively, RecG can regress forks into the PriA substrates directly (77).

PriA is another important player in the replication fork recovery process. It is a monomeric DNA helicase involved in most replication reactivation mechanisms, recruiting the replisome back onto the stalled fork (23,78-80). It has been shown to unwind DNA with a 3'-to-5' polarity fueled by the hydrolysis of ATP (81,82). PriA can recognize multiple DNA structures, ranging from simple replication forks to D-loops formed in recombinational repair (23,83,84). In addition to structure-specific binding, PriA also binds to the SSB at the replication forks through protein-

protein interactions, which stimulates helicase activity (23,83-87). This helicase is responsible for duplex unwinding to load DnaB onto the lagging strand. Once DnaB has been loaded, the replisome will form and resume the replication (88,89).

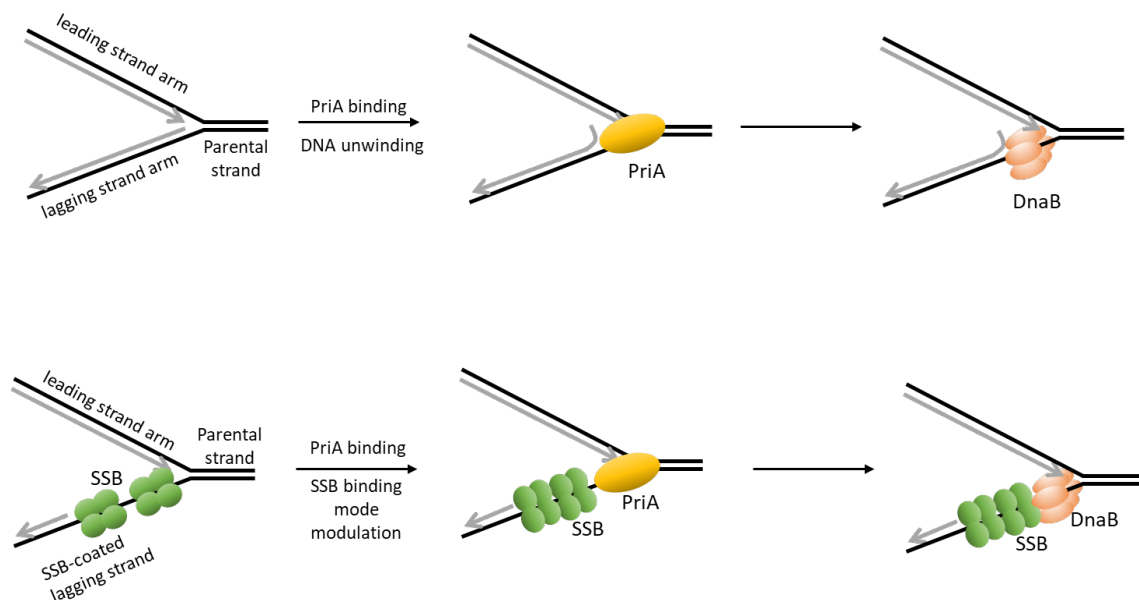


Figure 1.2. Schematic of PriA replication restart initiation. PriA binds to the stalled replication forks with either duplex or SSB-bound ssDNA lagging strand. PriA remodels the lagging strand arm to expose ssDNA by either unwinding DNA or altering the DNA-binding mode of SSB. This schematic is adapted from reference (85).

1.3 Nucleosome array

The DNA of a single mammalian cell fits into the confines of the nucleus by a hierarchical scheme of folding and compaction into chromatin. The nucleosomes core particle (NCP) is the basic repeating subunit of chromatin. Nucleosomes consist of an octameric histone core (comprising two copies each of H2A, H2B, H3, and H4) wrapped around 147 bp of DNA in about 1.75 superhelical turns (90-92). The disordered positively charged tails of histone proteins flexibly surround the core and play an essential role in many biological processes (93). The histone tails also contain many important epigenetic modification sites (94). The electrostatic interactions between the negatively charged DNA and the positively charged histone proteins stabilize the NCP, while the sequence of nucleosomal DNA may also determine the strength of histone-DNA interactions and may mediate the organization of nucleosomes into larger scales (95,96). The assembly of DNA into nucleosomes protects DNA from nucleases and restricts the binding of trans-acting factors. However, for transcription to occur, the nucleosomal DNA needs to unwrap from the central histone core, which can be mediated by modifications to the histone tails (97,98).

The nucleosomes, together with linker histones (H1), self-organize into chromatin, the higher-order structure. Experimental approaches have indicated that chromatin in living cells predominantly comprises irregular structures (99-104). Additionally, the results from chromosome conformation capture techniques and electron cryotomography have revealed the existence of clusters of only a few nucleosomes (103-106). This further suggests that chromatin organization is dominated by intermediate scale assemblies (107). Meantime, it has been proposed that tetranucleosomes are the functional and structural units that regulate gene expression (103,108-110). There might be two possible motifs of tetranucleosome that serve regulatory functions, the α -tetrahedron and the β -rhombus. However, these studies were performed with the DNA substrates

containing repeats of the nucleosome-specific DNA sequences that raise questions on the role of the DNA sequence in the nucleosome array assembly (111).

Using atomic force microscopy (AFM) and high-speed time-lapse atomic force microscopy (HS-AFM), our lab characterized the sequence-dependent nucleosome nanoscale structure by comparing the positioning of nucleosomes and DNA wrapping on the non-specific sequence to that on the synthetic Widom 601 positioning sequence (111). The AFM analyses suggest that nucleosomes assemble on the non-specific sequence without any preference for the position. On dinucleosomes, the nucleosomes formed on the non-specific sequence have a tendency to locate near the position of the nucleosome formed on the 601 sequence. This indicates that the internucleosomal interactions play a role in nucleosome positioning.

1.4 Significance

The rescue of replication forks stalled on the DNA template is critically essential for cell division and survival and for maintaining the integrity of the genome (112). When the replication stress is prolonged, it can lead to irreversible fork breakage to the replication fork, resulting in genome instability and the development of cancer (113,114). In this consideration, a comprehensive understanding of how cells rescue their stalled forks might lead to new strategies in cancer treatment. *E.coli* has been used as a study model to understand the stalled replication fork rescue. The starting point of many models for rescue involves regression of the newly replicated strands to form a Holliday Junction, which is driven by helicases including RecG, RuvABC, and RecA (115-119). The endpoint of most mechanisms is to produce a structure for PriA to load the replicative DNA helicase DnaB onto the DNA, leading to the resumption of replication (77,120-122).

The results presented in this thesis elucidate the roles of SSB on interactions of PriA and RecG with the stalled replication rescue. These analyses revealed that PriA has a binding preference to a fork substrate with a nascent lagging strand, and it is the fork structure that plays an essential

role in PriA's selection of DNA substrates. Furthermore, we found that SSB loads PriA onto the duplex regions of the substrates, suggesting remodeling of PriA by SSB. The high-speed AFM analyses revealed a novel property of PriA that it could switch the DNA template during translation. The lesions on the duplex DNA impair the binding of RecG to the fork, resulting in an inability to regress the stalled fork. The interactions between RecG and SSB with the mobile fork substrate showed that RecG regresses the stalled fork and displaces the SSB.

Elucidating principles of the assembly of the nucleosomal array into higher-order structures is critical for understanding the function of chromatin. Chapter 7 presents the preliminary data for the assembly of the nucleosome array depending on the DNA sequence. Here we designed a DNA substrate capable of binding at least four nucleosomes, consisting of a Widom 601 sequence as an anchor and a non-specific sequence for three additional histone octamers to bind. These studies revealed a strong effect of the DNA sequence on the assembly of nucleosome arrays, allowing for the formation of condensed oligonucleosomes with tight interactions between them.

Chapter 2. METHODS

2.1 Introduction

Atomic force microscopy (AFM), developed from scanning tunneling microscopy (STM), has offered a wide range of bio-applications in the past few decades due to its unprecedented sub-nanometer resolution of single molecules on the surfaces (123-126). By using a sharp tip scanning over the surface of the sample while sensing the interaction between the tip and the sample, AFM allows measurements of biological samples in physiological-like environments at a high spatial resolution, avoiding complex sample preparation procedures (127-129). The monitored interactions between the tip and the surface arise from different forces, including van der Waals forces, short-range repulsive forces, adhesion and capillary forces (130,131).

Besides surface imaging, AFM force measurements can be used to probe molecular interactions, physicochemical properties, surface stiffness, and macromolecular elasticity, contributing to our knowledge of the sample's physical properties. When used in an imaging mode, the AFM cantilever scans the surface of the specimen line after line, whereas in a force-probing mode, the cantilever is moved only in the vertical direction, perpendicular to the specimen plane (132,133). The vertical motion of the cantilever is controlled by piezoelectric actuators affording sub-nanometer resolution. The displacement of the cantilever is monitored directly with either a capacitor or a linear voltage differential transformer. As a result, high-resolution force-versus-extension curves of single molecules can be recorded (134).

As shown in Figure 2.1, the standard AFM consists of five main components; a tip connected to a cantilever, a piezoelectric scanner, a position-sensitive photodetector (PSD), an optical lever system, and a feedback-loop system. By mounting the cantilever on the piezoelectric

element and measuring the shift from its natural resonance frequency due to the interactions between the tip and samples, topographical information of the sample can be extracted.

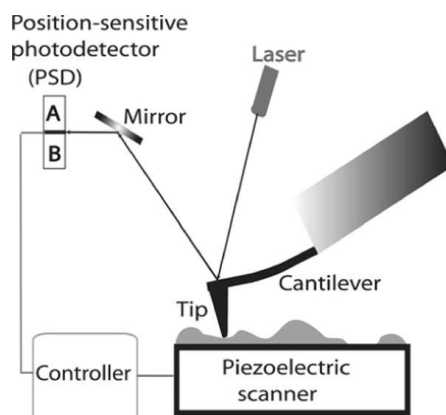


Figure 2.1. Schematic of the principle of AFM. The position of the tip relative to the sample is controlled by the piezoelectric scanner. During scanning, the vertical displacement of the tip is detected using the optical lever principle. The position of the light spot on the PSD is measured and sent as deflection signals to the feedback electronics. This figure is adapted from reference (135).

Typically, AFM has three different modes of operation: contact mode, non-contact mode, and intermittent-contact mode. In contact mode, the tip-sample interaction is maintained by measuring the deflection of the tip cantilever determined by van der Waals repulsive forces. In this mode, due to the strong repulsive interaction between tip and sample surface, damage or deformation of the biological sample can occur during the scanning process (136). In non-contact mode, the system vibrates a stiff cantilever near its resonant frequency without making contacts with the sample (137). The resonance frequency and amplitude of the oscillating probe decrease as the sample surface is approached. The development of the intermittent-contact (IC) mode or alternating contact (AC) mode, also known as tapping mode (TM) AFM, is a key advance in AFM technology. In AC/IC/TM-AFM, a cantilever is deliberately vibrated at the frequency close to the cantilever resonance frequency by a piezoelectric modulator with a very small amplitude (138). The van der Waals attractive force between the sample surface and the tip changes the amplitude and the vibration, which is monitored by the feedback-loop system to control the tip-sample distance while the tip approaches the surface (139). The tapping mode AFM overcomes problems such as friction and adhesion that are usually associated with conventional AFM approaches, allowing high-resolution imaging of soft samples that are difficult to examine using the contact AFM technique (140-144).

When choosing AFM as a single-molecule biophysical technique to characterize the interactions between DNA and proteins, it is important to realize that accurate data collection is often delicate due to the several limitations and difficulties associated with the technique. One of the most crucial aspects is sample preparation. Indeed, to withstand the force exerted by the scanning probe, the sample must be well attached to an appropriate solid substrate. Several methods have been developed to functionalize the solid substrate (145-148). We use aminopropyl silatrane (APS) to functionalize the mica surface with amine groups (146,149-162). The major advantage of these sample preparation procedures is that they work under a wide variety of ionic conditions, pH,

and over a wide range of temperatures, allowing us to characterize the interactions between DNA substrate and different types of proteins. Additionally, the dried samples can be stored in vacuum or argon for at least several weeks.

Another advantage of AFM is the capability to scan the samples in an aqueous solution. High-speed AFM (HS-AFM) has been developed to overcome the slow data acquisition rate of a conventional AFM instrument, which can acquire images at a sub-second rate, thereby allowing for the observation of DNA-protein dynamics at the nanoscale level (163-167). In addition to the high scan rate, which is about 1,000 times faster than possible with a conventional AFM, the tip-sample interaction is also minimized. Typically, the force applied in HS-AFM is <100 pN, and the tip-sample interaction is also reduced as a result of the high oscillation frequency (~ 1.6 MHz) (168). The HS-AFM tips are sharpened to a radius of curvature as small as ~ 1 nm, which allows for nanometer resolution while imaging in the aqueous solution.

Our lab has applied the regular tapping mode AFM and the HS-AFM to study the dynamics of nucleic acid molecules, intrinsically disordered proteins, nucleosomes, and DNA-protein interactions (126,146,150,155,157,159,162,169-178). In this chapter, a general description of the experimental approaches used in this thesis is provided, with specifics of each approach addressed in the methods section of each subsequent chapter.

2.2 Materials and reagents

1. Amicon Ultra-0.5 ml centrifugal filters (Millipore-sigma, UFC503008, pore size: 30 kDa NMWCO)
2. Nonwoven cleanroom wipes: TX604 TechniCloth (TexWipe, catalog number: TX604)
3. Petri dish (Fischer Scientific, catalog number: 08-757-100A)
4. Standard disposal cuvette (Perfector Scientific, catalog number: 9002)

5. Distilled deionized H₂O (DDI H₂O)
6. pUC19 Vector (New England Biolabs, catalog number: N3041S)
7. PCR primers (IDT, custom order)
8. DreamTaq polymerase (ThermoFisher Scientific, catalog number: EP0701)
9. Deoxynucleotide (dNTP) Solution Mix (New England Biolabs, catalog number: N0447S)
10. PCR purification kit (Qiagen, catalog number: 28104)
11. Restriction endonuclease: DdeI (New England Biolabs, catalog number: R0175S)
12. Restriction endonuclease: BspQI (New England Biolabs, catalog number: R0712S)
13. CutSmart[®] Buffer (New England Biolabs, catalog number: B7204S)
14. Oligonucleotide (IDT, custom order)
15. T4 Polynucleotide Kinase (New England Biolabs, catalog number: M0201S)
16. T4 DNA Ligase (ThermoFisher Scientific, catalog number: 15224090)
17. Muscovite Block Mica (AshevilleMica, catalog number: Grade-1)
18. 1-(3-Aminopropyl) silatrane (APS) [synthesized as described in ref (149)]
19. TESPA-V2 AFM probe (Bruker AFM Probes, catalog number: TESPA-V2)

2.3 AFM sample preparation

2.3.1 Assemble the DNA substrates

The tail DNA substrate (T3 or T5) was assembled from a duplex-DNA segment with a sticky end (the 224 bp segment for T3, the 356 bp segment for T5) and a tail-DNA segment. The fork DNA

substrate was assembled from two duplex-DNA segments with sticky ends (the 224 bp segment and the 356 bp segment) and a core fork segment (shown in Figure 2.1).

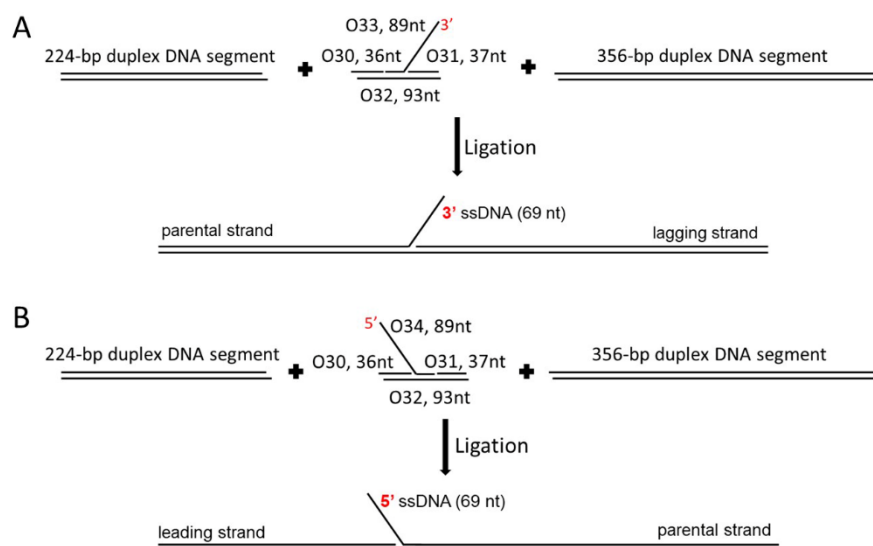


Figure 2.2. Assembly of the fork DNA substrates. *A*, the F3 DNA substrate: ligate two duplex-DNA segments with sticky ends (the 224-bp segment and the 356-bp segment) and a core fork segment (with a 3'-end, 69-nucleotide single-stranded region) together. *B*, the F5 DNA substrate: ligate two duplex-DNA segments with sticky ends (the same duplex-DNA segments used for the F3 DNA substrate) and a core fork segment (with a 5'-end, 69-nucleotide single-stranded region) together.

The 224-bp segment was obtained by the PCR reaction using pUC19 as the template and the forward primer F364, 5'-GAGTTCTTGAAGTGGTGGCC-3', and reverse primer R356, 5'-GGTAACTGTCAGACCAAGTTTACTC-3'. The PCR product was cut by DdeI and purified by electrophoresis gel purification (2% w/v agarose gel), and separated from the gel using the Gel Extraction Kit from Qiagen (Hilden, DE). Similarly, the 356-bp segment was obtained from the PCR reaction using pUC19 and the forward primer F480, 5'-GCGATTAAGTTGGGTAAC-3', and reverse primer R480, 5'-GTTCTTTCCTGCGTTATC-3'. The PCR product was cleaved by BspQI and purified by agarose gel. DNA concentration was then determined using NanoDrop Spectrophotometer (ND-1000, Thermo Fischer).

2.3.2 Functionalize the mica surface

The 50 mM 1-(3-Aminopropyl) silatrane (APS) stock solution was prepared in DDI H₂O as described (149). The stock solution can be kept for more than a year at 4 °C. An aliquot of 15 ml working APS solution (167 μM) was diluted from the APS stock. Mica strips (1 × 3 cm) can be cut from high-quality mica sheets, which will be placed diagonally in a cuvette. A schematic of the process to prepare APS functionalized mica for AFM imaging is shown in ref (179). We use a razor blade to cleave layers of the mica until both sides are freshly cleaved. The freshly cleaved mica will be placed into the APS-filled cuvette and incubated for 30 min. We then rinse the mica piece under running DDI H₂O droplets or slow fluid for ~10 s. Both sides of the APS-mica strip will be dried under the gentle argon flow. After that, the APS-functionalized mica is ready to use. Otherwise, it can be stored in a clean cuvette in a vacuum chamber or in the argon atmosphere for at least a week.

2.3.3 Prepare the protein-DNA complex

The binding solution was diluted from the 10× binding buffer. The binding solution contains 10 mM Tris-HCl (pH 7.5), 50 mM NaCl, 5 mM MgCl₂, and 1 mM DTT. The protein-DNA mixture

was mixed and incubated at room temperature ($\sim 20^{\circ}\text{C}$) for 10 min. After incubation, the protein-DNA complex solution was diluted to achieve a lower DNA concentration ($\sim 2\text{ nM}$) and ready for deposition onto the APS functionalized mica.

2.3.4 Deposit the samples on the APS-mica

A $10\text{ }\mu\text{l}$ aliquot of the diluted protein-DNA sample was deposited at the center of the APS-mica piece ($1 \times 1\text{ cm}$) and incubated for two minutes. We then rinse the mica sample with DDI H_2O droplets for $\sim 10\text{ s}$ to remove all buffer components and dry the deposited mica sample under a light flow of clean argon gas with the help of a clean wipe. The mica sample was attached to the magnetic puck by double-faced adhesive tape and stored in a vacuum cabinet filled with argon for at least 3 hours before imaging.

2.4 AFM imaging and Data analysis

Images were acquired using a MultiMode 8, Nanoscope V system (Bruker, Santa Barbara, CA) operated in tapping mode in the air on TESPA probes (320 kHz nominal frequency and a 42 N/m spring constant) from the same vendor.

The AFM images were analyzed using the FemtoScan Online software package (Advanced Technologies Center, Moscow, Russia). Graphs were made by Origin software (OriginLab Corporation, Northampton, MA, USA). The contour length of the DNA molecule was measured from one end to the other. For the internal length calibration, the measurements were collected to generate a histogram and fitted with Gaussian distribution. The calibration factor was obtained by dividing the mean value (nm) over the designed substrate length (bp).

The protein position was measured from the end of the short arm on the DNA substrates towards the center of the protein (arm length 1, shown in Figure 2.3 B). And we continued to measure from the center of the protein towards the other end of the DNA substrate to obtain the

contour length of the DNA (arm lengths 1 and 2 together, shown in Figure 2.3 *B*). The arm length in bp can be acquired by dividing the measured length over the calculated calibration factor.

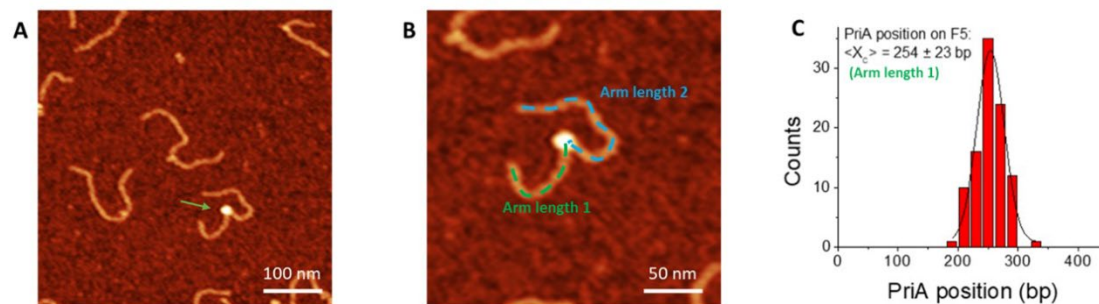


Figure 2.3. Measurement of the protein position. *A*, representative AFM image ($0.5 \mu\text{m} \times 0.5 \mu\text{m}$) of F5 DNA substrate with PriA. The Z-scale is 3 nm. Arrow points to bound PriA on the F5 DNA substrate. *B*, zoomed-in image ($0.25 \times 0.25 \mu\text{m}$) with the dotted line showing the contour length measurement. The position of each protein is measured from the end of the short arm to the center of the protein (dotted green line). The total length of the protein-bound DNA substrate was measured continuously from the center of the protein to the end of the other arm (dotted blue line). *C*, the histogram for PriA position on the F5 DNA substrate using the data of the short arm length. The histogram was fitted by Gaussian with a single peak centered at 254 ± 23 bp (S.D.), and with a bin size of 20 bp.

For the double-feature complexes, the height of each feature was measured using the cross-section feature of the software as described below. We were able to distinguish the proteins according to the volume measurement. For the length measurement, we start from the end closer to the SSB, continuously measure towards the center of SSB and the helicase, and continue recording until the end of the other side of the DNA substrate (Figure 2.4 *B*).

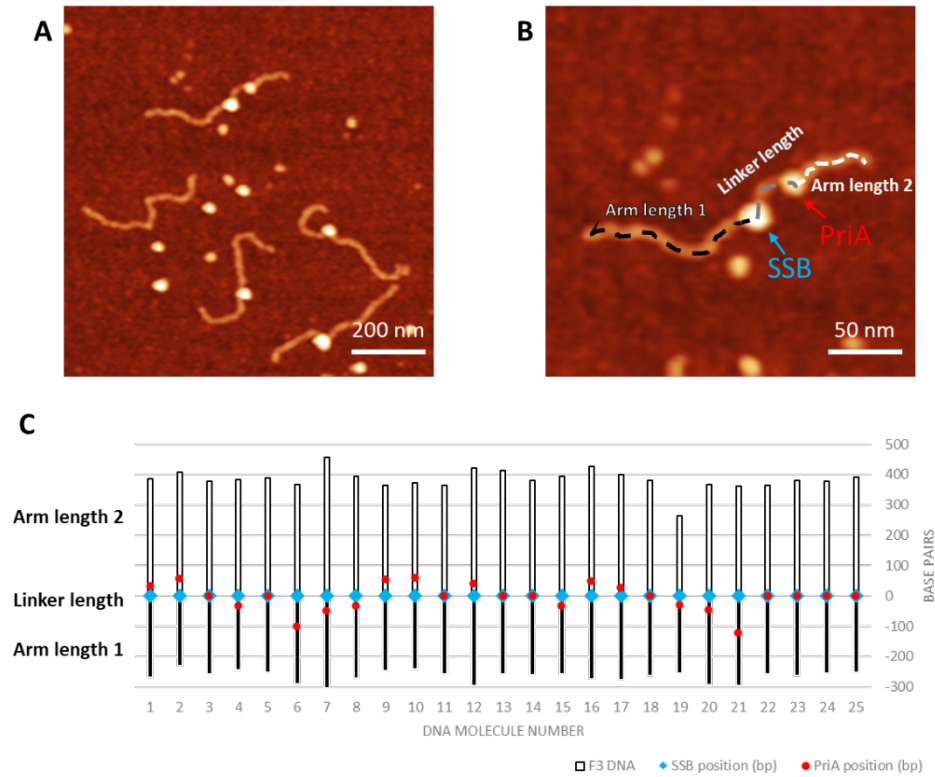


Figure 2.4. Measurement of the protein distribution of the complexes containing PriA and SSB proteins. *A*, representative AFM image of the PriA+SSB+fork DNA ($0.5 \times 0.5 \mu\text{m}$). The Z-scale is 3 nm. *B*, the zoomed-in image ($0.25 \times 0.25 \mu\text{m}$) of the double-protein complex with the dotted line showing the contour length measurement. The red arrow directs to PriA in the complex, while the blue arrow directs the SSB position. *C*, map of the proteins on the F3 DNA substrate with the SSB position corresponding to zero value. Blue diamonds indicate the position of SSB, and the red dots point to the PriA position.

The volume of the protein was collected from two sets of height (H) and full width at half maximum values (D) by orthogonal cross-section measurements (Figure 2.5 *A*). The measured height and width were applied to the formula as described in (128,180): $V = 3.14 \times H/6 \times (0.75 \times D_1 \times D_2 + H^2)$.

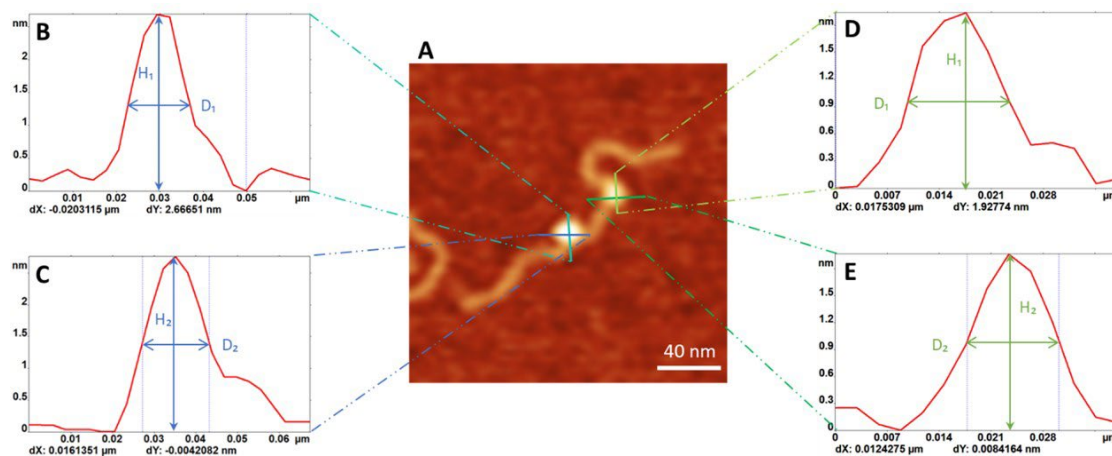


Figure 2.5. Measurement of the size of the protein. *A*, representative AFM image of the double-protein complex (0.2×0.2 μm). *B-E*, cross-section profiles (green and blue lines) of a protein produce the height distribution curves: *B* and *C*, the plots for SSB; *D* and *E*, the height distributions for PriA. Based on these curves, height (H) and width (D) values were collected for the protein volume calculation.

Chapter 3. CHARACTERIZATION OF THE BINDING INTERACTION OF PRIA WITH STALLED REPLICATION FORKS

3.1 Introduction

DNA replication frequently overcomes obstacles such as DNA lesions, tightly bound protein-DNA complexes, and unusual secondary structures such as double-strand breaks (23,34,36,181). Impeded forks must be restarted for the DNA replication to be accurately completed (182). Consequently, numerous mechanisms have evolved that either help minimize the frequency or remove the roadblocks and restart the stalled fork. In some cases, stalled forks can be directly restarted by the components of the replisome itself (56-59). Otherwise, the restart of stalled replication can be reinitiated by the recombinational repair machinery. In *E. coli*, the DNA helicase PriA is involved in the replication restart machinery (121). PriA recognizes abandoned DNA replication forks, remodels the DNA at the fork junction, and loads the replicative DNA helicase DnaB onto the template lagging strand arm, allowing replication to continue (85,183).

PriA remodels stalled DNA forks with 3'-to-5' DNA helicase activity, which opens the duplex for entry of DnaB when sufficient ssDNA is not available (81). Alternatively, PriA can modulate the DNA-binding mode of SSB if ssDNA gaps are occupied by SSB (85). PriA has a two-domain architecture; an N-terminal DNA binding domain (DBD) and a C-terminal helicase domain (HD) (184-189). The two evolutionarily conserved helicase lobes link ATP hydrolysis to DNA translocation and unwinding. Outside of the helicase core, the N-terminal 3'-binding domain (3'BD) binds the leading arm of replication forks, with specificity for the 3'-OH group of the nascent leading strand. A winged-helix domain (WHD) is tethered to the 3'BD and the helicase core by the

structurally dynamic linker and interacts with the parental duplex. A C-terminal domain (CTD) forms a structural core by interfacing with the other domains, except for the loosely-associated WHD. The isolated CTD has been shown able to bind to a variety of DNA structures *in vitro*, including ssDNA, duplex DNA, and a replication fork mimic. In addition to its DNA-binding functions, PriA interacts with other proteins, including SSB and PriB (86,87,190,191). The cooperation among each domain preserves the recognition and binding activity of PriA to various DNA constructs as well as the interaction with other proteins (16,85,192).

We used AFM to understand how PriA interacts with forks and how SSB might influence binding. These experiments were performed in the absence of ATP to separate the DNA-binding properties of PriA from its helicase activity. The AFM studies revealed the role of the fork type on the efficiency of PriA binding. Furthermore, SSB protein interacts with PriA and potentially changes the protein conformation, allowing for the binding of PriA to the DNA duplex. Experiments with the SSB mutant revealed the necessity of the C-terminal segment in this remodeling activity of SSB.

3.2 Methods

3.2.1 Purify the proteins

All the proteins in this chapter were provided by Dr. Piero Bianco, University of Nebraska Medical Center.

Purification of the PriA protein followed the method described in (86). The his-PriA protein was purified by ammonium sulfate precipitation followed by affinity chromatography using HisTrap FF crude column, SP Sepharose column (Equilibrated with 20 mM potassium phosphate, pH 7.6, 150 mM KCl, 0.1 mM EDTA, and 1 mM DTT; Eluted with a linear 150–500 mM KCl gradient) and Heparin column (Equilibrated with 20 mM Tris-OAc, pH 7.5, 0.1 mM EDTA, 1 mM

DTT, 10% (v/v) Glycerol, and 100 mM KCl; Eluted with a linear KCl gradient of 100–600 mM). Fractions containing PriA were pooled and dialyzed overnight against storage buffer (20 mM Tris-HCl (pH 7.5), 1 mM DTT, 400 mM KCl, and 50% (v/v) glycerol). PriA concentration was determined using an extinction coefficient (ϵ) of 104,850 M⁻¹ cm⁻¹ (73).

SSB protein was purified from strain K12 Δ H1 Δ trp, as described in references (63,193). The concentration of the purified protein was determined at 280 nm using ϵ = 30,000 M⁻¹ cm⁻¹ (73). Similar to the wildtype (WT), the his-SSB Δ C8 mutant protein was purified using nickel column chromatography, followed by step elution from ssDNA–cellulose (194).

3.2.2 Assemble the DNA substrates

Each tail DNA substrate (T3 or T5) was assembled from a duplex-DNA segment and a tail-DNA segment. The preparation of duplex-DNA segments, the 224 bp segment for T3 and the 356 bp segment for T5, were described in Chapter 2.3.1. The tail-DNA segment for T3 was assembled from the phosphorylated ssDNA oligonucleotides O42 (5'-TCATGACTCGCTGCGCAAGGCTAACAGCATCACACACATTAACAATTCTAACATCTG-3') and O43 (5'-CCTTGCGCAGCGAGTCA-3'); O42 and O43 were mixed in an equal molar ratio, and annealed by heating to 95°C and then cooling down slowly to room temperature. The tail-DNA segment was then ligated with the 224 bp duplex-DNA segment in the molar ratio of 1:1 to assemble the T3 DNA substrate. Similar to the assembly of the T3 DNA substrate, the tail-DNA segment for T5 was annealed from the 5'-phosphorylated oligonucleotides O36 (5'-TACGTGTAGGAATTATATTAAAGAGAAAGTGAAACCCAAAGAATGAAAAAGAAGATGTTAGAATTGTAAGCGGTATCAGCTCACTCATA-3') and O37 (5'-GCTTATGAGTGAGCTGATACCGC-3') in the equal molar ratio and then was ligated together with the 356 bp duplex-DNA segment in 1:1 molar ratio to obtain the T5 DNA substrate.

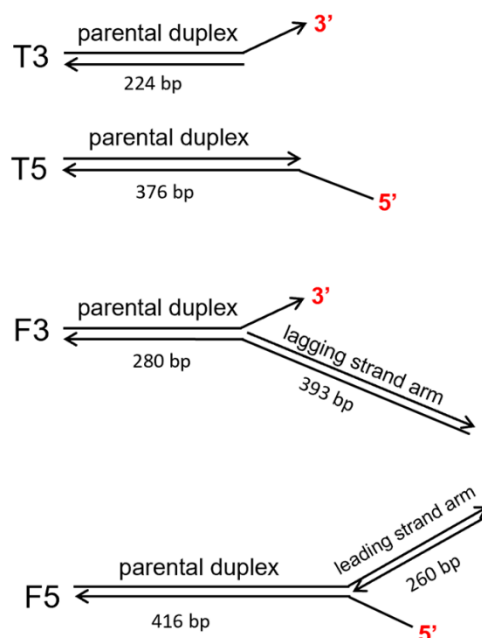


Figure 3.1. DNA substrates designed for this chapter. T3 DNA substrate comprises a 244 bp duplex region and a 3'-end 69-nucleotide single-stranded region. T5 DNA substrate has a 5'-ssDNA region of the same length, but the duplex size is 376 bp. For the F3 DNA substrate (3'-end) and the F5 DNA substrate (5'-end) DNA, 69 nt ssDNA was placed inside the 673 bp (676 bp for F5 DNA substrate) duplex with unequal lengths of the DNA duplex regions. Arrows mark the 3'-end of DNA strands.

The fork DNA substrates (F3 and F5 DNA substrates) were assembled from two duplex-DNA segments and a core fork segment. The core fork segment of the F3 DNA substrate was assembled by annealing the 5'-phosphorylated oligos in the same molar ratio (O30: 5'-TCATCTGCGTATTGGGCGCTCTTCCGCTTCCTATCT-3'; O31: 5'-TCGTTCCGGCTGCGGCGAGCGGTATCAGCTCACTCATA-3'; O32: 5'-GCTTATGAGTGAGCTGATACCGCTCGCCGCAGCCGAACGACCTTGCGCAGCGAGTCA GTGAGATAGGAAGCGGAAGAGCGCCCAATACGCAGA-3' and O33: 5'-CACTGACTCGCTGCGCAAGGCTAACAGCATCACACACATTAACAATTCTAACATCTGGTTTTTCATTCTTTGGGTTTCACTTTCTCCAC-3'). While the core fork segment of the F5 DNA substrate was annealed from phosphorylated O30, O31, O32, and O34 (O34: 5'-CTAACAGCATCACACACATTAACAATTCTAACATCTGGGTTTTTCATTCTTTGGGTTTCACTTTCTCCACCACTGACTCGCTGCGCAAGG-3'), in the same molar ratio. The two duplexes and core fork segment were ligated together at the molar ratio of 1:1:1 at 16°C overnight. The final products were purified with HPLC using a TSKgel DNA-STAT column.

3.2.3 Prepare the AFM sample of protein-DNA complex

PriA/DNA complex was prepared by mixing the PriA monomer (molar concentration: 100 nM) with DNA substrates (molar concentration: 45 nM) in a molar ratio of 8:1. The mixture was incubated in 10 µl of binding buffer [10 mM Tris-HCl (pH 7.5), 50 mM NaCl, 5 mM MgCl₂, 1 mM DTT] for 10 min at room temperature. After incubation, the complex was then diluted to achieve a lower DNA concentration (~1 nM), which was ready for deposition onto the APS functionalized mica.

SSB/PriA/DNA complex was prepared by mixing the proteins first: the SSB tetramer (molar concentration: 50 nM) was mixed with PriA monomer in a molar ratio of 1:2, and the mixture was kept on ice for 30 minutes before use. The mixture of proteins was added to fork DNA substrates in a 1:2:4 (DNA substrates: SSB: PriA) molar ratio and then incubated in 10 µl binding

buffer for 10 min at room temperature. After incubation, the complex was then diluted to achieve a lower DNA concentration (~ 1 nM) for AFM imaging using the APS functionalized mica procedure.

1-(3-aminopropyl) silatrane (APS) functionalized mica was used as the AFM substrate for all experiments. Fresh cleaved mica was incubated in 4ml APS (167 μ M) in a cuvette for 30 min and then was rinsed with DDI H₂O thoroughly as described in Chapter 2.3.4. 10 μ l of the sample were deposited onto the APS functionalized mica for two minutes. After two minutes of incubation, the mica was rinsed with DDI H₂O and then was dried with a gentle argon flow.

3.2.4 Acquire and analyze the AFM images

Images were acquired using tapping mode in air on a MultiMode 8, Nanoscope V system (Bruker, Santa Barbara, CA) using TESPA probes (320 kHz nominal frequency and a 42 N/m spring constant) from the same vendor. The dry sample AFM images were analyzed using the FemtoScan Online software package (Advanced Technologies Center, Moscow, Russia). The yield of protein-DNA complexes was calculated from the number of complexes dividing by the total number of DNA molecules. The positions of each protein were measured from the end of the short arm on the DNA substrates towards the center of the protein. The contour lengths of the DNA were then continuously measured from the center of the protein towards the other end of the DNA substrate. The histograms were approximated with Gaussian distribution, and the mean values and errors (S.D. and SEM) were calculated using Origin software (OriginLab Corporation, Northampton, MA, USA). The protein height and volume were measured with the cross-section option. The volume was calculated by applying the measured data to the formula: $V = 3.14 \times H/6 \times (0.75 \times D_1 \times D_2 + H^2)$, in which D_1 and D_2 are the diameters of the protein, which were measured twice, and H is the average height of the two measurements of the protein.

3.3 Results

3.3.1 The binding preference of PriA to the DNA substrates

The designed DNA substrates were assembled and verified by contour length measurements, shown in Figures 3.1 and 3.2, respectively. The tail substrates, T3 and T5, are duplex DNA with a 69-nt ssDNA tail on one end. By having different polarities of the ssDNA tail, these two substrates allow us to elucidate the effect of ssDNA polarity in the recognition and binding of PriA. The T3 DNA substrate consists of a 244 bp duplex region and a 3'-end 69-nucleotide single-stranded region. The T5 DNA substrate has a 5'-ssDNA region of the same length, but the size of its duplex region is 376 bp. The F3 and F5 DNA substrates also differ in the polarity of 69-nt ssDNA. The interactions of PriA with these substrates allow us to evaluate the role of fork orientation at the junction in the binding activities of PriA. These forks contained a 69 nt ssDNA arm asymmetrically placed within the DNA duplex region. The F3 DNA substrate has a gap in the nascent leading strand, while the F5 DNA substrate has a gap in its nascent lagging strand. Consequently, for the F3 DNA substrate, the DNA duplex regions are a 280 bp parental duplex and a 393 bp lagging strand arm. For the F5 DNA substrate, the parental duplex has 416 bp residues, and the other duplex region is a 260 bp leading strand arm.

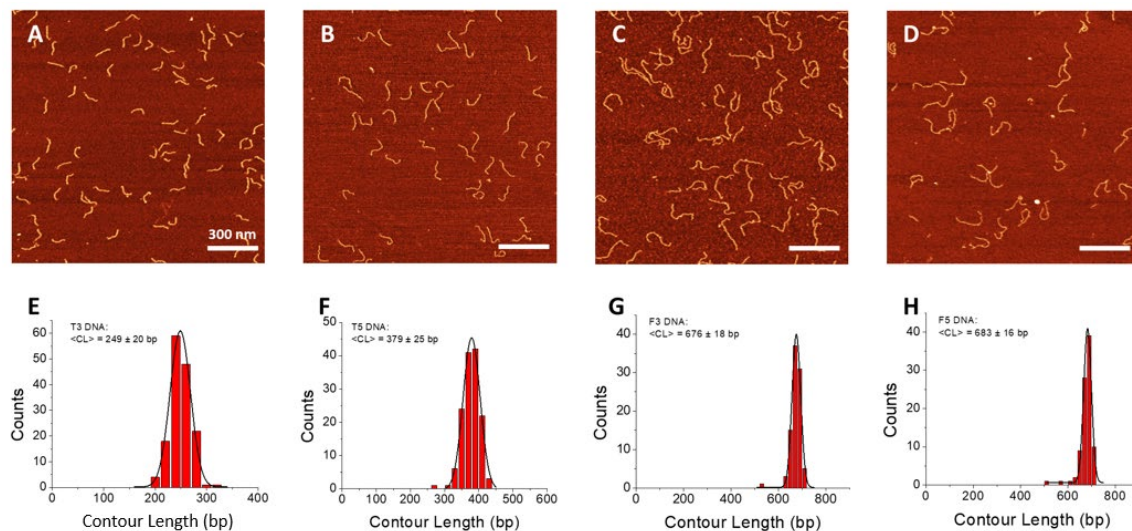


Figure 3.2. AFM results of DNA substrates. The upper panel shows AFM images of tail and fork DNA substrates. *A–D*, 1.5 x 1.5 μm AFM images of the T3 DNA substrate, the T5 DNA substrate, the F3 DNA substrate, and the F5 DNA substrate, respectively. The bar size is 300 nm. Z-scale is 2 nm. The lower panel shows DNA contour length measurements. Histograms were approximated by Gaussian functions with a bin size of 20 bp. *E*, the histogram for the T3 DNA substrate has a peak centered at 249 ± 20 bp (S.D.). *F*, the histogram for the T5 DNA substrate indicates a centered peak at 379 ± 25 bp. *G*, the histogram for the F3 DNA substrate is approximated by Gaussian with a peak centered at 676 ± 18 bp. *H*, the histogram for the F5 DNA substrate was centered at 683 ± 16 bp.

SSB protein was separately bound to each of the substrates to evaluate the accessibility of ssDNA. The AFM images are shown in Figure 3.3, demonstrating that SSB binds to only one of the two ends on tail DNA substrates. On fork DNA substrates, the position of SSB was measured from the end of the short arm towards the center of the protein in each complex. The histograms were approximated by single-peak Gaussians. The peak values, 276 ± 14 bp (S.D.) on the F3 DNA substrate and 260 ± 16 bp on the F5 DNA substrate, correspond to the fork positions as designed, which are 280 and 260 bp for F3 and F5 DNA substrates, respectively.

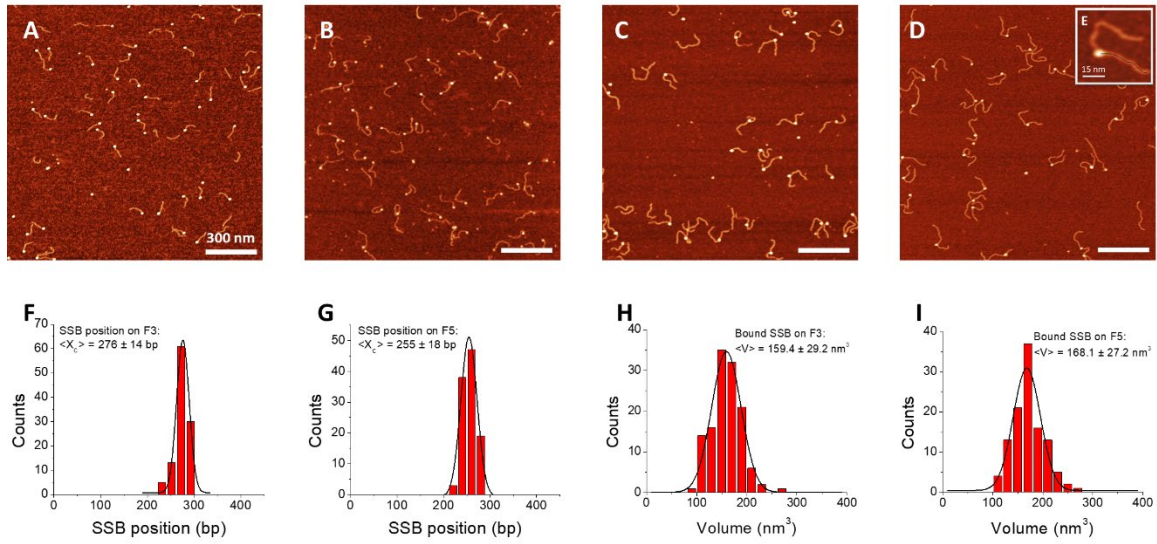


Figure 3.3. AFM results of DNA and SSB complexes. *A–D*, large-scale AFM images of DNA-SSB complexes ($1.5 \times 1.5 \mu\text{m}$): the T3 DNA substrate with SSB, the T5 DNA substrate with SSB, the F3 DNA substrate with SSB, and the F5 DNA substrate with SSB, respectively. Z-scale is 3 nm. *E*, a zoomed-in image shows the measurement of the protein position. The image size is 250 nm^2 . *F*, the Gaussian-fitted histogram for SSB position on the F3 DNA substrate was centered at 276 ± 14 bp (S.D.), with a bin size of 20 bp. *G*, the histogram for SSB position on the F5 DNA substrate was approximated by Gaussian distribution with a peak centered at 260 ± 16 bp. *H and I*, the volume histograms for bound SSB on fork DNA substrates. The bin size was 20 nm^3 . The average volume for SSB was $163 \pm 31 \text{ nm}^3$.

When mixed with T3 and T5 DNA substrates, PriA binds to only one end of the tail DNA substrates regardless of the large excess of the protein (8:1 PriA-to-DNA molar ratio), shown in Figures 3.4 *A and B*. Analysis of over 500 complexes demonstrated that <0.5% PriA was observed bound to both the ssDNA tail and the blunt end of the tail DNA substrate. This suggests that PriA binds poorly to blunt ends or dsDNA. Furthermore, the binding yield of PriA on tail DNA substrates, collected from three independent experiments, was $9.2 \pm 0.3\%$ on T3 DNA and $7.9 \pm 0.7\%$ on T5 DNA, pointing to a minor preference for PriA binding to the substrate with 3'-ssDNA tail.

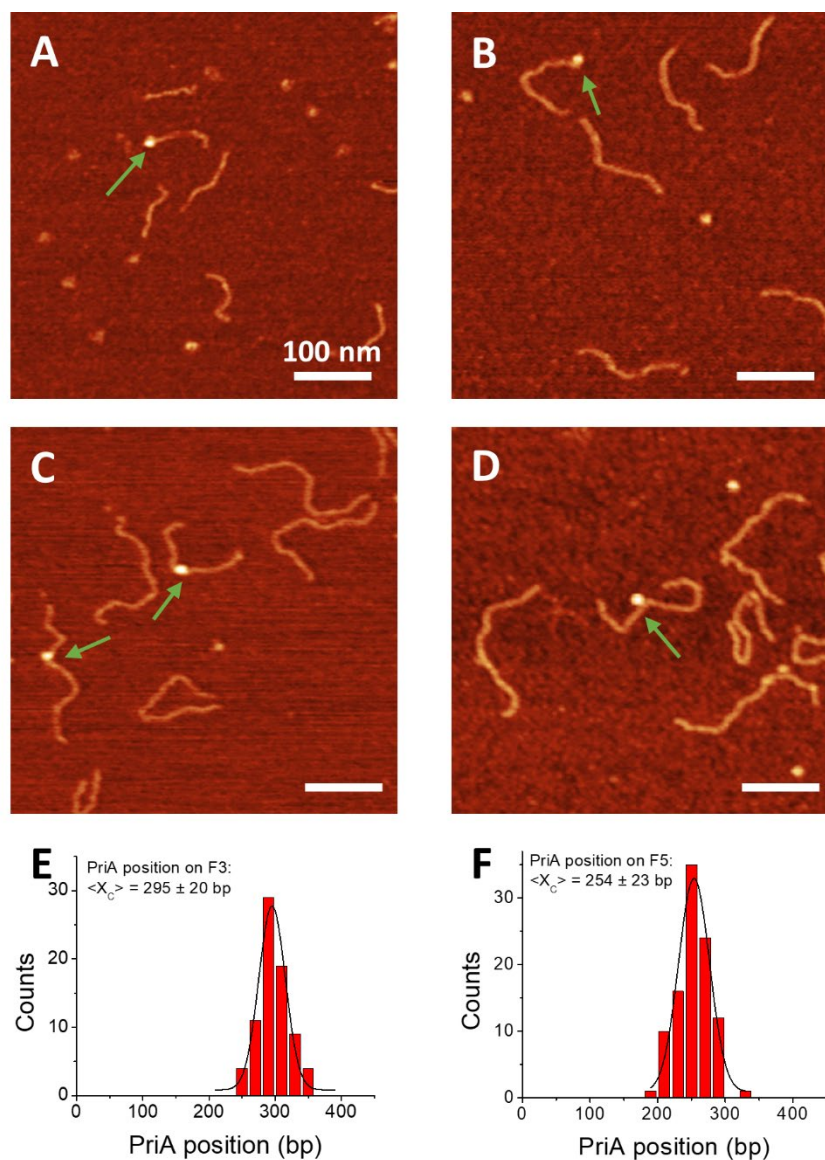


Figure 3.4. In the absence of SSB, PriA binds preferentially to the F3 DNA substrate. *A–D*, $0.5 \mu\text{m} \times 0.5 \mu\text{m}$ AFM images of the T3 DNA substrate with PriA, the T5 DNA substrate with PriA, the F3 DNA substrate with PriA, and the F5 DNA substrate with PriA, respectively. Arrows direct to bound PriA on DNA substrates. Z-scale is 3 nm. *E and F*, histograms for PriA position on fork DNA substrates, approximated by Gaussian with a bin size of 20 bp. The peaks were found to be centered at 288 ± 24 bp (S.D.) on the F3 DNA substrate and at 254 ± 23 bp on the F5 DNA substrate, respectively.

To assess the interactions of PriA with fork DNA substrates, PriA was separately bound to F3 and F5 DNA substrates and imaged, shown in Figures 3.4 *C and D*. The results show that PriA was bound exclusively to a site embedded within the duplex region. To determine if the binding site corresponds to the position of the fork, we measured the position of PriA in each complex from the end of the short arm toward the center of the protein. The histograms, shown in Figures 3.4 *E and F*, were fitted by single-peak Gaussians with a bin size of 20 bp. The centered peak of the histogram for PriA position on the F3 DNA substrate was found to be 295 ± 20 bp (S.D.). For PriA-DNA complexes on the F5 DNA substrate, the peak was centered at 254 ± 23 bp (S.D.). These peak values match the designed fork position, which supports our previous assumption that the fork provides the recognition and binding site for PriA to load onto DNA replication forks.

The yields of complexes for both substrates were measured, and the data revealed different results compared with tailed DNA substrates, shown in Table 3.1. The yield of PriA on the F3 DNA substrate was $13.0 \pm 1.2\%$, while it was $8.2 \pm 1.3\%$ on the F5 DNA substrate based on the results of three independent experiments. As the polarity of the ssDNA tail does not play an essential role in the binding preference for PriA, the difference between F3 and F5 DNA substrates suggests that other structural features of the fork substrates must be involved.

Table 3.1. The binding yield of DNA with PriA at the molar ratio of 1:8.

	T3+PriA	T5+PriA	F3+PriA	F5+PriA
Binding yield	$9.2 \pm 0.3\%$	$7.9 \pm 0.7\%$	$13.0 \pm 1.2\%$	$8.2 \pm 1.3\%$

3.3.2 The interactions between PriA and SSB on the stalled DNA fork

Studies show that SSB binds to the RecG and PriA helicases both *in vivo* and *in vitro* (86). Previously, we demonstrated that SSB remodeled RecG during DNA loading (71). Does SSB-PriA interaction also alter PriA binding activities? A similar analysis was performed to answer this question. Here, PriA was preincubated with SSB at a 2:1 molar ratio for 10 minutes on ice. Then, the mixture was added to fork DNA substrates in the molar ratio of 2:1 (complex: DNA substrate), and allowed to bind for 10 minutes at room temperature before deposition onto mica substrate for imaging.

Figure 3.5 shows that for both F3 and F5 DNA substrates, double-feature complexes were observed. The double features correspond to PriA and SSB bound to the same DNA molecule, with the larger protein being SSB and the smaller one being PriA, as explained below. Furthermore, in some complexes, the two proteins are located far from each other, while in others, SSB and PriA co-localize on the DNA (*insets i and ii*, respectively). These data suggest that interaction of PriA with SSB leads to a change in PriA conformation, allowing PriA to bind to duplex DNA. We termed this property of SSB remodeling, which was initially identified for SSB-mediated loading of RecG protein on the DNA fork.

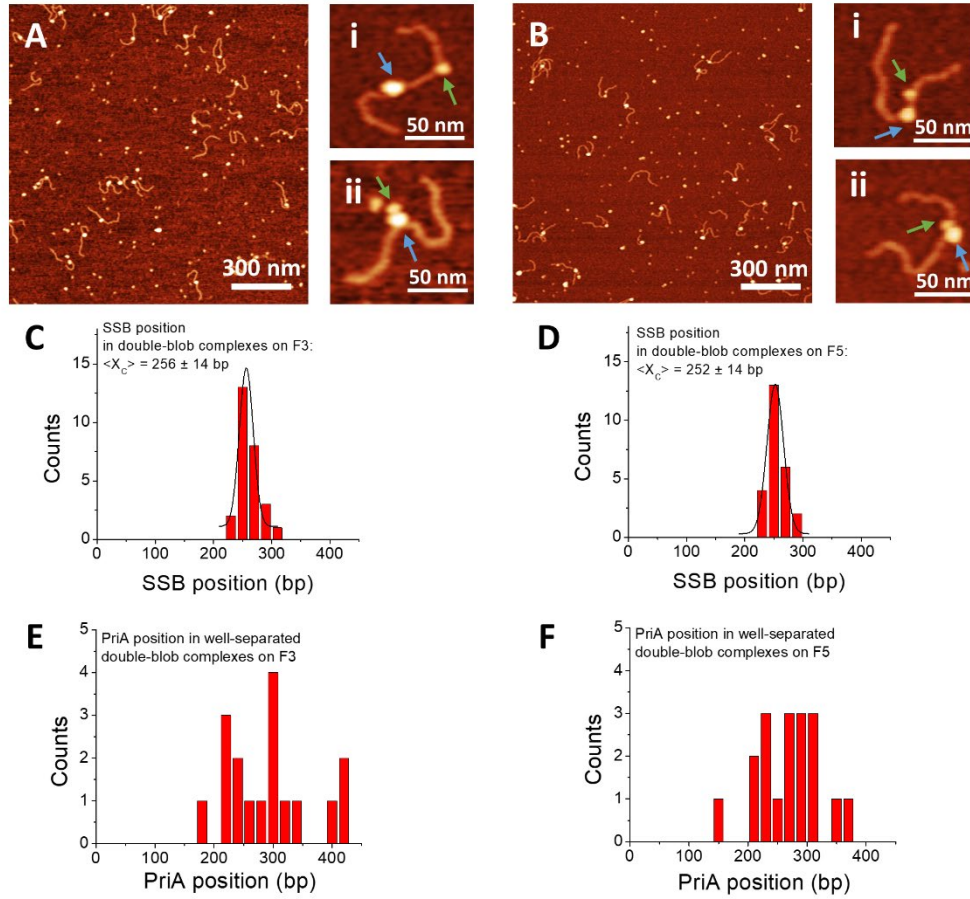


Figure 3.5. In the presence of SSB, PriA can be localized to duplex regions of forks. *A and B*, large-scale AFM images of F3 DNA substrate +SSB+PriA and F5 DNA substrate +SSB+PriA, respectively. Z-scale is 3 nm. *Insets i and ii*, a gallery of zoomed-in images of each complex to the right. Green arrows direct to PriA in the complexes, while SSB position is directed by blue arrows. *C and D*, histograms for SSB position in double-feature complexes, fitted by Gaussian function with a bin size of 20 bp. Peaks of SSB distributions were approximated at 256 ± 14 bp (S.D.) on the F3 DNA substrate and at 252 ± 14 bp on the F5 DNA substrate, respectively. *E and F*, histograms for PriA position in well-separated double-feature complexes on F3 and F5 DNA substrates, respectively.

PriA and SSB were bound to each DNA substrate separately, imaged, and analyzed to identify each protein in the double-feature complexes. As measured, SSB volume is between 159 ± 29 and $168 \pm 27 \text{ nm}^3$ (Figures 3.3 *H and I*). In contrast, the volume of PriA range from 113 ± 23 to $116 \pm 29 \text{ nm}^3$ (Figures 3.6 *C and D*). Therefore, the large proteins correspond to SSB, and the smaller ones are PriA. Based on this, the positions of SSB and PriA could be collected. The distribution of SSB positions is narrow, and the Gaussian maximum (F3 DNA substrate: 256 ± 14 bp and F5 DNA substrate: 252 ± 14 bp) correlates with the specific binding of SSB to the ssDNA region at the fork. The results show that SSB remains bound at the fork position (Figures 3.5 *C and D*)

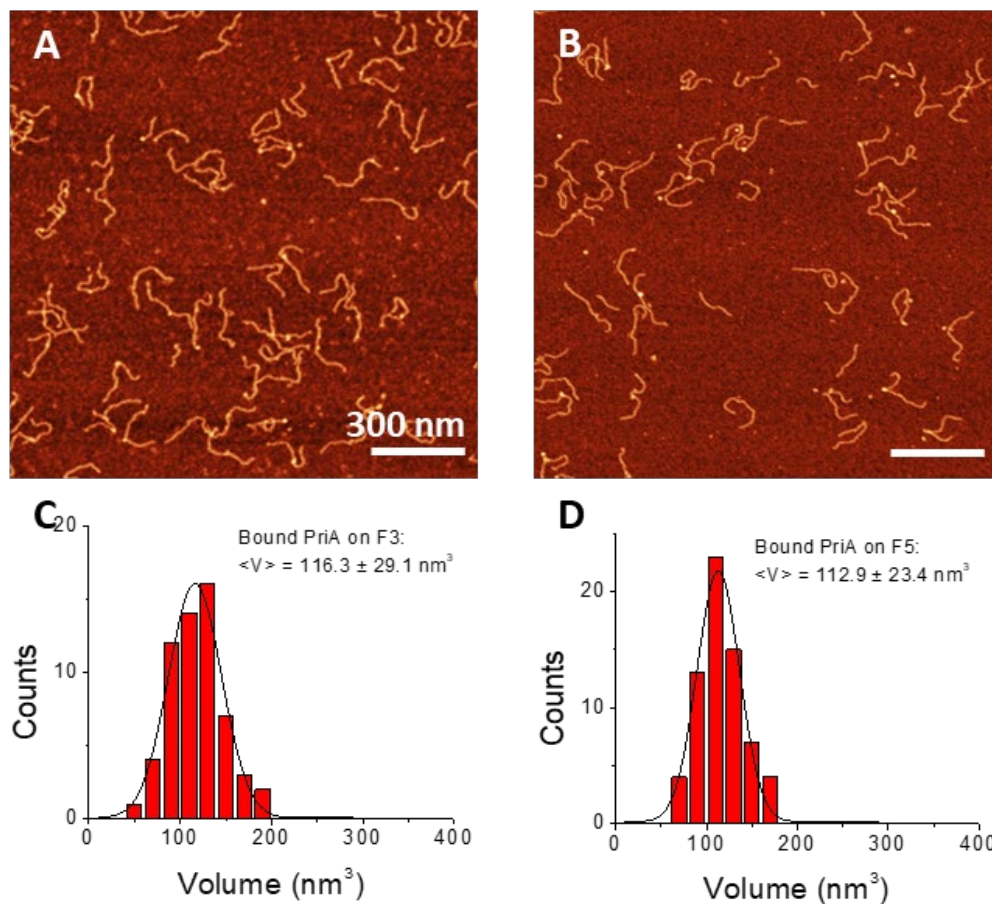


Figure 3.6. AFM results of DNA and PriA complexes. *A and B*, large-scale AFM images of DNA-PriA complexes (1.5 $\mu\text{m} \times 1.5 \mu\text{m}$): the F3 DNA substrate with PriA, and the F5 DNA substrate with PriA, respectively. Z-scale is 3 nm. *C and D*, volume distributions for bound PriA on fork DNA substrates. The bin size was 20 nm³. The histogram of bound PriA on the F3 DNA substrate was centered at $116.3 \pm 29.1 \text{ nm}^3$ (S.D.) by single-peak Gaussian fitting. The histogram of bound PriA on the F5 DNA substrate was centered at $112.9 \pm 23.4 \text{ nm}^3$. The average volume for PriA was $115 \pm 30 \text{ nm}^3$ (S.D.).

The results show that SSB enables the loading of PriA onto the duplex regions (Figures 3.5 *E and F*), whereas in the absence of SSB, PriA binds specifically to the fork region. In Figure 3.7, the position of PriA was mapped relative to that of SSB, as the SSB position indicates where the fork is. In the maps, the SSB position (green squares) is set to zero, marking the fork position. For the F3 DNA substrate, PriA (red dots) bound to the parental duplex arm sits in the negative interval, and the positive values indicate PriA positioning on the lagging strand. The occurrence of PriA positioning on the parental arm, or the lagging strand, or colocalizing with SSB at the fork was found to be 28, 32, and 40%, respectively. Therefore, in the presence of SSB, PriA is loaded preferentially at the fork. While it is loaded onto the duplex regions, there is no preference for one region over the other. In contrast, for the F5 DNA substrate, the occurrence of PriA positioning on the parental arm, or the leading strand, or colocalizing with SSB at the fork was found to be 24, 48, and 28%, respectively. Therefore, on the F5 DNA substrate, the fork with a gap in the nascent lagging strand, PriA is preferentially loaded onto the leading strand.



Figure 3.7. The distributions of proteins in double-feature complexes on each fork DNA substrate, with the SSB position corresponding to zero value on the maps. Green squares indicate the position of SSB, and the red dots point to the PriA position. *A*, the map of proteins on the F3 DNA substrate. PriA in negative interval means that they positioned on the parental strand, and positive values indicate PriA positioned on the lagging strand. *B*, the map of proteins on the F5 DNA substrate. PriA in negative interval means that they positioned on the leading strand, and positive values indicate PriA positioned on the parental strand.

In addition to the colocalized double-feature complexes, single-feature complexes were observed at the fork position, but the sizes of these complexes varied. The complex could be bound PriA, SSB, or SSB-PriA complexes of larger sizes. The volume data was collected to identify the components of each protein-DNA complex. The volume distribution fitted with multi-peak Gaussians for the F3 DNA substrate is shown in Figure 3.8 *A*. Peak 1 is centered at $137 \pm 37 \text{ nm}^3$, which is close to the volume of bound SSB on the F3 DNA substrate (Xc, $159 \pm 29 \text{ nm}^3$ in Figure 3.3 *H*). Peak 2 is approximated at $244 \pm 28 \text{ nm}^3$, corresponding to the complexes of PriA and SSB (free PriA volume: $58 \pm 12 \text{ nm}^3$, bound SSB volume: $159 \pm 29 \text{ nm}^3$). The population of those large features is ~24%, approximated by the area under Gaussian.

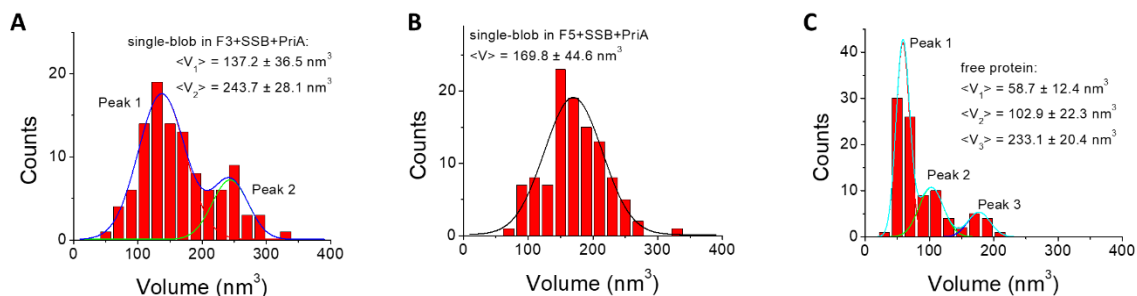


Figure 3.8. Volume analysis for samples of fork DNA mixed with SSB and PriA. *A*, the multi-peak Gaussian fitted distribution for the single-feature complexes on the F3 DNA substrate. Peak 1 is centered at $137.2 \pm 36.5 \text{ nm}^3$, and peak 2 is approximated at $243.7 \pm 28.1 \text{ nm}^3$. The population approximated by the area under the curve is 76.1% for peak 1 and 23.9% for peak 2. *B*, the volume distribution for single-feature complexes on the F5 DNA substrate. The peak fitted with Gaussian was centered at $169.8 \pm 44.6 \text{ nm}^3$. *C*, the volume distribution for free proteins in the same image. The histogram shows three peaks based on multi-peak Gaussian fitting, which are $58.7 \pm 12.4 \text{ nm}^3$, $102.9 \pm 22.3 \text{ nm}^3$, and $233.1 \pm 20.4 \text{ nm}^3$. The population approximated by the area under the curve is 59.9% for peak 1, 27.5% for peak 2, and 12.6% for peak 3.

A similar analysis was done for F5 DNA substrates with data shown in Figure 3.8 *B*. The volume distribution was fitted with single-peak Gaussian with a peak centered at $170 \pm 45 \text{ nm}^3$. This value shows a minor difference from the volume of bound SSB on the F5 DNA substrate ($168 \pm 27 \text{ nm}^3$, shown in Figure 3.3 *I*), suggesting that the SSB-PriA complexes formation are subtle at the fork region of F5 DNA substrate.

3.3.3 The interactions of PriA and SSB in the absence of DNA

To characterize the interaction of SSB-PriA in the absence of DNA, we also analyzed the sizes of free proteins in the same samples, with fork DNA substrates mixed with SSB and PriA. The volume distribution is shown in Figure 3.8 *C*. The histogram shows three peaks based on multi-peak Gaussian fitting, which are $59 \pm 12 \text{ nm}^3$, $103 \pm 22 \text{ nm}^3$ and $233 \pm 20 \text{ nm}^3$. Peak 1 matches the volume of free PriA ($58 \pm 12 \text{ nm}^3$), shown in Figure 3.9 *A*. Peak 2 is close to the volume of free SSB ($91 \pm 21 \text{ nm}^3$ in Figure 3.9 *B*). Peak 3 could be assigned to the SSB-PriA complex, even though the measured volume of each protein was smaller than half of the 3rd peak value, because neither tetrameric SSB nor monomeric PriA aggregates with themselves, based on the narrow single-peak distribution of each volume measurement in single-protein binding control experiments. Also, peak 3 is with the smallest probability, which is 12.6% evaluated by the area under the curve, while the probabilities of the other two are 59.9% for peak 1 and 27.5% for peak 2. Therefore, though the population of the SSB-PriA complexes is low, the interaction between SSB and PriA in the absence of DNA also exists.

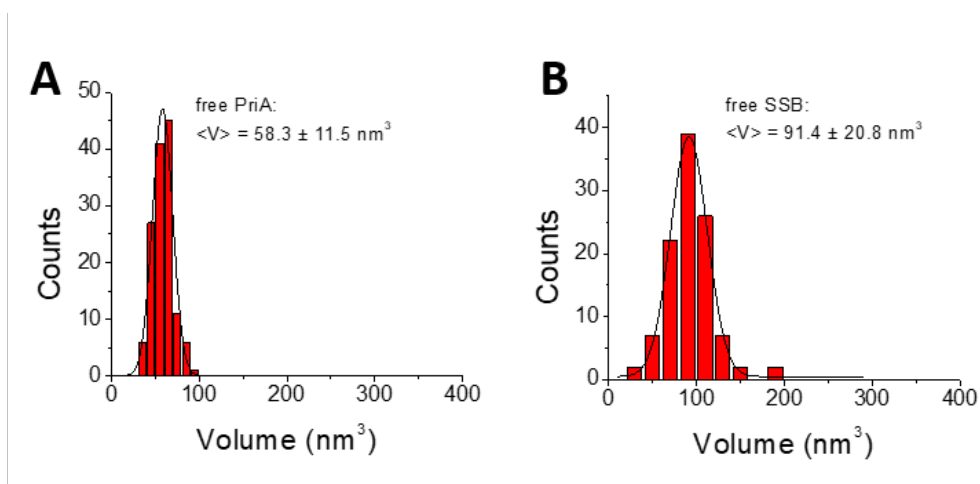


Figure 3.9. Size analysis for free protein: volume distributions fitted by Gaussian for PriA, and SSB, respectively. *A*, the histogram for free PriA protein was centered at $58.3 \pm 11.5 \text{ nm}^3$ (S.D.) by single-peak Gaussian fitting, with a bin size of 10 nm^3 . *B*, the histogram for free SSB was centered at $91.4 \pm 20.8 \text{ nm}^3$ with single-peak Gaussian fitting. The bin size was 20 nm^3 .

3.3.4 The role of the C-terminal of SSB in the protein-protein interaction

It is known that the C-terminal domain of SSB is required for interactome partner binding (87,195). To determine whether the C-terminal domain of SSB is required for PriA loading, we used the SSB Δ C8 protein, which has the acidic tip removed. First, the binding of the SSB mutant to F3 and F5 DNA substrates was assessed. Results show that yield of SSB Δ C8 binding onto each DNA substrate was 83.7% for the F3 DNA substrate and 81.8% for the F5 DNA substrate (Figure 3.10). This is, within experimental error, the same as that observed for wild type. Thus, ssDNA binding for this mutant is unaffected, which is consistent with the previous studies (73,194,196).

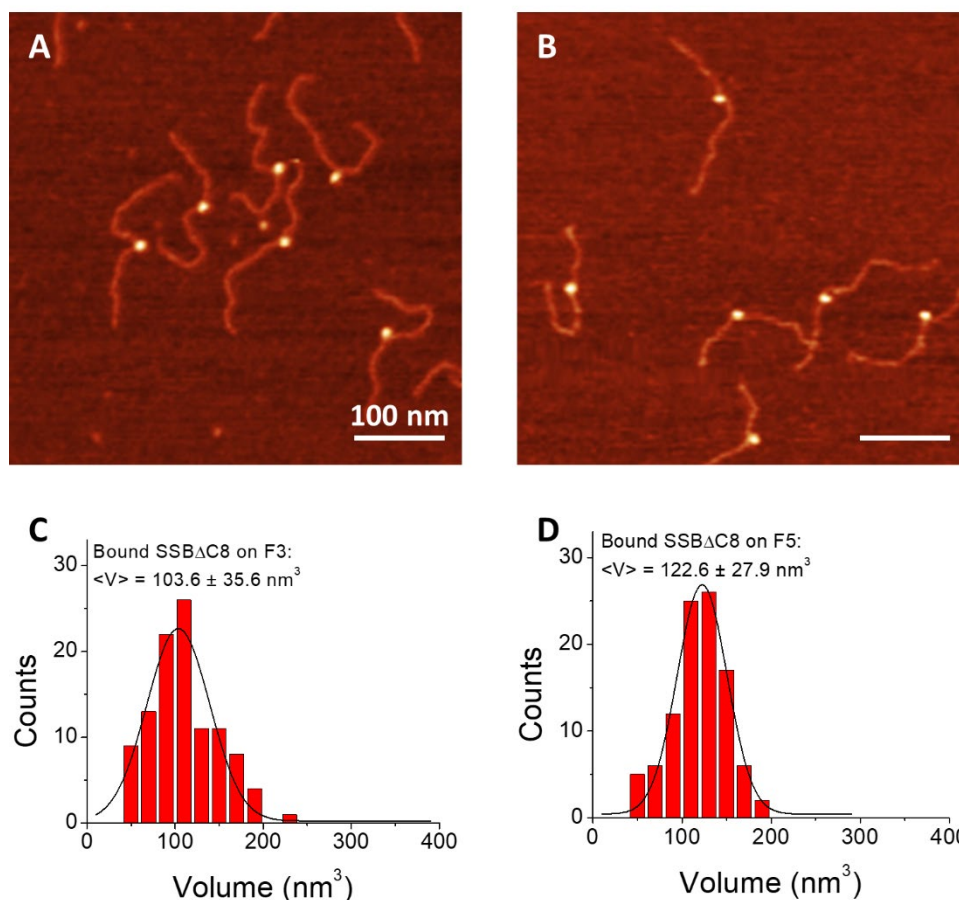


Figure 3.10. AFM results of fork DNA and SSBΔC8 complexes. *A and B*, 0.5 x 0.5 μm AFM images of the F3 DNA substrate with SSBΔC8, the F5 DNA substrate with SSBΔC8, respectively. Z-scale is 3 nm. *C and D*, volume distributions for fork DNA-SSBΔC8 complexes. The bin size was 20 nm³. The histogram of bound SSBΔC8 on the F3 DNA substrate was centered at $103.6 \pm 35.6 \text{ nm}^3$ (S.D.) by single-peak Gaussian fitting. The histogram of bound SSBΔC8 on the F5 DNA substrate was centered at $122.6 \pm 27.9 \text{ nm}^3$. The average volume for SSBΔC8 was $114 \pm 42 \text{ nm}^3$.

In the following experiments, PriA and SSB Δ C8 were mixed in the same way as it was done for the wild-type experiments, then incubated with the DNA substrates and imaged. The yield of double-feature complexes formed on both F3 and F5 DNA substrates was reduced to less than 5%, much lower than that of WT SSB and PriA (Table 3.1). Furthermore, analysis of the sizes of the single-feature complexes revealed that these were bound SSB Δ C8 complexes, as the sizes $97 \pm 26 \text{ nm}^3$ and $111 \pm 31 \text{ nm}^3$ on F3 and F5 DNA substrates, respectively (Figure 3.11). Collectively, these results show that SSB Δ C8 does not interact with PriA or facilitate the loading of PriA onto the DNA.

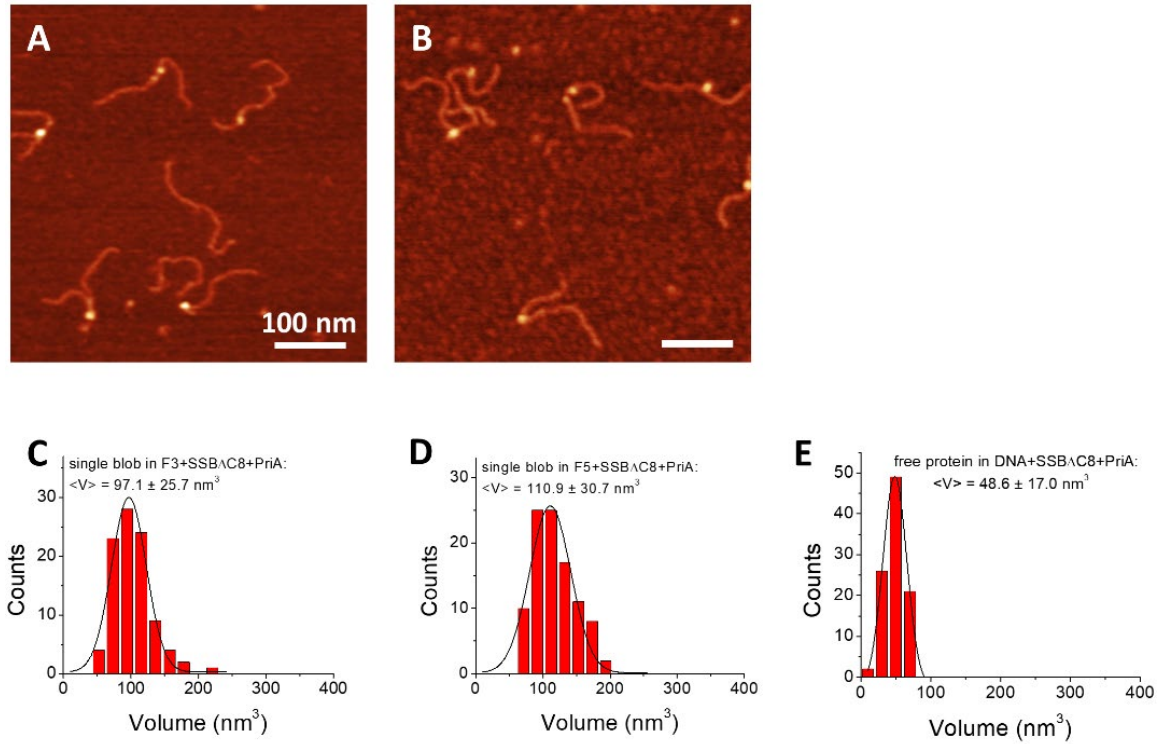


Figure 3.11. SSB Δ C8 does not load PriA. *A and B*, $0.5 \mu\text{m} \times 0.5 \mu\text{m}$ AFM images of the F3 DNA substrate with SSB Δ C8 and PriA, and the F5 DNA substrate with SSB Δ C8 and PriA, respectively. Z-scale is 3 nm. *C*, the volume analysis of the single-feature complexes on the F3 DNA substrate. The distribution was fitted with single-peak Gaussian, and the peak was found to be centered at $97.1 \pm 25.7 \text{ nm}^3$. *D*, the single-peak Gaussian distribution for the single-feature complexes on the F5 DNA substrate. The centered peak is approximated at $110.9 \pm 30.7 \text{ nm}^3$. *E*, the volume distribution for free proteins in the sample of fork DNA substrates mixed with SSB Δ C8 mutant and PriA. The histogram was fitted by Gaussian with a single peak centered at $48.6 \pm 17 \text{ nm}^3$.

We also characterized the role of the C-terminus on the interaction of SSB and PriA in the absence of DNA. The analysis was done for free proteins in the way characterized above. In Figure 3.11 *E*, the volume distribution was fitted by Gaussian with a single peak centered at $49 \pm 17 \text{ nm}^3$, which is different from the multi-peak distribution of free proteins in the wild-type experiments. Thus, the difference between results of PriA with WT SSB and SSB Δ C8 mutant further emphasizes the role of SSB C-terminus in the interactions with its partner protein, that the acidic tip of SSB is needed for the SSB-PriA interaction.

3.4 Discussion

The primary function of PriA is to restart the replication process by facilitating the loading of the replicative DNA helicase, DnaB, onto the stalled replication fork (121). Once bound, PriA exposes ssDNA for DnaB by unwinding the lagging strand or remodeling SSB-coated ssDNA (85,197). This priming process requires the binding of PriA to various DNA structures (16), which was the focus of this paper, as it remains unclear how PriA differentiates among various DNA structures and then plays the role that is needed for the restart of the stalled replication fork. Therefore, we performed studies in the absence of ATP to uncouple the DNA binding property of PriA from its helicase activity.

3.4.1 The role of ssDNA and fork in PriA binding activity

On the fork DNA substrates, PriA binds to both substrates at the fork position, with a preference to the F3 DNA substrate with a nascent lagging strand, which is an unexpected finding. According to previous publications, PriA should bind preferentially to the F5 DNA substrate that has a gap in the nascent lagging strand since it provides a 3'-OH group at the fork junction as the recognition and binding site for the 3'-DNA binding domain of PriA, while the F3 DNA substrate does not (85,187,197). Our finding on PriA's binding preference suggests the participation of the other

domains in PriA-DNA binding. It is in line with the previous finding that PriA binds to the arrested replication fork in a manner independent of a 3'-terminus as well (187). In addition to the independence of polarity, the bend at the fork position may play an important role in PriA binding activity as well, as demonstrated in references (184,198). This emphasizes the essential role of the fork structure and the presence of a nascent lagging strand in the binding of PriA onto the stalled replication fork.

Our model on the role of other PriA domains in the assembly of the complexes with the replication fork is supported by the findings that PriA does not have a binding preference to the polarity of ssDNA in the tailed DNA substrates. Nurse *et al.* demonstrated that PriA bound with high affinity to duplexes with 3'-tails, whereas it did not bind to duplexes with 5'-tails at all (198). However, they detected stable binding of the 3'-extension when the ssDNA tail exceeded 12 nt and high-affinity binding results when the tails were more than 16 nt in length. In our studies, the size of the ssDNA region is 69 nt. Thus, the ssDNA region might also involve in the binding activity of multiple domains and then stabilize the interaction between PriA and DNA substrates. Note that PriA has over 100-fold higher binding yield with the ssDNA region than the blunt end on the tail DNA substrates. This property also contributes to the high efficiency of targeting the stalled replication fork where the restart is needed.

3.4.2 Remodeling of PriA by SSB on the stalled fork

Although the interactions between SSB protein and PriA have already been characterized (86,87,184,191,199), our results revealed a novel role of SSB in the interaction with PriA in the fork DNA substrates. As shown in Figure 3.5, both proteins can be colocalized at the fork position (*insets ii*), where PriA binds to the fork while SSB binds to the ssDNA region. Interestingly, we also identified complexes shown as *insets i* on both images in which SSB and PriA are well separated. On both substrates, SSB locations produce narrow distributions (histograms *C and D* in Figure 3.5). However, the positions of PriA in the SSB-PriA complexes assembled on both

substrates are very broad (Figures 3.5 *E and D*). These data are in contrast with the data obtained from PriA-DNA complexes in the absence of SSB, in which PriA has narrow distribution on each histogram and the peak positions coincide with the location of the fork (Figures 3.4 *E and F*). Thus, we hypothesize that after remodeling, PriA can bind to the DNA duplex with spontaneous translocation over DNA duplexes, comparable to what was observed for RecG (71,72).

Based on the mapping of positions of proteins on the fork substrates in Figure 3.7, PriA shows no preference to the flanks of the F3 DNA substrate (28% on parental strand and 32% on lagging strand). However, on the F5 DNA substrate, which has a gap in the lagging strand, remodeled PriA showed a preference to the leading strand. Note that in the absence of SSB, PriA binds specifically to the fork regions of the fork substrates. These suggest that the SSB-PriA interaction changes the helicase conformation so that PriA becomes capable of binding to DNA duplex, which is similar to the remodeling of RecG protein by SSB proposed by us (71). The translocation mobility of RecG has been proven by direct visualization of RecG mobility using the time-lapse AFM (72). Therefore, it was hypothesized that remodeling of RecG by SSB allows RecG to translocate along the duplex strands in an ATP-independent way so that RecG can be recruited rapidly to accomplish its fork regression role. Recently the protein-protein interaction of SSB with partner protein has been reported for RecQ (191,200,201) and RecOR (202,203), suggesting that the remodeling of components of the DNA replication machinery is a common property of SSB. The remodeling of PriA by SSB facilitates the binding of PriA onto duplex DNA, which is shown in Figure 3.5. Thereby, the binding and/or translocation of PriA along the duplex may stimulate the association of PriA at the stalled replication fork in an ATP-independent way, facilitating the restart process once the ATP is available for PriA helicase activity.

3.4.3 The protein-protein interaction and the effect of SSB tail region on it

PriA interacts with SSB both in the absence and presence of fork DNA substrates. According to published data, the stimulation effect or the localization activity of SSB-PriA interaction requires

an excess of SSB over the helicase (86,87,184,199). In our experiments (Figure 3.8), colocalized PriA-SSB complexes on DNA were detected at a molar ratio of 1:2, SSB-to-PriA, with the concentration of PriA being 5 nM. The volume analysis of colocalized SSB and PriA complexes (Figure 3.8 *A*) was clearly seen for F3 DNA substrate from peak 2, and the yield of such complexes was 24% compared with the single-feature complexes (76%), which correspond to complexes with SSB binding only. Considering that the single-feature complexes count for 78% binding events in the mixture sample (with the rest of events being 7% of free DNA substrates and 15% of double-feature complexes), the overall binding yield of PriA-SSB on F3 DNA should be 0.24×0.78 , which is 18.7%. No such identified peak appears on the F5 DNA substrate (Figure 3.8 *B*), suggesting that the colocalization depends on the substrate structure. On the F3 DNA substrate, which is a better substrate for binding by PriA alone (Table 3.1), the occurrence of colocalization is much higher. In this way, the interaction between SSB and PriA increases the binding of PriA to fork DNA substrates and improves the selectivity of PriA to the more favorable substrate. This suggests that the SSB stimulation effect, as it is known on PriA helicase activity, also plays a role in the binding activities of PriA.

In addition to the protein-protein interaction found in protein-DNA complexes, the volume analysis of free protein (Figure 3.8 *C*) revealed a minor peak (peak 3). It has a larger volume than each protein itself and can be attributed to the complex formed by the SSB-PriA assembly. So, SSB-PriA interaction is independent of the presence of DNA or ATP. This property helps SSB localize or direct PriA to the needed place more efficiently.

Studies showed that most of the interactions between SSB and its partner protein are mediated by the C-terminus of SSB (66,86,204). The C-terminal domain of SSB, corresponding to residues 117-178, can be sub-divided into the intrinsically disordered linker (aa 117-170) and the highly-conserved acidic tip (66). The linker mediates protein-protein interactions while the acidic tip is required to maintain the structure of the C-terminus of SSB so that it does not bind to SSB

itself (194). Thus, when the acidic tip is mutated or deleted, the C-terminus binds to SSB, thereby inactivating the protein. Consequently, SSB-partner interactions are lost. Experiments with the SSB Δ C8 in which the acidic tip of SSB was removed showed that the yield for double-feature complexes dropped, and these findings are in line with the effect C-terminus on the remodeling of RecG (71), suggesting that C-terminus plays an important role in the SSB remodeling of PriA as well.

3.4.4 Conclusion

Our study revealed several novel properties of the interactions of PriA and stalled DNA replication forks, with or without SSB. In the absence of ATP, we observed that PriA binds preferentially to the forked DNA with a gap in the nascent leading strand. Since PriA showed no clear preference towards the polarity of ssDNA in tail DNA substrates, it is the fork structure that plays an essential role in PriA binding. The interactions between SSB and PriA revealed the remodeling of PriA by SSB, which loaded PriA onto the duplex DNA, and this property of SSB can be attributed to its C-terminal segment. It could be an ATP-independent translocation activity by which PriA slides along the DNA duplex and searches for the site needed to get restarted.

Chapter 4. DYNAMICS OF PRIA AT STALLED DNA REPLICATION FORKS

4.1 Introduction

In Chapter 3, we investigated the structure-dependent fork-recognition pattern of PriA in the absence of ATP. We found that the PriA binds preferentially to the F3 DNA substrate, which has a nascent lagging strand, compared to the other forked or tailed DNA substrates. Here we extend our previous studies to the direct visualization of the PriA-DNA dynamics in the presence of ATP.

As discussed before, PriA recognizes the abandoned DNA replication fork in a structure-specific manner and remodels the stalled fork to expose an ssDNA region for the replisome to load. In the presence of ATP, PriA binds and interacts with the three arms of the DNA replication fork (85). PriA requires an ssDNA region (at least 2-nt) to initiate the helicase activity in the 3'-to-5' direction (197,205). In a recent model, the movements of the helicase lobe of PriA have been proposed to enable PriA to “pull in” the lagging strand arm to unwind the duplex (192). In the PriA dominated replication restart pathway, PriA only needs to unwind few base pairs of the lagging strand arm to promote the replication restart (16,182,206). However, there are still some unknown features of PriA: Does the helicase remain bound at the fork position during translocation? How does the ssDNA at fork position regulate the translocation activity?

This chapter shows that most of the PriA molecules are observed bound at the fork in the presence of ATP. However, PriA is capable of translocating over distances as far as several hundred base pairs. On the fork substrate with a nascent lagging strand (the F3 DNA substrate), PriA translocates preferentially onto the parental duplex. When there is an additional 5-nt ssDNA gap on the lagging strand arm at the fork position (the F13 DNA substrate), PriA translocates on both

the parental and lagging arms, with no preference to the 69-nt ssDNA gap over the 5-nt ssDNA gap on the F13 DNA substrate. Time-lapse AFM imaging revealed long-range translocation of PriA and a previously undiscovered property of PriA; PriA can switch to the other DNA strand during translocation on the DNA duplex. By switching the bound DNA template, PriA is able to redirect to the fork position when the DNA substrate lacks an ssDNA gap on the lagging strand arm. In this way, the efficiency of the PriA-mediated DNA replication resumption can be accelerated. These novel features of PriA shed light on the mechanisms of the stalled replication rescue.

4.2 Methods

4.2.1 Purify the proteins

All the proteins in this chapter were provided by Dr. Piero Bianco, University of Nebraska Medical Center. Purification of PriA follows the protocol described in Chapter 3.2.1.

4.2.2 Assemble the DNA substrates

The preparation of the F3 DNA substrate is described in Chapter 3.2.2. Figure 4.1 shows the design of the fork substrates. The construction of the F13 DNA substrate is similar to that of the F3 DNA substrate except for the fork segment. Oligos O30, O31, O32, O33 were annealed to form the core fork segment of the F3 DNA substrate. For the F13 DNA substrate, O31 was replaced by O46 (5'-CGGCTGCGGCGAGCGGTATCAGCTCACTCATA-3') to leave an ssDNA gap on the lagging strand arm at the fork position.

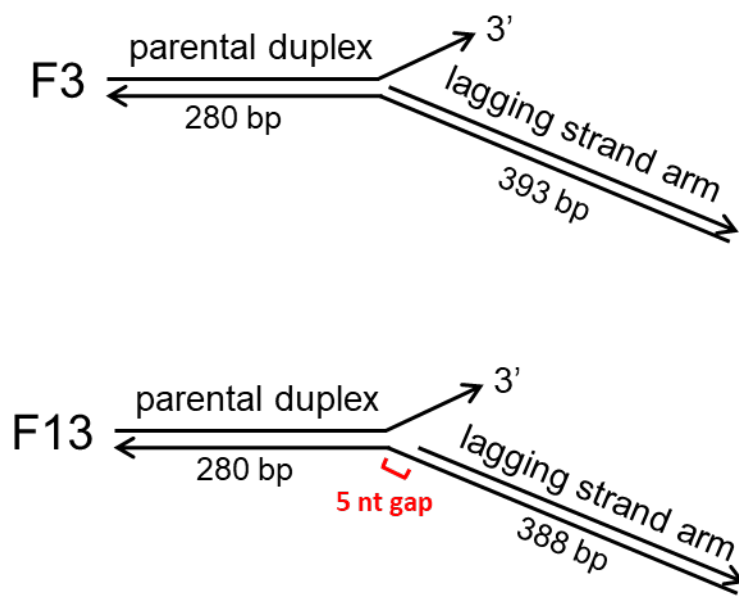


Figure 4.1. DNA substrates designed for this chapter. In the F3 and F13 DNA substrates, the 69 nt ssDNA was placed inside the 673 bp duplex with unequal lengths of the DNA duplex regions, corresponding to the parental duplex (280 bp) and the lagging arm (393bp). The F13 DNA substrate contains a 5-nt ssDNA gap on the lagging arm (388 bp) at the fork position. The gap position is marked in the schematic. Arrows mark the 3'-end of DNA strands.

4.2.3 Preparation of protein-DNA complex

Fork DNA construct (F3 or F13 DNA substrate) was mixed with the PriA separately in a molar ratio of 1:2 and incubated in 10 μ l of binding buffer [10 mM Tris-HCl (pH 7.5), 50 mM NaCl, 5 mM MgCl₂, 1 mM DTT, 1 mM ATP] for 10 min. The complexes were then ready for deposition on the AFM substrates, with a 2 nM final concentration for fork DNA substrates and 1 nM for dsDNA.

4.2.4 Dry sample imaging and imaging in aqueous solution with time-lapse AFM

The dry sample preparation and acquisition are the same as described in Chapter 3.2.4. The sample preparation for time-lapse AFM follows our previous research; A mica disk (1.5 mm in diameter) was glued to the glass cylinder and then attached to the time-lapse AFM stage. The mica was cleaved with tape and functionalized with 167 μ M APS. An aliquot of the sample (2.5 μ l) was deposited on the APS functionalized mica and incubated for 2 min at room temperature. The sample was then rinsed with 20 μ l of binding buffer. Time-lapse images were acquired using a commercial time-lapse AFM instrument (RIBM Co. Ltd., Tsukuba, Japan), with the custom-built, high-aspect-ratio, high-frequency carbon probes manufactured as described in (based on BL-AC10DS, Olympus Corp., Tokyo, Japan). The scan size was set to 300 nm \times 300 nm, and the scan rate corresponding to the data acquisition was 600 ms/frame. The time-lapse HS-AFM movies were read with the Falconview plugin in Igor software (kindly provided by T. Ando) and saved as regular image files. The images were then analyzed using the FemtoScan.

4.3 Results

4.3.1 The ATP-dependent translocation of PriA on the fork substrates

Both F3 and F13 DNA substrates have a 69 nt ssDNA as the template leading strand arm of the fork, shown schematically in Figure 4.1. In the F3 DNA substrate, the single-stranded leading strand is flanked by a 280 bp parental duplex and a 396 bp lagging strand arm, which is the same as the one in Chapter 3. The F13 DNA substrate differs from the F3 DNA substrate by incorporating a 5-nt ssDNA gap on the lagging strand arm at the fork position. The contour length of F3 and F13 DNA substrates were measured, and the data are shown as the histograms in Figures 4.2 *E and F*. The maxima of the contour length were centered at 660 ± 28 bp for the F3 DNA substrate and 669 ± 31 bp for the F13 DNA substrate, which match the design of both DNA substrates. We then prepared the control experiment for the PriA-DNA complexes in the absence of ATP. Figures 4.2 *A-D* shows that PriA binds specifically to the fork position in the absence of ATP, as expected.

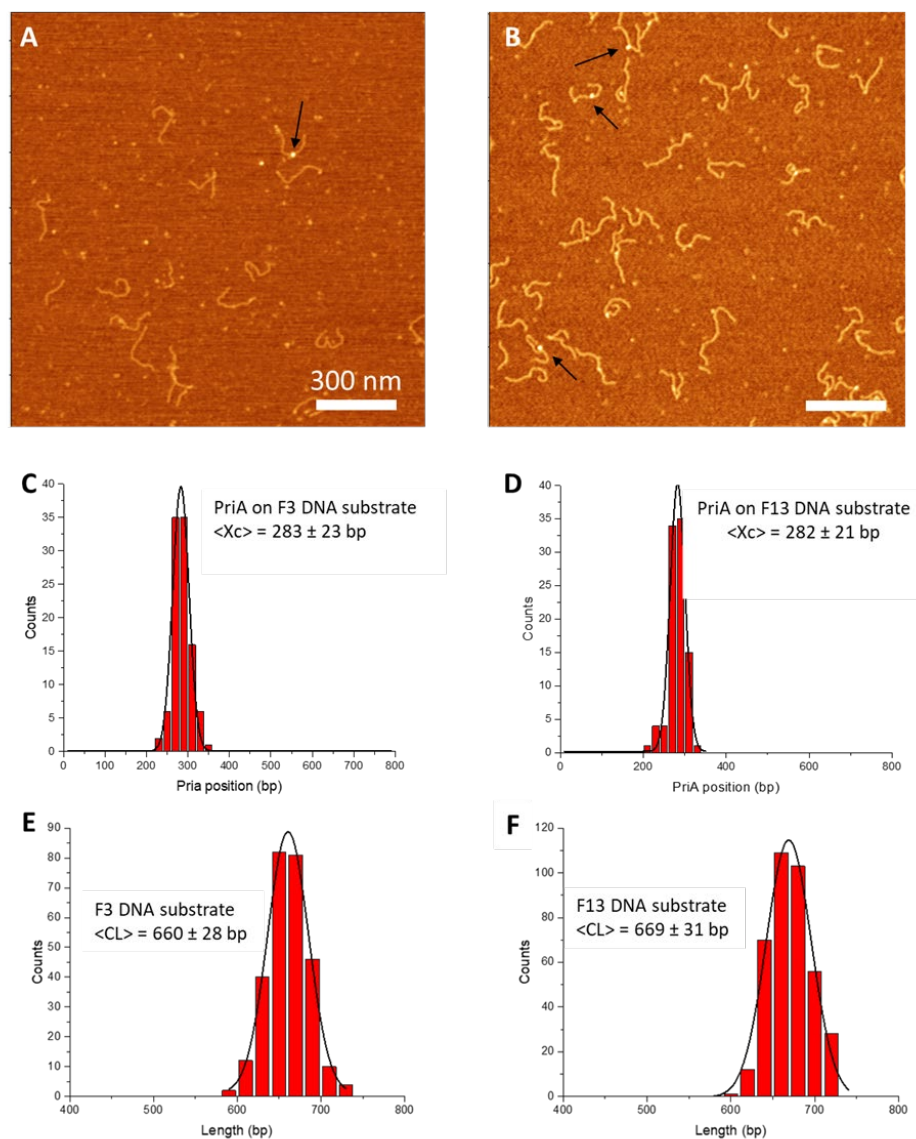


Figure 4.2. The control experiment of PriA mixed with fork DNA substrates in the absence of ATP. *A and B*, the AFM images of PriA on the F3 DNA substrate and the F13 DNA substrate, respectively. Z-scale is 3 nm. Arrows pointed to the PriA-DNA complexes. *C and D*, the histograms for PriA position measurement, approximated by Gaussian distribution with a bin size of 20 bp. *E and F*, the histogram for the DNA contour length measurement.

PriA was mixed with F3 or F13 DNA substrate separately in the presence of ATP and incubated for 10 min at room temperature. The representative images of each assembled protein-DNA complex with zoomed-in snapshots to the right are shown in Figures 4.3 *A and B*. The bright circular features in the images are the complexes of PriA with DNA substrates, as indicated with black arrows. The yields of PriA-DNA complexes in the presence of ATP were $11.3 \pm 1.4\%$ and $14.3 \pm 1.2\%$ for the F3 and F13 DNA substrates, respectively. In snapshots *i* and *iii*, PriA was located at the fork position. In snapshots *ii* and *iv*, PriA was located distal to the fork position of the F3 or F13 DNA substrates, with the fork positions indicated with green arrows. We then mapped the positions of PriA on each substrate (Figures 4.3 *C and E*), with the DNA contour length shown on the y-axis. The position of PriA, indicated by the blue triangles, was measured from the end of the parental duplex to the center of the protein. The parental duplex is the short flank for both substrates, corresponding to the bottom part of the map.

The results in Figure 4.3 *C* show that most of the PriA molecules are bound to the fork position of the F3 DNA substrate ($\sim 80\%$), with the remaining bound to duplex regions ($\sim 20\%$). Furthermore, in Figure 4.3 *D*, the histogram for the PriA position on the F3 DNA substrate, the peak centered at 276 ± 25 bp corresponds to the designed fork position. Based on Figures 4.3 *C and D*, $\sim 80\%$ of PriA are located at the fork position, while $\sim 20\%$ of PriA are non-fork located. In the control experiments (shown in Figure 4.4), PriA does not bind to the duplex DNA (1kb in length) neither in the absence nor in the presence of ATP. Thus, the non-fork locations can be attributed to the ATP-dependent translocation activity of PriA, which can be coupled with the helicase activity.

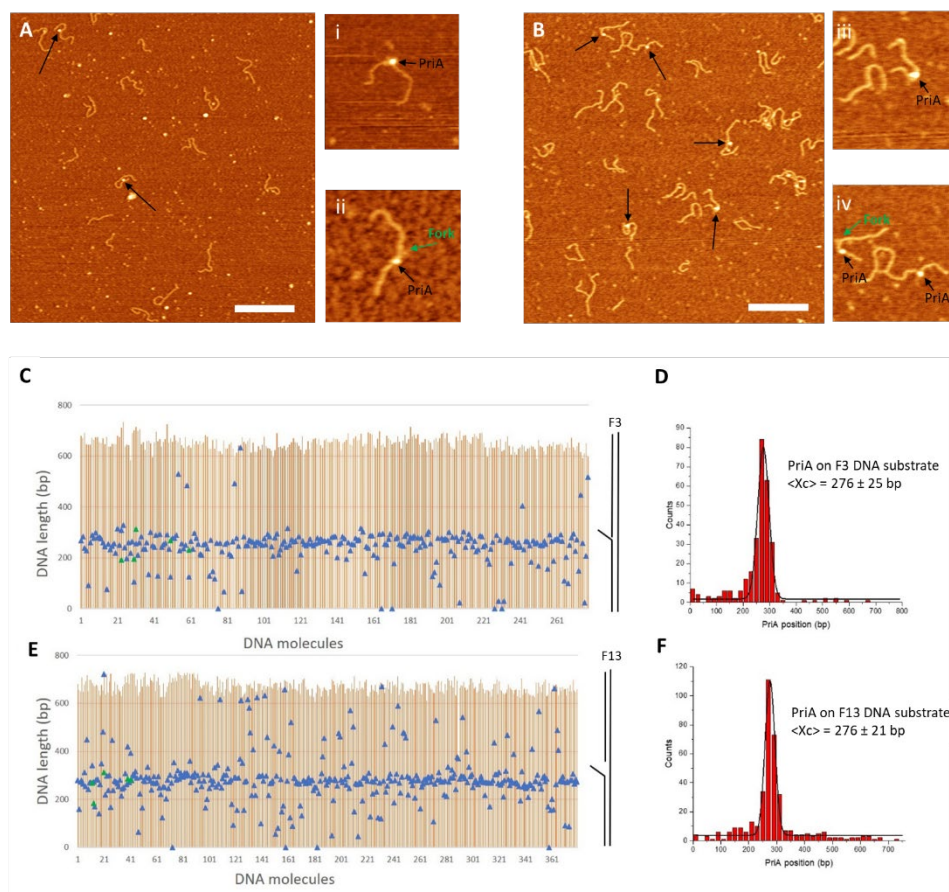


Figure 4.3. The ATP-dependent translocation of PriA on the fork DNA substrates. *A and B*, the typical AFM images of PriA with fork DNA substrates, respectively. Black arrows point to the PriA-DNA complexes. The zoomed images to the right of each panel (300 nm \times 300 nm) show selected PriA-DNA molecules, with the fork position indicated by green arrows. *C and E*, mapping of PriA on each DNA substrate. The schematic of the DNA substrate is present to the right of each graph. Each DNA molecule is aligned to the end of the parental strand, and PriA molecules are represented as blue triangles. When a second PriA is present on a DNA molecule, the triangle is colored green. *D and F*, the distributions for PriA position measured from the end of the parental duplex of each DNA substrate.

Surprisingly, PriA molecules were also observed on the lagging strand arm of the F3 DNA substrate, which account for ~20% of all the non-fork-located complexes. According to the previous studies, PriA requires a small single-stranded gap (two bases or larger) at the fork in order to initiate the helicase activity (42,197). Since there is only one ssDNA gap on the F3 DNA substrate, which is the 69-nt single-stranded leading strand template, we hypothesized that PriA would translocate on the leading strand template in the 3'-to-5' direction. Following this direction, PriA can continue translocating on the parental duplex towards the end. The result of PriA position distribution on the lagging strand arm based on the single-molecule AFM study indicates a potential novel property of PriA that has not been discovered due to the limitation of the other approaches. We will discuss this in Chapter 4.4.3.

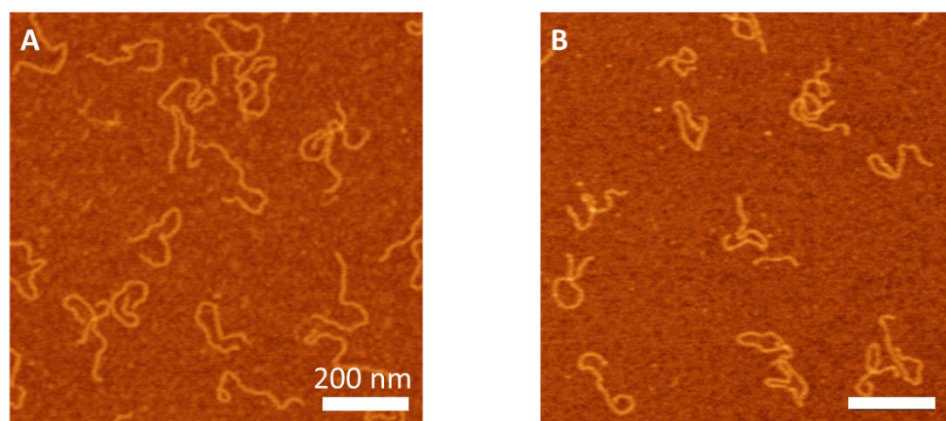


Figure 4.4. The control experiment of PriA mixed with duplex DNA substrate (1036 bp in length). *A*, the AFM image of PriA with the duplex DNA substrate in the absence of ATP. *B*, the AFM image of PriA with the duplex DNA substrate in the presence of ATP.

The results in Figures 4.3. *B and E* show that, similar to the complexes on the F3 DNA substrate, the majority of PriA molecules are bound at the fork of the F13 DNA substrate. According to Figure 4.3 *F*, 60% of the PriA molecules are bound to the fork position, as shown by the Gaussian distribution with a peak centered at 276 ± 21 bp. In contrast to the F3 DNA substrate, the non-fork-located PriA molecules on F13, which count for the rest 40% of molecules examined, were distributed equally on the parental duplex and the lagging strand arm. This is due to the additional 5-nt ssDNA gap on the lagging strand template at the fork position that allows PriA to initiate its helicase activity on the lagging strand and translocate towards the end of the lagging strand arm following the 3'-to-5' direction. Since PriA shows no preference for translocating along the parental strand over the lagging strand of the F13 DNA substrate, the sizes of the ssDNA gap, which are 69-nt on the leading strand and 5-nt on the lagging strand, do not affect the direction of PriA translocation activity.

In addition to the complexes with one PriA molecule bound, a small fraction of the complexes contain two PriA molecules (Figure 4.3 *A*, molecules #22, 29, 50, and 64; Figure 4.3 *B*, molecules #12, 19, and 43). These can result from two PriA molecules binding sequentially, followed by translocation over the duplex arms.

4.3.2 The visualization of PriA translocation in the presence of ATP

The mapping data suggest that PriA can translocate away from the fork position over a hundred base pairs in the presence of ATP. To directly visualize the translocation of PriA, we performed time-lapse AFM experiments with the high-speed AFM. In these experiments, PriA was mixed with the F13 DNA substrate in the binding buffer [10mM Tris-HCl (pH 7.5), 50 mM NaCl, 5 mM MgCl₂, 1 mM DTT, 1mM ATP] for 10 minutes at room temperature. The mixture was deposited onto the APS mica, incubated for 2 minutes, and rinsed with the binding buffer before scanning. The sample was imaged under aqueous buffer conditions to obtain the dynamics of the PriA–DNA

interactions. The scan rate of a typical image ($300 \times 300 \text{ nm}^2$) was 600 ms. Movies were assembled after the frame-by-frame recording of each selected complex of interest.

Figure 4.5 *A* displays the frames demonstrating the PriA translocation activity on the lagging strand arm of the F13 DNA substrate. The black arrows direct to PriA, and the green arrows indicate the fork position when it is visible. In Figure 4.5 *B*, the traces of complexes from the frames in Figure 4.5 *A* are shown for clarity. PriA translocated away from the fork position towards the end of the lagging strand arm and ended with dissociation from the DNA. The position of PriA measured from the end of the parental strand is shown in Figure 4.5 *C* (the black curve), which demonstrates that PriA translocated gradually on the lagging strand arm for ~ 100 bp from frames 6 to 11. Then PriA appeared to stay motionless between frames 11 and 17, followed by a rapid translocation during frames 17 to 20 over a distance of ~ 100 bp. After that, PriA dissociated from the DNA substrate. The grey curve in Figure 4.5 *C* shows the PriA position measured from the end of the lagging strand arm. To determine whether the changes in the DNA contour length accounts for the difference in the position of PriA instead of the active translocation, we measured the DNA contour length in each frame, shown as the blue curve in Figure 4.5 *C*. It is shown that the DNA contour length remains constant, except for frames 17 and 18. The decrease in the contour length measurement in these frames is caused by the end of the lagging strand arm floating up from the mica surface, as the PriA position measured from the end of the parental duplex did not change from frame 16 to 17. Since the DNA contour length remains constant and PriA is observed in different positions, we conclude that the changes in PriA position were due to ATP-dependent PriA translocation on the lagging strand arm.

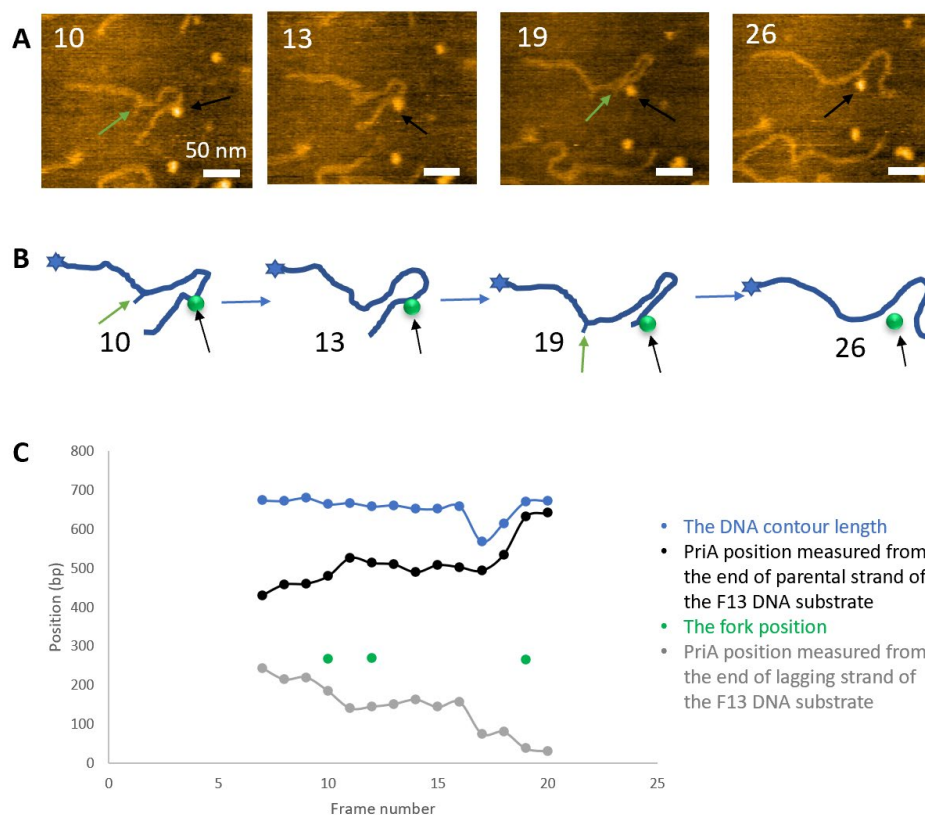


Figure 4.5. Time-lapse AFM data of PriA translocation on the lagging strand arm of the F13 DNA substrate. *A*, the selected frames from the HS-AFM movie. The black arrows point to the PriA locations, while the green arrows point to the fork position when it is visible. *B*, traces of the complexes shown in *A*, corresponding to each frame. The F13 DNA substrate and PriA are colored blue and green, respectively. The stars mark the end of the parental arm. *C*, the position measurement of PriA on the F13 DNA substrate. The green dots mark the fork position when the fork is visible. The blue, black, and grey curves show the DNA contour length, PriA position measured from the end of the parental arm and from the end of the lagging arm, respectively.

Translocation activities of PriA on the parental duplex of the F13 DNA substrate were also observed (Figure 4.6). The selected frames from the HS-AFM movie are shown in Figure 4.6 *A*, with the traces of the complex placed below each frame for clarity (Figure 4.6 *B*). PriA remained bound at a position near the end of the parental duplex from frames 1 to 16. A burst in translocation occurred between frames 16 to 17, where PriA translocated toward the fork position over ~100 bp (Figure 4.6 *C*). After that, PriA remained motionless until it dissociated from the DNA substrate. As we discussed in the previous section (Chapter 4.3.1), PriA can translocate to the parental duplex from the leading strand template. It can also translocate on the lagging strand arm toward the end of the lagging strand arm, following the 3'-to-5' direction. However, in this movie, PriA translocated toward the fork position, in the direction contrary to either case discussed above. This observation further suggests that PriA might have a novel property, as mentioned in Chapter 4.3.1, allowing PriA to translocate in the opposite direction as expected.

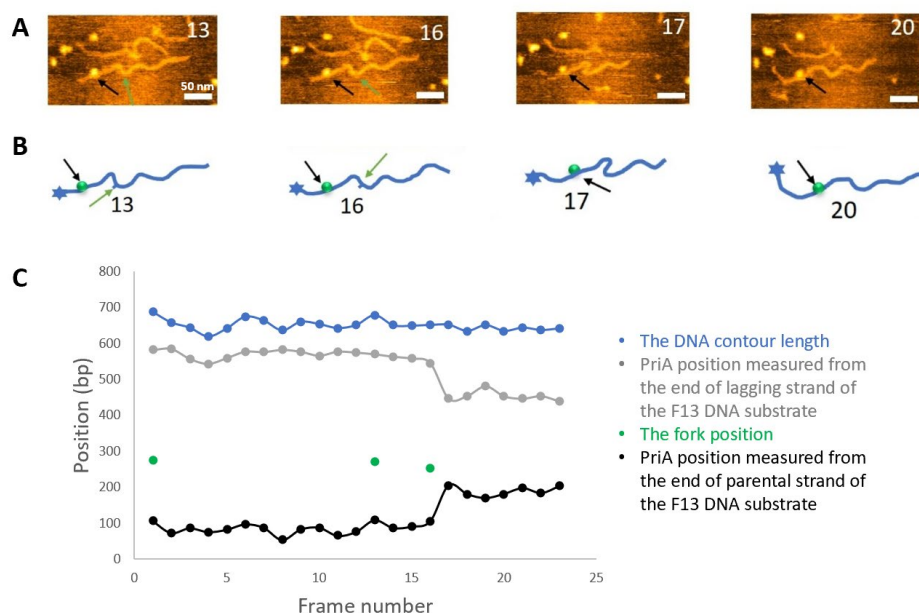


Figure 4.6. Time-lapse AFM data of PriA translocation on the parental duplex of the F13 DNA substrate. *A*, the selected frames from the HS-AFM movie. The black arrows point to the PriA locations, while the green arrows point to the fork position when it is visible. *B*, traces of the complexes shown in *A*, corresponding to each frame. The F13 DNA substrate and PriA are colored blue and green, respectively. The stars mark the end of the parental arm. *C*, the position measurement of PriA on the F13 DNA substrate. The green dots mark the fork position when the fork is visible. The blue, black, and grey curves show the DNA contour length, PriA position measured from the end of the parental arm and from the end of the lagging arm, respectively.

In addition to the observation of PriA translocation in different directions, the changes in the translocation direction were also directly visualized. The data in Figure 4.7 *A* show a few frames from the HS-AFM movie, with the traces of the complex placed below each frame for clarity (Figure 4.7 *B*). The quantitative analysis is shown in Figure 4.7 *C*, which is the position measurement of PriA as a function of time. The black curve indicates the PriA position measured from the end of the parental duplex, while the grey curve shows the PriA position measured from the end of the lagging arm. The blue curve corresponds to the DNA contour length measurement, which shows relatively low time-dependent variability of the DNA length. However, the position of PriA changes non-monotonously. Initially, PriA translocated toward the end of the lagging strand arm, from frames 35 to 47, over ~180 bp. PriA then changed its direction, translocating back toward the fork position, from frames 51 to 56. During frames 57 to 80, PriA did not change its position. After that, PriA translocated away from the fork for 200 bp on the lagging strand arm (frames 80 to 90). From frame 100, PriA changed its direction again and translocated for 100 bp back toward the fork position.

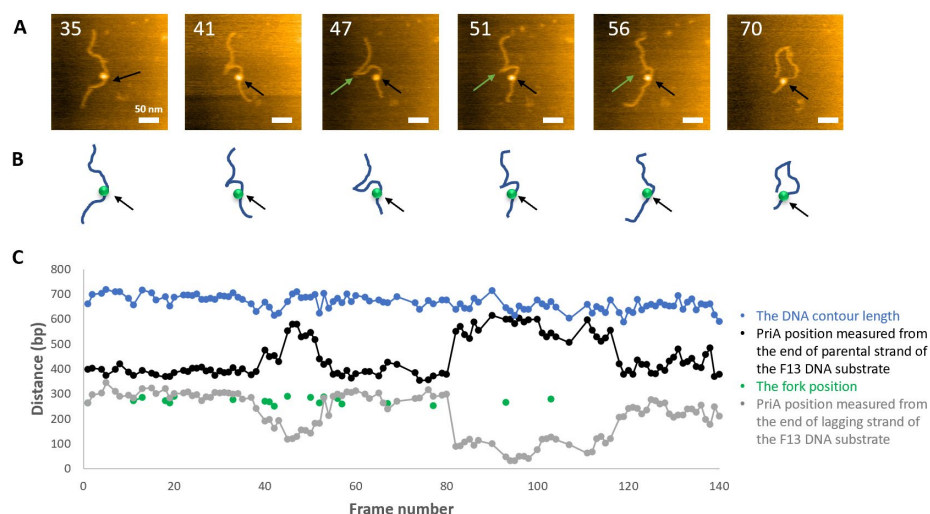


Figure 4.7. Time-lapse AFM data of PriA translocation on the lagging strand arm of the F13 DNA substrate. *A*, the selected frames from the HS-AFM movie. The black arrows point to the PriA locations, while the green arrows point to the fork position when it is visible. *B*, traces of the complexes shown in *A*, corresponding to each frame. The F13 DNA substrate and PriA are colored blue and green, respectively. The stars mark the end of the parental arm. *C*, the position measurement of PriA on the F13 DNA substrate. The green dots mark the fork position when the fork is visible. The blue, black, and grey curves show the DNA contour length, PriA position measured from the end of the parental arm and the end of the lagging arm, respectively.

Thus, the time-lapse AFM experiments provided direct evidence for the long-range translocation of PriA and revealed that the direction of translocation could change. Since PriA unwinds DNA in the 3'-to-5' direction, the change in the translocation direction indicates that PriA can switch between DNA strands in the duplex during the translocation.

4.4 Discussion

The AFM studies in this chapter revealed three novel properties of PriA in complex with the stalled replication fork in the presence of ATP; (1) the specificity of PriA in binding to the different fork DNA molecules with and without gaps at the fork position; (2) the ATP-dependent dynamics of PriA at the fork position and the long-range translocation of PriA mediated by ATP hydrolysis, and (3) DNA strand switching by PriA during translocation.

4.4.1 The specificity of PriA in binding to fork DNA

According to Chapter 3, PriA binds specifically to the fork position in the fork DNA substrates in the absence of ATP, with no detectable binding to the duplex DNA. This is consistent with previous studies that fork binding is essential for PriA to initiate the replication restart (184,185,197,198,207,208). In Figure 4.2, the control experiments also show that PriA binds exclusively to the fork position of both F3 and F13 DNA substrates in the absence of ATP. Furthermore, the control experiments in Figure 4.4 suggest that PriA does not bind to the duplex DNA regardless of the presence of ATP.

In the presence of ATP, PriA unwinds a few base pairs of the lagging strand arm to facilitate the binding of DnaB and the further loading of the rest of the replication machinery onto the stalled replication fork (122,209). There are two conceivable ways for PriA to process the fork DNA substrates for DnaB. In one way, PriA binds to the fork position by placing the helicase domain on the 69-nt template leading strand (185). This allows PriA to translocate from the fork position

toward the parental arm, following the 3'-to-5' direction. Alternatively, PriA binds to the fork position with the helicase domain positioned on the lagging strand arm (189). Then, PriA would translocate along the lagging strand arm away from the fork position if there is a small ssDNA gap on the lagging strand. The second way is available for the complexes on the F13 DNA substrate exclusively, because the F3 DNA substrate does not have an ssDNA region on the lagging strand required to initiate the ATP-dependent helicase activity. Additional interactions involving the winged-helix domain and the 3'-DNA binding domain further stabilize the binding of PriA to the fork position.

The results in Figure 4.3 shows that PriA is mainly located at the fork position of both fork DNA substrates in the presence of ATP. As we discussed, PriA only needs to unwind several base pairs of the lagging strand arm for DnaB to load. However, the expected unwinding activity (up to 5 bp) is too subtle to be detected in our system. According to the histograms (Figures 4.3 *D and F*), the peaks can be partially attributed to the unwinding of a small region of the duplex DNA at the fork position. Based on Keck's model, PriA unwinds the duplex DNA by "pulling" the DNA across the helicase domain and couples the protein-protein interaction to the helicase activity, hereby loading the replisome onto the abandoned fork substrate (192). So, the peak in the histograms can also be due to this specific unwinding pattern. However, 20% of the overall PriA-DNA complexes are non-fork located on the F3 DNA substrate. On the F13 DNA substrate, the non-fork located PriA count for 40% of the overall complexes. These non-fork-located complexes suggest that PriA can translocate over large distances as well. We will discuss this in the next section (Chapter 4.4.2).

4.4.2 The ATP-dependent translocation and dynamics of PriA

The translocation of PriA is directly visualized by the static experiments (Figure 4.3) and the time-lapse AFM experiments (Figures 4.5, 4.6, and 4.7). Figure 4.3 reveals the partition of PriA translocation on the parental duplex and the lagging strand arm of the fork DNA substrates. On the F3 DNA substrate (Figures 4.3 *A, C, and D*), most of the non-fork-located PriA translocated onto

the parental duplex. However, there are 20% of the non-fork-located PriA translocating on the lagging strand arm, whereas on the F13 DNA substrate, there is almost no preference for PriA translocating to the parental duplex over the lagging strand arm (Figures 4.3 *B*, *E*, and *F*). The difference in the translocation activities could arise from the specific fork structure at each DNA substrate.

PriA requires at least 2 nt of ssDNA region (197) to initiate the helicase activity and there is only one ssDNA region on the F3 DNA substrate; therefore, the helicase domain of PriA binds to the 69-nt ssDNA at the fork, translocating onto the parental duplex from the template leading strand, in the 3'-to-5' direction. The F13 DNA substrate contains an extra 5-nt ssDNA region on the lagging strand arm at the fork position. This allows PriA to translocate on the F13 DNA substrate in two different ways. In one way, PriA initiates the helicase activity from the 69-nt single-stranded leading strand template, translocating onto the parental duplex in the 3'-to-5' direction. In another way, PriA starts the helicase activity from the 5-nt ssDNA gap on the lagging strand template, translocating toward the end of the lagging strand arm, in the same 3'-to-5' direction. Since PriA translocates on the parental and lagging arms of the F13 DNA substrate in an almost equal ratio, it suggests that PriA originally initiates unwinding with no preference to the 5-nt ssDNA gap over the 69-nt ssDNA gap at the fork position. This is consistent with the data of PriA unwinding activity in bulk, which shows a similar unwinding efficiency of PriA on the parental duplex and lagging strand arm (52% on the parental duplex, 46% on the lagging strand arm, and 2% on both duplex regions) (197).

However, 20% of PriA translocated from the fork to the lagging strand arm of the F3 DNA substrate. This is similar to an earlier finding that PriA mostly unwound the parental arm of a substrate with shorter duplex regions compared to the F3 DNA substrate (197). There were also 10% of the lagging strand arm unwound by the helicase activity. These can be assigned to the DNA

breathing at the fork, which provides the affinity of PriA to the lagging strand arm to some degree. Alternatively, it can be a novel property of PriA that enables it to alter the translocation activity.

Furthermore, the data in Figure 4.3 shows PriA located far away from the fork position, which can be as distant as several hundred base pairs. No such complexes have been found from the control experiments performed in the absence of ATP (Figure 4.2). These data are consistent with the ATP-dependent translocation of PriA that results in fork-distal positions. However, it conflicts with the model proposed by Keck that PriA remains bound at the fork position and unwinds the duplex DNA (192).

4.4.3 The strand-switching property of PriA

The results from time-lapse AFM revealed a previously undiscovered property of PriA- the capability to alter the direction of the translocation by switching the bound-DNA template during translocation. Figures 4.5, 4.6, and 4.7 reveal that PriA can move towards and away from the fork position. The data in Figure 4.7 show that initially, the PriA translocated away from the fork position and then translocated towards the fork, which was in the opposite direction. These data also show that PriA altered the translocation direction multiple times. Since PriA translocates in the 3'-to-5' direction, and it does not bind to dsDNA, the changes in translocation direction could result from strand switching or from backtracking along the same DNA strand, as discovered for HIM-6 (210). Typically, backtracking occurs over a few unwinding steps. However, in Figure 4.7, PriA translocated away and towards the fork over a distance of ~200 base pairs. Therefore, the changes in the translocation direction are due to the strand-switching property of PriA. This explains why PriA was observed on the lagging strand of the F3 DNA substrate; originally, PriA translocates along the template leading strand toward the parental duplex, then it switches to the other DNA template, translocating back to the fork position. In the experiments with no other proteins present in the microenvironment, PriA does not pause for DnaB loading. Instead, it continues translocating along the template lagging strand after switching the template strand. The

strand-switching property is not without precedent. It has been observed at the single-molecule level for UvrD, a helicase that unwinds DNA duplex in the 3'-to-5' direction (211).

4.4.4 Conclusion

In conclusion, several novel properties of PriA in the ATP-dependent helicase activity were revealed in this chapter. We have shown that PriA remains mainly bound to the fork position in the presence of ATP. This corresponds to the previous studies and supports the recent model that PriA stays bound at the fork while unwinding the duplex DNA. However, the motor function of PriA drives it away from the fork position, translocating over distances as large as 400 bp. Importantly, PriA can translocate on both the parental duplex and the lagging strand arm of the DNA substrates, with the final direction dictated by the fork structure. PriA originally initiates unwinding with no preference to the 5-nt ssDNA gap over the 69-nt ssDNA gap at the fork position. Finally, we found that PriA can switch the bound-DNA strand to the other DNA strand during translocation, allowing it to change the translocation direction. As a result, PriA is capable of moving towards and away from the fork position. It is conceivable that strand switching serves to redirect PriA back to the fork position when the ssDNA gap is not present on the lagging strand so that the resumption of DNA replication can be directed to the lagging strand arm of the fork. In addition, it may also serve to clear the DNA near the fork position to ensure the unobstructed reloading of the replisome.

Chapter 5. RESTRICTION OF RECG TRANSLOCATION BY DNA MISPAIRING

5.1 Introduction

RecG is a monomeric DNA helicase that binds and regresses stalled DNA replication forks. In the process, it couples DNA unwinding to duplex rewinding, resulting in the extrusion of Holliday Junctions (34,41,205). For regression to occur, RecG forms an intimate complex with the stalled fork (212). Here, the wedge domain of RecG binds to the fork region, while the helicase domains are predicted to bind to the parental duplex ahead of the fork. Modeling of RecG revealed that it unwinds the replication fork through a structural transition with the helicase domains by hydrolyzing ATP. In addition to RecG, SSB plays an essential function in fork rescue by enhancing and controlling the activity of RecG in the early stages of the reaction (70,86,116,213).

We have used AFM to understand the functions of RecG and SSB on a designed stalled replication fork (71,72). We demonstrated that the interaction of fork-bound SSB leads to remodeling of RecG during the loading process. As a result, RecG becomes capable of spontaneous translocation ahead of the replication fork over distances as large as 200 bp, and this was directly visualized by HS-AFM (72). During translocation, the helicase domains unwind the dsDNA in a 3'-to-5' direction, and regression is inhibited by reversing the polarity of the phosphate backbone in either leading or lagging strands (41). Since the helicase domains are essential to the movement of RecG and translocation is inhibited by the altered phosphodiester backbone, it is conceivable that duplex imperfections, such as those induced by DNA damaging agents or a failure to correct errors during DNA replication, may impair the interaction of RecG with a stalled DNA replication

fork. This may function as a signal to RecG that the fork structure is compromised so that instead of regressing the fork, RecG dissociates.

To test this, we assembled the fork DNA substrates with duplex imperfections in the parental duplex. The duplex imperfections include a C-C mismatch or a G-bulge, positioned either 10 or 30 bp upstream of the fork. These positions are either within or outside the footprint of the helicase bound to a fork (212,214). Results herein show that when a duplex imperfection is placed 10 bp from the fork, the binding efficiency of RecG is negatively impacted and cannot be rescued by SSB to the levels observed for undamaged DNA. In contrast, a G-bulge or C-C mismatch placed 30 bp from the fork does not affect RecG binding in the absence or presence of SSB. Instead, these duplex distortions restrict RecG sliding to the region between the duplex imperfections and the fork itself. Collectively, these data show that DNA substrates with damage in the immediate vicinity of the fork position will likely not be repaired by a fork regression pathway, as the damage impairs the binding of RecG to the fork resulting in an inability to regress the stalled fork.

5.2 Methods

5.2.1 Purify the proteins

All the proteins in this chapter were provided by Dr. Piero Bianco, University of Nebraska Medical Center.

RecG protein was purified as described previously (71). Briefly, the protein was eluted from a 100 ml Q-Sepharose column equilibrated in buffer A [20 mM Tris-HCl (pH 8.5), 1 mM EDTA, 1 mM DTT, 10 mM NaCl], using a linear salt gradient (10–1000 mM NaCl), with RecG eluting between 250 and 360 mM NaCl. The pooled fractions were then subjected to heparin FF and hydroxyapatite chromatography. Pooled fractions from the hydroxyapatite column were dialyzed overnight in S buffer [10 mM KPO₄ (pH 6.8), 1 mM DTT, 1 mM EDTA and 100 mM

KCl]. The protein was applied to a 1 ml MonoS column and eluted using a linear KCl gradient (100–700 mM) with RecG eluting at 350 mM KCl. The fractions containing RecG were pooled and dialyzed overnight against storage buffer [20 mM Tris-HCl (pH 7.5), 1 mM EDTA, 1 mM DTT, 100 mM NaCl and 50% (v/v) glycerol]. The protein concentration was spectrophotometrically determined using an extinction coefficient of $49,500 \text{ M}^{-1} \text{ cm}^{-1}$ (71).

SSB protein was purified from strain K12 Δ H1 Δ trp as described previously (86). The concentration of the purified SSB protein was determined at 280 nm using an extinction coefficient of $30,000 \text{ M}^{-1} \text{ cm}^{-1}$. The site size of SSB protein was determined to be 10 nucleotides per monomer by monitoring the quenching of the intrinsic fluorescence of SSB that occurred on binding to ssDNA(116,213).

5.2.2 Assemble the DNA substrates

The fork DNA substrates were assembled from two duplexes and the core fork segment, following our previous methodology. The difference in the assembly of the F3 DNA substrate and the mismatching DNA substrates (F6, F7, and F8 DNA substrates) is the core segment. To assemble the core segment of the F6 DNA substrate, O33 was replaced by O35 (5'-CACTGACTCCCTGCGCAAGGCTAACAGCATCACACACATTAACAATTCTAACATCTGGTTTTTCATTCTTTGGGTTTCACTTTCTCCAC-3'). To assemble the core segment of the F7 DNA substrate, O30 was replaced by O30-bulge (5'-TCATCTGCGTATTGGGCGCTCTTCGCGCTTCCTATCT-3'). For the F8 DNA substrate, O30 was replaced by O30-mismatch (5'-TCATCTGCGTATTGGGCGCTCTTCCCCTTCCTATCT-3').

5.2.3 Prepare the protein-DNA complexes

SSB/DNA complex was prepared by mixing the SSB tetramer with the DNA substrates (molar concentration: 20 nM) in a molar ratio of 2:1, and incubated in 10 μ l of binding buffer [10 mM Tris-HCl (pH 7.5), 50 mM NaCl, 5 mM MgCl₂, 1 mM DTT] for 10 min at room temperature.

RecG/DNA complex was prepared by mixing RecG with the DNA substrate (molar concentration: 20 nM) in a molar ratio of 4:1, and incubated in 10 μ l of binding buffer for 10 min at room temperature.

SSB/RecG/DNA complex was prepared by mixing SSB tetramer (concentration: 20 nM) and DNA in the molar ratio of 1:2 in 30 μ l of binding buffer for 10 min at room temperature. The RecG protein (4:1 molar ratio to DNA) was added into the mixture and incubated for an additional 30 min. The final molar ratio of DNA: SSB: RecG was 1:2:4, and the final DNA concentration was 2 nM before deposition.

5.2.4 Acquire and analyze the AFM images

1-(3-aminopropyl) silatrane (APS) functionalized mica was prepared as described in Chapter 2.3.4 and used as the AFM substrate for all experiments. 10 μ l of the sample were deposited onto the APS functionalized mica for two minutes. The mica was then rinsed with DDI H₂O and dried with a gentle argon flow. Images were acquired using tapping mode in the air on a MultiMode 8, Nanoscope V system (Bruker, Santa Barbara, CA) using TESPA probes (320 kHz nominal frequency and a 42 N/m spring constant) from the same vendor.

The dry sample AFM images were analyzed using the FemtoScan Online software package (Advanced Technologies Center, Moscow, Russia). The SSB positions were measured from the end of the short arm to the center of the protein. The DNA contour length was then obtained by continuously measuring to the other end of the DNA substrate. The yield of protein-DNA complexes was calculated from the ratio of the number of complexes to the total number of DNA molecules.

5.3 Results

The DNA substrates that have lesions on the parental strand of the stalled DNA replication forks are shown in Figure 5.1. We took the F3 DNA substrate as a control, as the duplex regions are of different lengths, which allows us to distinguish between the parental and lagging strand arms of the fork in AFM images (71). This fork was used to study RecG binding activities and SSB-RecG interactions, representing the preferred fork substrate for RecG, as shown previously (41,42,72,205). The F6, F7, and F8 DNA substrates are similar to the F3 DNA substrates, except for the addition of a mismatch or bulge in the parental duplex region. The F6 DNA substrate contains a C-C mismatch at 10 bp upstream of the fork position. The F7 DNA substrate contains a single G-bulge on the parental arm positioned 30 bp upstream of the fork, while the F8 DNA substrate contains a C-C mismatch at the same position. The C-C mismatch can change the local structure of DNA- inducing global helical bending or opening, and affecting the depth and width of minor groove in the center of the helix (215,216). The G bulge in the F7 DNA substrate contains an extra G on one DNA strand, and there are two C bases, one on each side of G, which makes it less stable than other lesions (217). The mismatch or bulge positions were designed to be within the RecG thermal sliding distance of SSB bound to a fork (71,72,214). Furthermore, the 10 bp imperfection is within the RecG-fork footprint, whereas the 30 bp imperfections are outside this region (212,214).

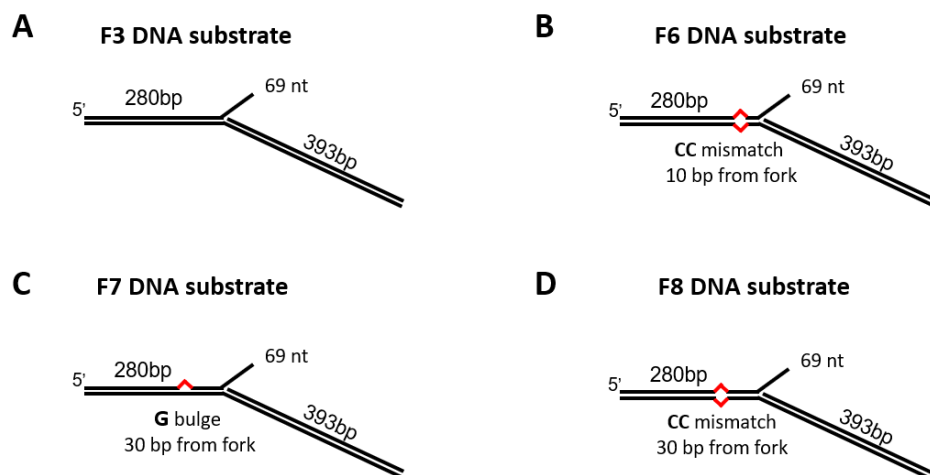


Figure 5.1. The design for the lesions in the stalled replication fork. *A*, the original F3 DNA substrate, which contains 69 nt ssDNA between the two perfectly paired DNA duplexes (280bp and 393bp). *B*, the F6 DNA substrate, containing the C-C mismatch on the parental duplex at 10 bp away from the fork position. *C*, the F7 DNA substrate, containing a single G bulge at 30 bp upstream of the fork. *D*, the F8 DNA substrate, having a C-C mismatch on the parental duplex at 30 bp away from the fork.

5.3.1 The interaction between SSB and RecG on the designed fork DNA substrates

As shown in Figure 5.2, both SSB and RecG can be observed bound to the same DNA molecule (indicated by the black arrows) in the absence of ATP. SSB and RecG can be readily discerned based on the size analyses; this is presented in the insets of Figure 5.2, with the larger feature being SSB (blue arrow) and the smaller being RecG (red arrow). Furthermore, for most DNA molecules with both proteins bound, SSB and RecG are at distinct positions and seldom colocalize. There are some DNA molecules with only a single feature, and analysis shows that these are SSB-DNA complexes.

To assess the ability of SSB to load RecG onto the fork substrates, we measured the yield of protein-DNA complexes in RecG only and SSB-RecG experiments. Results show that the yield of RecG complexes is higher when SSB is added first compared to when there is RecG only (Figure 5.2 *E*). The graph shows that when duplex imperfection is positioned 10 bp from the fork (the F6 DNA substrate), binding of RecG is inhibited 2-fold, regardless of the presence of SSB. In contrast, when the duplex imperfection is positioned 30 bp away from the fork, RecG binding with or without SSB loading is unaffected, with F7 and F8 DNA substrates producing yields similar to that on the F3 DNA substrate. This suggests that when the imperfection is within the RecG-fork footprint, helicase binding is impaired. Additionally, this also indicates that the initial loading site of RecG by SSB encompasses 10 base pairs from the fork.

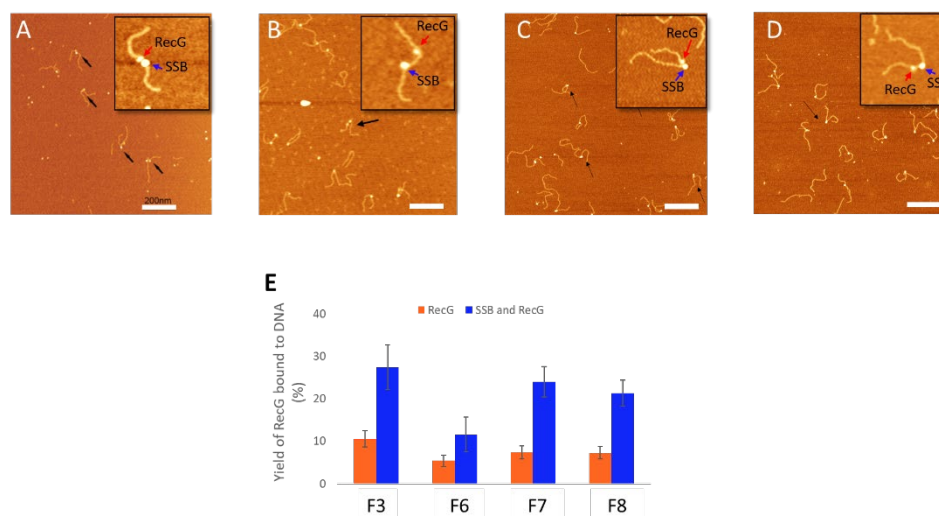


Figure 5.2. AFM analyses of the RecG-SSB-DNA complexes on each DNA substrate in the absence of ATP. *A-D*, the AFM images of SSB and RecG on the F3, F6, F7 and F8 DNA substrate, respectively. The scale bar is 200 nm. Black arrows point to the double-protein complexes. The insets (200 nm × 200 nm) are the zoomed images of typical double-feature complexes; the blue arrows point to SSB, and the red arrows point to RecG protein. *E*, yields of SSB-RecG complexes on the fork DNA substrates. In the absence of SSB (orange bars), the binding yield of RecG on the DNA substrates are $10.6 \pm 1.9\%$ (on the F3 DNA substrate), $5.4 \pm 1.2\%$ (on the F6 DNA substrate), $7.4 \pm 1.5\%$ (on the F7 DNA substrate) and $7.3 \pm 1.5\%$ (on the F8 DNA substrate), respectively. With SSB premixed with DNA substrates (blue bars), the RecG binding yields increased to $27.4 \pm 5.3\%$, $11.6 \pm 4.1\%$, $24 \pm 3.6\%$, and $21.3 \pm 3\%$, respectively.

5.3.2 The restriction of RecG translocation by the mispairing on the parental duplex

We then investigated whether SSB can remodel RecG on all fork substrates and allow RecG to translocate over the duplex arms of the fork. To do this, we mapped the positions of SSB and RecG on all four DNA substrates, and the data are shown in Figure 5.3. SSB and RecG positions were measured from the end of the parental duplex (short arm). Since SSB binds specifically to the ssDNA of the fork DNA substrates, the position of SSB was set to 0 on the map. When RecG translocates on the parental strand, the position of RecG has a negative value (below SSB in the graph). When RecG translocates on the lagging strand, the position of RecG has a positive value (above SSB in the graph).

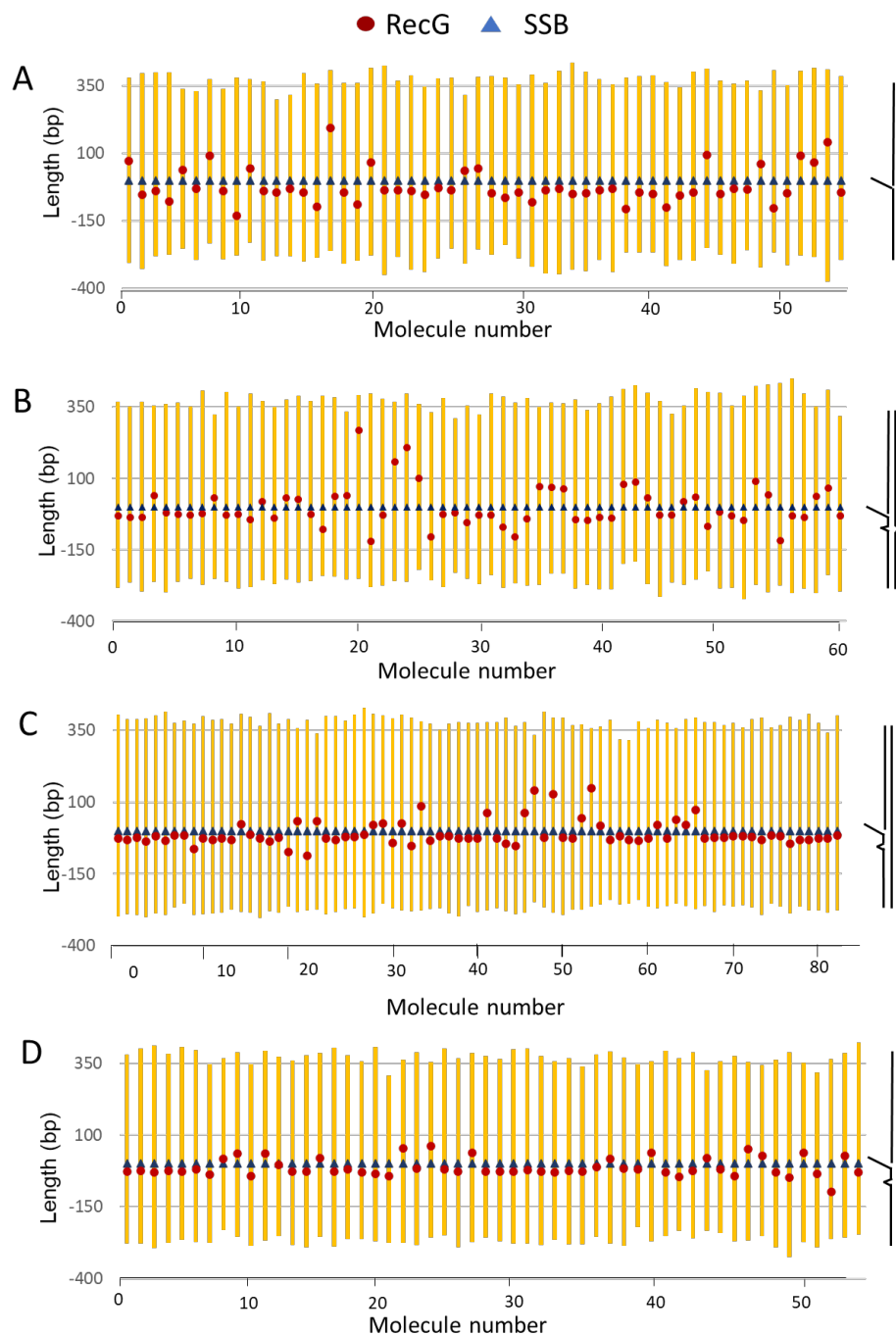


Figure 5.3. The mapping of protein positions on each DNA substrate. *A-D*, mapping of RecG positions relative to the SSB binding site (the fork position) on the F3, F6, F7, F8 DNA substrate, respectively. The map is constructed relative to the position of SSB position, indicated with triangles, while RecG is marked with circles.

In 75% of cases, RecG binds to the parental duplex of the F3 DNA substrate, with the translocation distance being 48 ± 13 bp (Figure 5.4 *A*). While on F6, F7 and F8 DNA substrates, RecG binds to the parental duplex in 60%, 75% and 74% of the cases, respectively. This is consistent with our previous finding; when the helicase is loaded onto the fork by SSB, RecG is visualized preferentially on the parental duplex arm of each substrate (71). When a DNA imperfection is positioned 10 bp from the fork (the F6 DNA substrate), the translocation preference that RecG is loaded onto the parental duplex decreased to 60%, compared to that of the 75% on the F3 DNA substrate. This is accompanied by an increase in inappropriate loading onto the lagging strand arm, up from 25 to 40%. Finally, the translocation distance for RecG on the parental duplex arm of this fork is 1.6-fold lower, which is at 30 ± 11 bp (Figure 5.4 *B*). In contrast, when either a C-C mismatch or a G-bulge was positioned 30 bp from the fork junction, the loading of RecG by SSB and the translocation preference are unaffected by the DNA imperfection. This follows as the duplex imperfection is positioned outside the footprint of RecG bound to a fork. However, the translocation distances for the F7 and F8 DNA substrates are measured to be 26 ± 11 bp and 26 ± 10 bp (Figures 5.4 *C and D*), respectively, which are 1.8-fold shorter than those on the F3 DNA substrate.

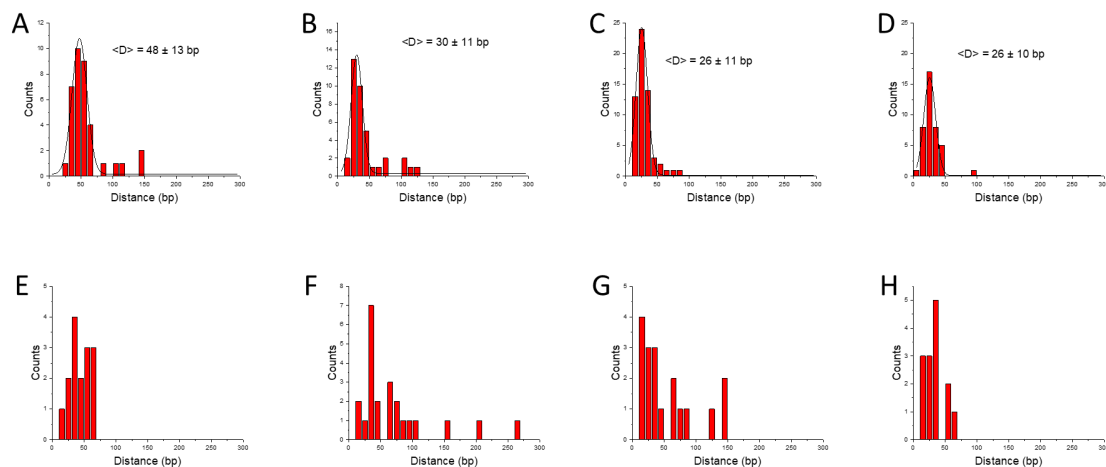


Figure 5.4. The analysis for the RecG-SSB distance. *A-D*, the histograms of the distance between the SSB and RecG on the parental duplex of the F3, F6, F7, and F8 DNA substrate, respectively. Histograms were approximated with Gaussian distribution, and the values corresponding to maxima on these distributions are shown in each histogram. *E-H*, the histograms of the distance between the SSB and RecG on the lagging strand arm of the F3, F6, F7, and F8 DNA substrate, respectively.

In contrast to the narrow distributions of translocation distances on parental duplex arms observed for each fork substrate, the translocation distance of RecG on the lagging strand arms varies over a wide range (Figures 5.4 *E-H*). There is no preferred translocation distance of RecG on the lagging strand. These data show that the C-C mismatch and G-bulge at 30 bp away from the fork limit the translocation of RecG on the parental arm to the region between the mismatch and the fork itself. Note that the translocation distance of RecG on the F6 DNA substrate is also 1.6-fold lower than that observed on undamaged DNA, where the duplex imperfection is 10 bp from the fork. It is conceivable that the C-C mismatch at this position perturbs the helicase domains from the proper association with the DNA duplex so that dissociation is favored.

5.4 Discussion

The RecG DNA helicase plays a crucial role in stalled replication fork rescue, where it regresses forks where replisomes were impeded. In the previous study, we found that the helicase is remodeled by SSB so that it slides on the parental duplex DNA ahead of the fork prior to the onset of fork regression, using thermal energy (71). We proposed that this sliding can test the integrity of the parental DNA ahead of the fork. Consequently, if duplex imperfections are encountered, this could result in RecG disengaging from the fork, thereby controlling the frequency of fork regression. To test this, we used AFM to visualize the effects of duplex lesions on the thermal sliding of RecG in the presence of SSB.

5.4.1 The effects of SSB on RecG binding to the fork DNA substrates

Our previous study suggested that fork-bound SSB enhances the loading of RecG onto forks. According to the yield calculated from each experiment, DNA mixed with RecG only or mixed with both SSB and RecG, the binding of RecG is increased when SSB is added to the DNA first (Figure 5.4). The binding is followed by thermal sliding predominantly on the parental duplex of

the fork DNA substrate, which is mediated by the helicase domains. In the absence of SSB, RecG is observed bound exclusively to the fork via its wedge domain. However, when SSB is bound to the fork, RecG is loaded onto the duplex regions with a preference for the parental duplex. This suggests that for a properly oriented SSB tetramer bound with the correct polarity, loading of RecG by one of the four available linker regions has dramatic effects on thermal sliding mediated by the helicase domains.

It has been proposed that, for SSB-RecG interaction to occur, the PXXP motifs in one intrinsically disordered linker of DNA-bound SSB bind to the oligonucleotide-oligosaccharide binding fold (OB-fold) in the wedge domain of RecG, which could result in the remodeling of RecG by SSB and the loading of RecG onto the DNA substrate (194,195,218). As the RecG OB-fold is required for fork regression and is occluded during SSB binding, the only way for RecG to bind to DNA is via its helicase domains (69,212,213). Once loaded, the helicase slides using thermal energy on the parental duplex of stalled replication forks, and this was proposed to be a duplex integrity-sensing mechanism (72). Once the helicase returns to the fork region, ATP hydrolysis-coupled regression ensues concomitant with the displacement of SSB (41,73). Here, RecG generates ≥ 35 pN of force to dislodge the first SSB tetramer, which communicates via the linker/OB-fold network of interactions to the remaining DNA-bound SSB tetramers, resulting in their cooperative dissociation (73).

5.4.2 The translocation of RecG limited by the lesions in the parental duplex

Based on our previous study, SSB remodels RecG and loads the helicase onto the parental duplex of the fork substrate (71,72). When the parental duplex has lesions (the F7 and F8 DNA substrates), the translocation distance is limited to the range of the distance between the fork and the lesion positions. On the F6 DNA substrate, the translocation distance is also lower than that on the F3

DNA substrate, suggesting that the CC-mismatch at this position perturbs the helicase domains from properly associating with the DNA duplex so that dissociation is favored.

The correctly loaded RecG bound to the parental duplex slides within a limited range while sensing the integrity of the parental duplex region. If the duplex integrity is intact, then in the presence of ATP, fork regression coupled to SSB displacement ensue. In other cases, the helicase can be improperly loaded onto the lagging strand arm of the fork (Figures 5.4 *E-H*), resulting in aimless sliding either towards or away from the fork (directionality cannot be ascertained from the AFM images). The net result is that this improperly loaded RecG will not regress the fork. Instead, it could translocate away from the fork, or if it does return to the fork, it could unwind the fork in the presence of ATP.

5.4.3 Conclusion

This chapter tested our hypothesis that if duplex imperfections could result in RecG disengaging from the fork and control the fork regression frequency. We found that a C-C mismatch or G-bulge placed 30 bp ahead of the fork has no effect on the efficiency of SSB loading but restricts RecG sliding to within the 30 bp from the fork. In contrast, on the DNA substrate with a C-C mismatch positioned 10 bp from the fork, the efficiency of RecG-loading by SSB decreases, but sliding is unrestricted for those loaded helicase molecules. These suggest that RecG can sense the integrity of the parental duplex ahead of the fork, and only when the duplex is intact will fork regression ensue.

Chapter 6. DNA FORK REGRESSION DYNAMICS INDUCED BY RECG HELICASE

6.1 Introduction

We have demonstrated that the interaction of fork-bound SSB leads to the remodeling of RecG during the loading process onto the DNA (71,72). We then characterized that the lesions in the parental duplex limit the translocation of RecG in Chapter 5. As the fork substrates used in the previous study were static, fork regression could not be visualized, and the interplay between SSB and RecG during this dynamic process could not be studied. Therefore, we constructed a mobile fork substrate to visualize the fork regression in the dynamic situation, which contains a 41 bp complementarity between the template leading strand and the template lagging strand downstream the fork region. It was anticipated that it would interconvert between two states, S1 and S2, driven by spontaneous branch migration.

As expected, in the absence of proteins, these two states were directly observed using AFM. Furthermore, in the presence of SSB, a bimodal distribution for the protein position corresponding to the two states of the fork was observed. In the absence of ATP, RecG bound preferentially to state S1, while in the presence of ATP, RecG regressed the fork and displaced SSB in the process. SSB maintains the fork structure (state S2) following regression by RecG. These findings show that the DNA helicase couples DNA unwinding to duplex rewinding and the displacement of SSB bound to the DNA, consistent with a previous single-molecule study (41).

6.2 Methods

6.2.1 Purify the proteins

All the proteins in this chapter were provided by Dr. Piero Bianco, University of Nebraska Medical Center. SSB and RecG proteins were purified as described in references (71,86,113).

6.2.2 Assemble the DNA substrates

The mobile fork DNA substrate (F12 DNA substrate) was assembled from two duplex-DNA segments and a core fork segment, similar to our previous methodology in Chapters 3, 4 and 5. The duplex-DNA segments were the same as used in Chapters 3 and 4. The core fork segment was assembled by annealing the ssDNA oligos (O30: 5'-TCATCTGCGTATTGGGCGCTCTTCCGCTTCCTATCT-3', O45: 5'-TCGTTGCGCTGCGGCGAGCGGGATCTAGTAGCTCTGCAGCACTGCATAATTATCAGCTCACTCATA-3', O46: 5'-GCTTATGAGTGAGCTGATAATTATGCAGTGCTGCAGAGCTACTAGATCGCCGCTCGCCGCAGCCGAACGACCTTGCGCAGCGAGTCAGTGAGATAGGAAGCGGAAGAGCGCCCAATACGCAGA-3', O47: 5'-CACTGACTCGCTGCGCAAGGTCGTTGCGCTGCGGCGAGCGGCGATCTAGTAGCTCTGCAGCCTTCATCTTTGGGTTCACTTTCTCCAC-3') in the same molar ratio. The duplex DNA segments and the core fork segment were ligated together in a molar ratio of 1:1:1 at 16°C overnight. The final products were purified with HPLC using a TSKgel DNA-STAT column.

6.2.3 Prepare the protein-DNA complexes

SSB/DNA complex was prepared by mixing the SSB tetramer with the DNA substrates (molar concentration: 20 nM) in a molar ratio of 2:1, and incubated in 10 µl of binding buffer [10 mM Tris-HCl (pH 7.5), 50 mM NaCl, 5 mM MgCl₂, 1 mM DTT] for 10 min at room temperature.

RecG/DNA complex was prepared by mixing RecG with the DNA substrate (molar concentration: 20 nM) in a molar ratio of 4:1, and incubated in 10 µl of binding buffer for 10 min at room temperature.

SSB/RecG/DNA complex was prepared by mixing SSB tetramer (concentration: 20 nM) and RecG in the molar ratio of 1:2 in 30 μ l of binding buffer on ice for 30 min. The DNA substrate was then mixed with the SSB-RecG complexes in a molar ratio of 1:2 and incubated in 10 μ l of binding buffer for 30 min at room temperature. The final molar ratio of DNA: SSB: RecG was 1:2:4.

The binding buffer for the experiments with ATP has the following composition: 10 mM Tris-HCl (pH 7.5), 50 mM NaCl, 5 mM MgCl₂, 1 mM DTT.

6.2.4 Acquire and analyze the AFM images

1-(3-aminopropyl) silatrane (APS) functionalized mica was prepared and used as the AFM substrate for all experiments. Ten microliters of the sample were deposited onto the APS functionalized mica for two minutes. The mica was rinsed with DDI H₂O and dried with a gentle argon flow. Images were acquired using tapping mode in the air on a MultiMode 8, Nanoscope V system (Bruker, Santa Barbara, CA) using TESPA probes (320 kHz nominal frequency and a 42 N/m spring constant) from the same vendor.

The dry sample AFM images were analyzed using the FemtoScan Online software package (Advanced Technologies Center, Moscow, Russia). The SSB positions were measured from the end of the short arm to the center of the protein. The DNA contour length was then obtained by continuously measuring to the other end of the DNA substrate. The yield of protein-DNA complexes was calculated from the ratio of the number of complexes to the total number of DNA molecules.

6.3 Results

6.3.1 The two dynamic states of the F12 fork substrate

The F12 DNA substrate used in this study has a 3'-end, 69-nt ssDNA region inserted between two heterologous duplex regions of different lengths (Figure 6.1), similar to the static fork DNA substrates that we designed for the previous chapters. As shown in the schematic of Figure 6.1, the duplex region on the left of the fork position corresponds to the parental duplex, while the duplex region on the right corresponds to the lagging strand arm of the fork substrate. The single-strand region on the right corresponds to the lagging strand arm of the fork substrate. The single-strand region at the fork position is the template leading strand. In contrast to the F3 DNA substrate in Chapters 3, 4 and 5, the central core of the F12 DNA substrate is homologous as there is a 41-nt region of ssDNA at the fork position, which is complementary to the template lagging strand. This design allows the fork to migrate between state S1 and state S2, as shown in Figure 6.1. At the state S1, the length of the parental duplex (the short duplex region) is 280 bp, and the length of the lagging strand arm is 423 bp, while the ssDNA region at the fork position is 69 nt. At the state S2, the length of the parental duplex is 321 bp, with the 41-nt complementary region of the ssDNA at the fork position annealing to the template lagging strand. Hence, the length of the lagging strand arm decreases to 382 bp. This design of the mobile fork is predicted to permit the study of the fork regression process.

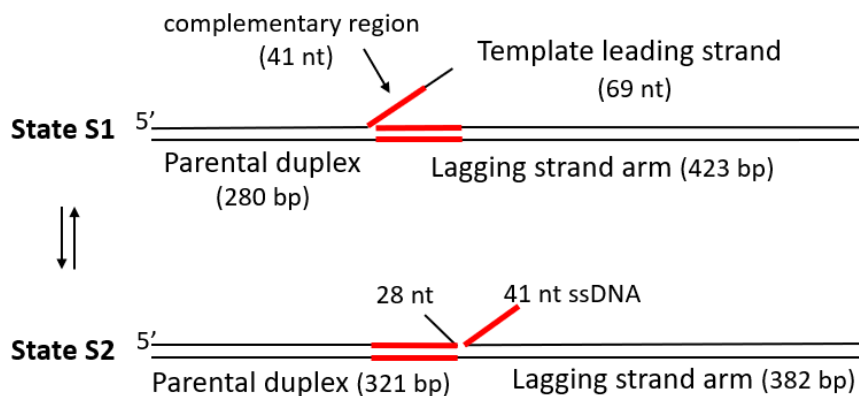
F12 DNA substrate

Figure 6.1. Dynamic fork design for this chapter. The F12 DNA substrate has a 3'-end 69-nt ssDNA region flanked by the duplex regions of different lengths. Within the ssDNA region, there is a 41-nt region (colored red) complementary to the template lagging strand. Consequently, the fork can equilibrate between two states (designated S1 and S2). Interconversion between S1 and S2 involves duplex DNA formation of the complementary sequences in the ssDNA and the template lagging strand. This results in a net increase of the parental duplex by 41 bp and a decrease in the lagging strand arm.

We imaged the F12 DNA substrate using AFM to determine if the fork can migrate between the two states. Figure 6.2 *A* shows a representative AFM image of the F12 DNA substrate. The zoomed-in images *i* and *ii* are the observation of sharp kinks at the fork position. The kink can be explained by the nick at the fork joint. The long ssDNA at the fork position can also contribute to the kink formation. This interpretation is supported by the kink position measurement of the distance from the end of the parental duplex to the kink position. The distribution of fork positions and the full length of DNA are shown in Figures 6.2 *B* and *C*. The histogram for the fork position can be approximated by a bimodal Gaussian distribution. The peak positions are 281 ± 9 bp and 308 ± 12 bp, which corresponds to the two states of the F12 DNA substrate. This suggests that the fork is dynamic between two states as designed. The DNA contour length measurement for the F12 DNA substrate is shown in Figure 6.2 *C*. The histogram is approximated with Gaussian distribution, and the peak is centered at 700 ± 27 bp, which corresponds to the designed length of the F12 DNA substrate (703 bp).

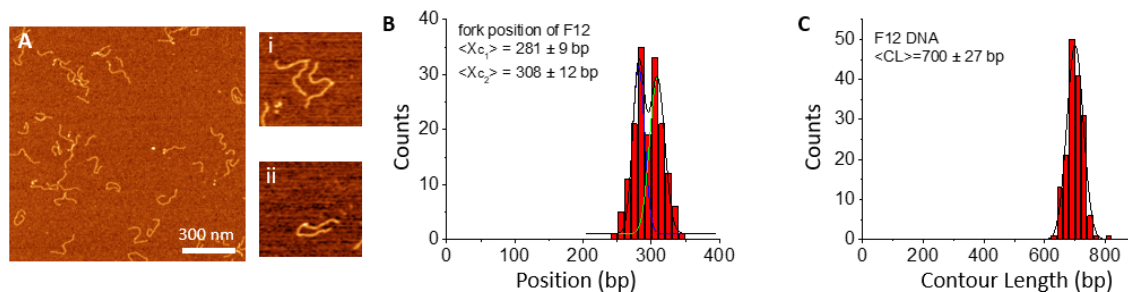


Figure 6.2. AFM analysis for the fork position of the F12 DNA substrate (the kinked DNA molecules). *A*, typical AFM images of the F12 DNA substrate. Zoomed-in images ($300 \text{ nm} \times 300 \text{ nm}$) of selected molecules with a clear appearance of the kink are shown to the right (*i and ii*). *B*, the distribution for fork positions measured from the end of the parental duplex. *C*, the contour length measurement for the F12 DNA substrate. The distributions were fitted by Gaussians, and the peak values X_c , defined by the maxima values $\pm \text{S.D.}$, are indicated on the histograms.

6.3.2 The assembly of a Holliday Junction on the F12 DNA substrate

To further confirm the mobility of the fork position between the two states, a 69-nt ssDNA, which is complementary to the 69-nt ssDNA of the F12 DNA substrate, was annealed to the fork DNA substrate. Given the self-complementarity at the fork position, the annealing can lead to the structures shown in Figure 6.3 *A*. If the fork is at state S1, the annealing will form a three-way junction on the F12 DNA substrate. However, a four-way Holliday Junction will be formed if the fork was at state S2.

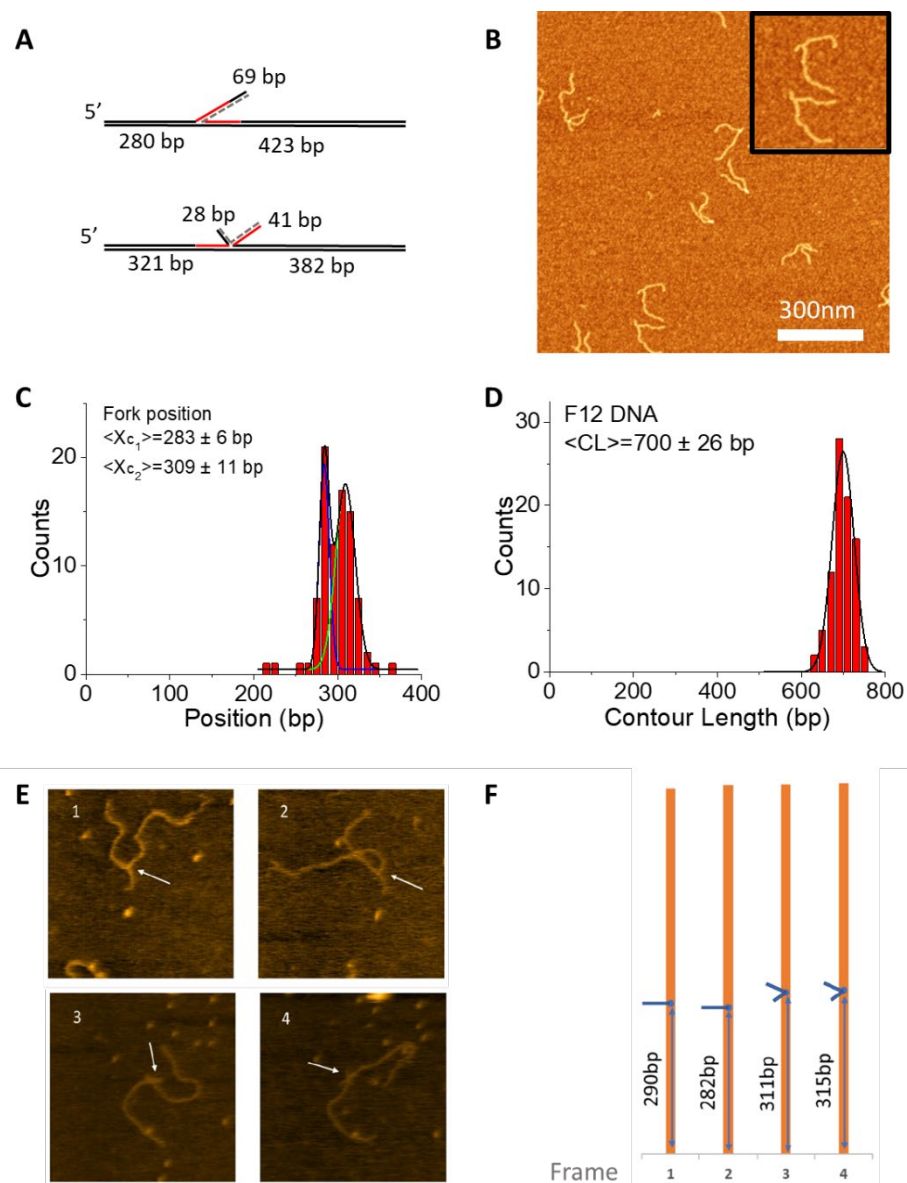


Figure 6.3. AFM analysis of the fork position on the F12 DNA substrate probed by annealing with a complimentary 69-nt ssDNA. *A*, the schematic of the annealed DNA substrate. The complimentary 69-nt ssDNA is colored in gray. *B*, representative AFM image of the annealed fork DNA substrate with a 69-nt ssDNA. Inset (size: 300nm \times 300nm) shows the enlarged images of the annealed F12 DNA substrate. *C*, the distribution for the dsDNA position at the fork measured from the end of the parental duplex. *D*, the contour length measurement for the annealed F12 DNA substrate. *E*, the selected frames of the F12 DNA substrate from the HS-AFM movie. Frames 1 and 2 show the 3-way junction, while frames 3 and 4 show the 4-way junction. The arrows indicate the fork position. *F*, the schematic of the substrate and changes of the fork position in the movie. The DNA molecule is aligned to the end of the parental duplex and colored in orange. The dsDNA at the fork position is colored in blue.

The representative AFM image of the annealed substrate is shown in Figure 6.3 *B*. We mapped the fork positions in Figure 6.3 *C*. The histogram was fitted with a bi-distribution Gaussian. The peaks are centered at 283 ± 6 bp and 309 ± 11 bp, which correspond to the two peaks measured for the kink position on the free DNA substrate (Figure 6.2 *B*). The distribution for the contour length measurement was fitted with a single-peak Gaussian with the peak centered at 700 ± 26 bp, as shown in Figure 6.3 *D*. The dynamic of Holliday junction was also visualized with HS-AFM and the selected frames are shown in Figure 6.3 *E*. The measurement of the ssDNA position from the selected frames in Figure 6.3 *F* suggests that the fork is dynamic during data acquisition.

It is also necessary to determine whether the binding of SSB would affect the equilibrium between the states S1 and S2. Therefore, we prepared samples of SSB-F12 DNA substrate complexes to mimic fork regression buffer conditions. The typical AFM image of SSB-F12 complexes in the absence of ATP is shown in Figure 6.4 *A*. The SSB protein appears as a bright globular feature. The SSB position on the F12 DNA substrate was measured from the end of the parental strand to the center of the protein and shown in Figure 6.4 *B*. The distribution can be fitted with a bi-distribution Gaussian with peaks centered at 285 ± 18 bp and 317 ± 13 bp, which correlate with the fork position on free DNA substrate (Figure 6.2 *B*). This result suggests that SSB binds to the fork at both states and does not affect the migration of the fork position.

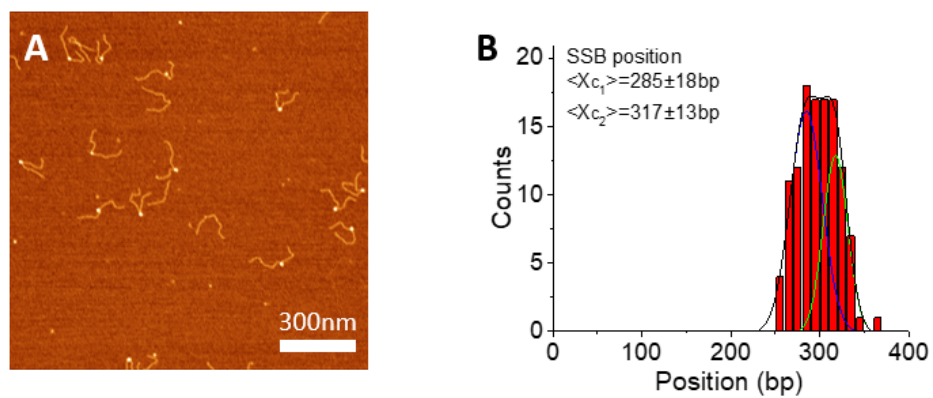


Figure 6.4. AFM results of SSB-F12 DNA substrates in the absence of ATP. *A*, a representative image of the SSB-F12 complex in the absence of ATP. *B*, the distribution of SSB position fitted by bi-distribution Gaussian.

6.3.3 The fork regression of the F12 DNA substrate by RecG

The experiments with both SSB and RecG bound to the F12 DNA substrate were performed. In these experiments, SSB and RecG were premixed and then added to the F12 DNA substrate. The experiments were performed in the absence and presence of ATP separately. Typical AFM images are shown in Figures 6.5 *A* and *C*. Most protein-DNA complexes have one protein bound onto the DNA substrate, while some DNA molecules have double-feature complexes with one feature larger than the other. The volume of the protein in the single-feature complex and the larger one in double particles in Figure 6.5 *A* was measured, and the average volume is $155.8 \pm 30 \text{ nm}^3$, which is close to the volume of SSB ($122.8 \pm 22 \text{ nm}^3$). This suggests that the protein in the single-feature complex or the larger protein in the double-feature complex is SSB, while the smaller protein in the double-feature complex corresponds to RecG. To check if RecG can change the binding of SSB to the F12 DNA substrate, we measured the position of SSB and the histograms are displayed in Figures 6.5 *B* and *D*. In the absence of ATP (Figure 6.5 *B*), the distribution of SSB is still broad and can be fitted by the bi-distribution Gaussian. The peak values are $278 \pm 12 \text{ bp}$ and $311 \pm 11 \text{ bp}$, consistent with the distribution observed for SSB only with DNA (Figure 6.4 *B*). In contrast, when the buffer contains ATP, the distribution of SSB positions is narrow and can be fitted with a single peak Gaussian (Figure 6.5 *D*). The average position is $313 \pm 14 \text{ bp}$, which corresponds to state S2 of the F12 DNA substrate. These results suggest that in the presence of ATP, RecG can rewind the complementary region on the fork DNA substrate, displacing SSB from the ssDNA.

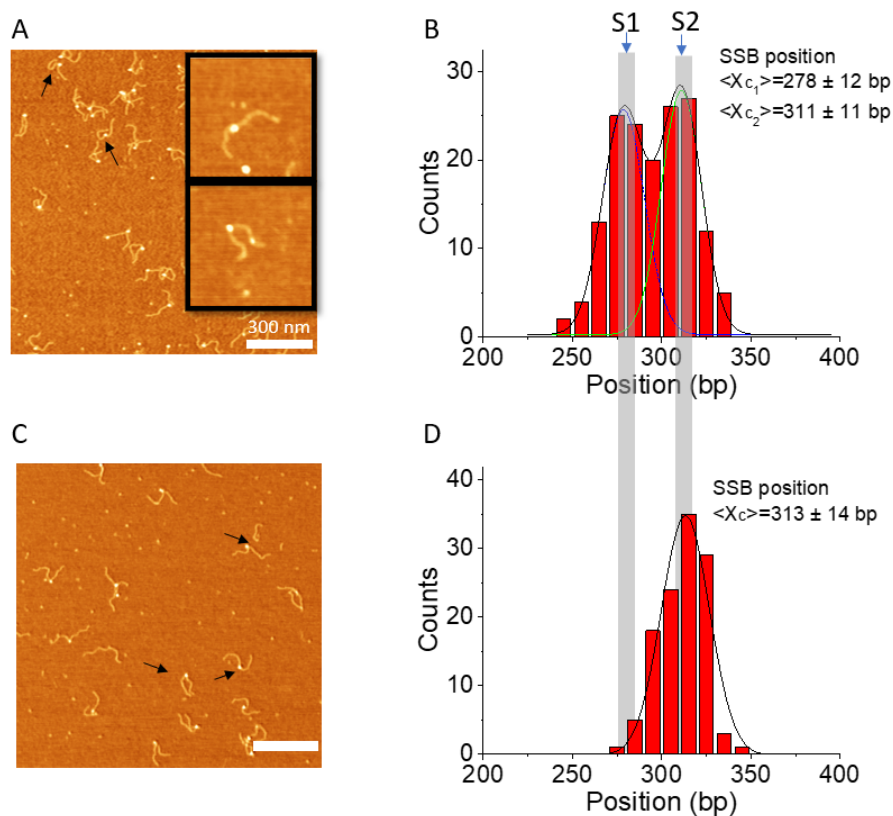


Figure 6.5. AFM analyses of the RecG-SSB-F12 complexes in the absence and presence of ATP. *A*, representative images of RecG-SSB-F12 complexes in the absence of ATP. Arrows point to the typical complexes. The two insets show the typical single and double feature complexes on the F12 DNA substrate (size: 300nm \times 300nm). *B*, the distribution of SSB in the complexes, in the absence of ATP. The histogram is fitted by the bi-distribution Gaussian. *C*, representative images of RecG-SSB-F12 complexes presence of ATP. *D*, the distribution of SSB in the complexes, in the presence of ATP. The histogram is fitted by a single peak Gaussian distribution.

To investigate if the shift of SSB position was caused by the fork regression, we performed experiments with the non-hydrolyzable ATP-analog, ATP γ S, instead of ATP. First, the position of SSB in the complexes was measured (Figure 6.6 *A*). The histogram was fitted with a two-peak Gaussian distribution, with the average positions at 289 ± 7 bp and 313 ± 8 bp, which are very close to positions of SSB in the absence of ATP (Figure 6.4 *B*). As a control, to determine whether ATP can change the binding activity of SSB to F12, the sample of SSB-F12 in the presence of ATP was prepared, and the positions of SSB were measured (Figure 6.6 *B*). The fitting of the histogram by Gaussian distribution shows two peaks centered at 290 ± 16 bp and 316 ± 7 bp. The distribution of the SSB position on the F12 DNA substrate is consistent in the absence and presence of ATP or ATP γ S, suggesting that ATP does not affect the position of SSB on F12.

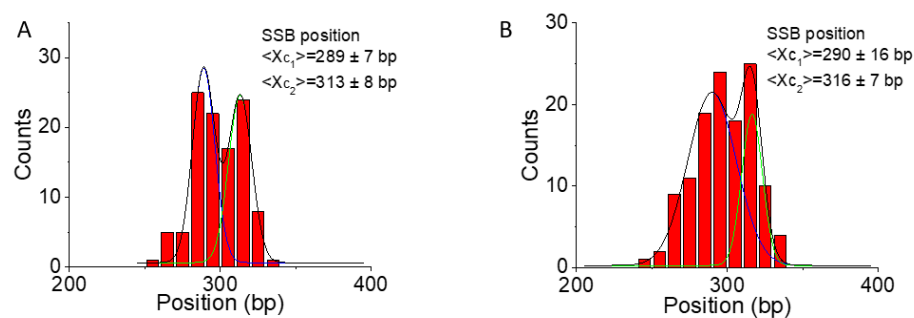


Figure 6.6. The SSB position in the complex. *A*, the distribution for SSB position in the RecG-SSB-DNA complexes in the presence of ATP γ S. The histogram is fitted by the bi-distribution Gaussian. *B*, the distribution for SSB position in the SSB-DNA complexes in the presence of ATP. The histogram is fitted by the bi-distribution Gaussian.

Similar experiments were done for RecG to determine whether fork position is altered in the presence of nucleoside triphosphate (Figure 6.7). In the absence of ATP, the RecG position on the F12 DNA substrate can be fitted with a single peak, and the position 281 ± 16 bp corresponds to state S1 of the fork substrate (Figure 6.7 *A*). In the presence of ATP, the histogram of the RecG position becomes broad and can be fitted with two Gaussian distributions (Figure 5.7 *B*). The peak positions are 280 ± 15 bp and 310 ± 16 bp. The maximum at 310 bp suggests that RecG binds to the fork and regresses it from state S1 to state S2. Hence, in the presence of ATP, RecG catalyzes the regression of the fork from state S1 to S2. However, due to the design of the fork, a fraction of the regressed forks revert to S1 once RecG disengages from the DNA, which explains the broad distribution of RecG position in Figure 6.7 *B*.

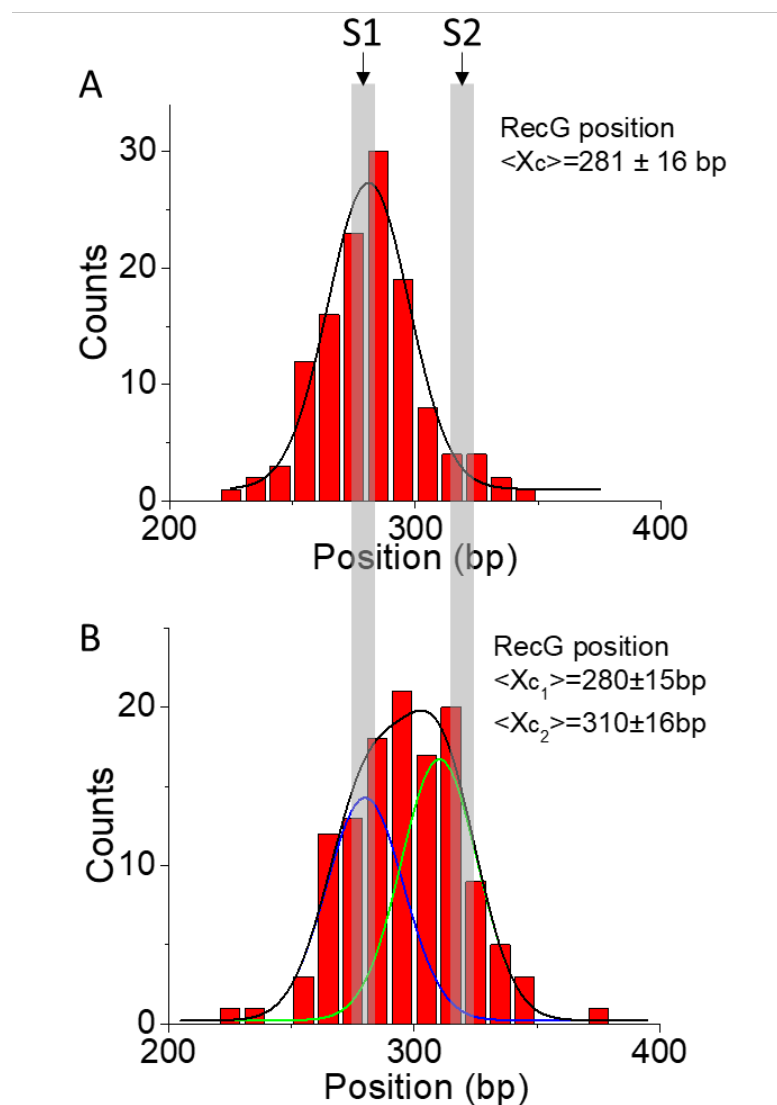


Figure 6.7. The RecG position in the RecG-DNA complex. *A*, the distribution for RecG position in the RecG-DNA complexes in the absence of ATP. The histogram is fitted by the Gaussian distribution. *B*, the distribution for RecG position in the RecG-DNA complexes in the presence of ATP. The histogram is fitted by the bi-distribution Gaussian.

6.4 Discussion

As a static fork was used in the previous study, it was impossible to study the fork regression catalyzed RecG. Therefore, a dynamic fork design was required, designated F12 DNA substrate. It is shown that the designed fork substrate equilibrates between two states: S1 (a stalled replication fork) and S2 (a regressed fork). Additionally, SSB binds to each state without a clear preference. The primary finding is that RecG drives fork regression and displaces SSB from DNA in the process, consistent with previous single-molecule studies with magnetic tweezers.

6.4.1 The fork regression by RecG in the presence of ATP

The binding of RecG to the F12 DNA substrate remains transient so that the complex yield remains as low as 6.3% and is unaffected by the presence of ATP. Furthermore, the presence of ATP does not change the partition of the F12 DNA between states S1 and S2 (Figure 6.7). This follows because of the transition from state S1 to S2 due to the fork regression by RecG. However, a fraction of the regressed fork will revert back to S1, thereby reestablishing the equilibrium. In contrast, when SSB is present in the regression reaction, it binds to the fork at state S2, trapping the fork and producing an increase in the ratio of S2:S1 (Figure 6.5). The RecG-dependent shift in this ratio was only observed in the presence of ATP since the equilibrium between S1 and S2 was unaltered in the absence of ATP or the presence of the non-hydrolyzable analog ATP γ S. The control experiments demonstrate that SSB alone does not alter the S1:S2 ratio, and it can maintain the status of the fork state after binding to F12 DNA substrate. Therefore, the only way this ratio could be altered is if RecG bound to the SSB-DNA complex and then hydrolyzed ATP to drive fork regression, concomitant with the SSB displacement.

Similar to previous studies with the static F3 fork DNA substrate, we observed the SSB-mediated remodeling of RecG based on the direct visualization of double-feature complexes on the F12 DNA substrate. In these complexes, the SSB position coincides with the location of the fork,

whereas RecG binds to DNA far from the fork position. Thus, regardless of whether the fork is static or dynamic, SSB-loading of RecG concomitant with helicase remodeling is observed. This suggests that remodeling is intrinsic to the SSB-mediated loading process. Although the remodeling of RecG by SSB was observed on the dynamic fork, the yield of the double-feature complexes (~5% on F12 DNA substrate) was lower than that on the static fork F3 DNA substrate (~10%). This finding suggests that once loaded onto the parental duplex, RecG slides back to the fork, the wedge domain engages the fork, resulting in regression and displacement of SSB and this dynamics is coupled to ATP hydrolysis. For this to occur, SSB must slide some short distance on the ssDNA tail and away from the fork to permit wedge domain access. SSB sliding has been demonstrated ²³. In contrast, RecG sliding before the onset of regression can only occur when the duplex DNA is undamaged. Ultimately this ensures that the regression does not occur, and other repair enzymes must process the DNA first.

6.4.2 Conclusion

In this chapter, we characterized the interaction between RecG and SSB on the mobile fork substrate. The mobile fork substrate migrates simultaneously between two states; the stalled fork (state S1) and the regressed fork (state S2). The presence of SSB does not alter the states of the fork substrate. In the absence of ATP, RecG binds preferentially to state S1. While in the presence of ATP, RecG regressed the fork and displaced SSB in the process.

Chapter 7. ASSEMBLY OF NUCLEOSOME ARRAY INTO HIGHER-ORDER STRUCTURES

7.1 Introduction

DNA in eukaryotic cells is packaged into chromatin through extensive association with histone proteins (219-221). Nucleosome is the fundamental unit of chromatin, which regulates the readout and expression of eukaryotic genome (222-224). It is a DNA-protein complex with approximately 147 base pairs of DNA wrapped around a protein complex known as histone octamer (91,225,226). Canonical histone octamers consist of two copies of the four core histone proteins, H2A, H2B, H3, and H4 (90). The positively charged histone octamers bind strongly to the negatively charged DNA. The X-ray crystallography revealed the atomic structure of the nucleosome and explained how DNA is wrapped around histone octamers in a superhelix of approximately one and three-quarters of turns (227). Meanwhile, the spatial organization of nucleosomes in chromatin continues to be the source of debate. Initially, it was proposed that nucleosomes condense into a 30-nm-diameter chromatin fiber based on electron microscopy (EM) or X-ray scattering analyses of chromatin extracted from various organisms (228-231). Most recently, however, a combination of EM topography with a developed labeling method (ChomEMT) does not support the assembly of ordered 30-nm fibrils (232). Instead, they showed the assembly of 10-nm fibers in the cell that are not uniform; instead, they are heterogeneous and vary in diameter between 5 and 24 nm. Potential reasons are discussed in the recent review article (233), in which the major role is given to electrostatics, as ionic strength for experiments *in vitro* and inside cells are very different. The authors also suggest that the absence of the 30-nm fiber formation can be due to nucleosome loss or irregular nucleosome spacing in native chromatin. It has then been proposed that nucleosome

fibers exist in a highly disordered, interdigitated state (109,234,235). What is the reason for such irregular spacing of nucleosomes? We have recently shown that the internucleosomal distance within dimers of nucleosomes varies depending on DNA sequences (111). No such effect is detected if repeats of such a highly sequence-specific DNA motif as Widom 601 are used in similar experiments (236). Note that most structural studies of chromatin, including papers cited above, used repeats of the 601 motif.

Our central hypothesis is that the DNA sequence is a factor that is critically involved in the interactions between nucleosomes and their assembly into higher-order structures. To test this hypothesis, we designed a DNA substrate with the specific positioning sequence, the 601 motif, and the non-specific sequence from the plasmid DNA that does not have such strong binding affinity as the 601 motif. By incorporating sequences with varying binding affinities into one DNA substrate, we can investigate the internucleosomal interactions and assembly pattern on this substrate and compare that with the previous studies on the repeated 601 motifs. Here, we conducted experimental nanoscale structural studies using single-molecule AFM, which can characterize the dynamic states of biological systems (173,237-239). Here, we present the analyses for the oligo-nucleosomes in AFM topographic images that provide the organizational properties and internucleosomal interactions of the nucleosome array.

7.2 Methods

7.2.1 Prepare the DNA substrate

The DNA substrate used in nucleosome assembly contains the 147 bp 601 Widom sequence flanked by plasmid DNA, 113 bp, and 738 bp in length (shown in Figure 7.1). It is generated from PCR using a plasmid vector pUC57 with the forward primer (5'-GATGTGCTGCAAGGCGATTAAG-3') and the reverse primer (5'-GGGTTTCGCCACCTCTGAC-3'). The DNA substrate was

concentrated from the PCR product and purified using gel electrophoresis. DNA concentration was then determined using NanoDrop Spectrophotometer (ND-1000, Thermo Fischer) before being used for nucleosome assembly.

7.2.2 Assemble the nucleosome

Nucleosomes were assembled using a gradient dilution method optimized from our previous research (111,240-242). Recombinant human histone octamers were purchased from The Histone Source (Fort Collins, CO) for use in assembly. Before assembly, histones were dialyzed against the initial dialysis buffer [10 mM Tris (pH 7.5), 2 M NaCl, 1 mM EDTA, 2 mM DTT] at 4°C for 1 hour. DNA (25 pmol) was then mixed with the histone octamer at a molar ratio of 1:5. The total volume of the mixture should be adjusted to 10 μ l with 5 M NaCl and DDI H₂O so that the start concentration in the reaction is 2 M NaCl. The mixture was diluted with dilution buffer [10 mM Tris (pH 7.5)] using a syringe pump (0.07 μ l/min for 1000 min) to decrease the salt concentration to 0.25 M NaCl, allowing the histone to bind the DNA and form the nucleosome core particle. The nucleosomes were then dialyzed for 1 hour against a fresh low salt buffer before being diluted to 300 nM and stored at 4°C. The final concentration of the nucleosome n was adjusted to 2 nM right before deposition, using imaging buffer [10 mM HEPES (pH 7.5), 4 mM MgCl₂].

7.2.3 AFM imaging and data analysis

Sample preparation for AFM imaging was performed as described in previous chapters. The nucleosome sample was deposited onto the APS-functionalized mica and incubated for 2 minutes at room temperature. After that, the sample was rinsed with DDI H₂O and dried with argon flow. The samples were stored in vacuum before being imaged.

Images were acquired using tapping mode in the air on a MultiMode 8, Nanoscope V system (Bruker, Santa Barbara, CA) using TESPA probes (320 kHz nominal frequency and a 42

N/m spring constant) from the same vendor. The dry sample AFM images were analyzed using the FemtoScan Online software package (Advanced Technologies Center, Moscow, Russia).

DNA contour length analysis was performed by measuring from one end of free DNA to the other. The mean measured value of free DNA on an image was divided by the known length of the given substrate, yielding a conversion unit. Flank measurements for the nucleosomes were obtained by measuring from the DNA end to the center of the nucleosome for both arms. 5nm was subtracted from each measured flank length/internucleosomal distance to account for the length contributed by the histone core. The flank length and the internucleosomal distance measurements were divided by the calculated conversion unit to convert measurements in nm to bp. The histograms were approximated with Gaussian distribution, and the mean values and errors (S.D. and SEM) were calculated using Origin software (OriginLab Corporation, Northampton, MA, USA).

7.3 Results and discussion

The DNA substrate used in this chapter contains a 147 bp strong positioning 601 Widom sequence in the non-specific sequence of DNA (Figure 7.1 *A*). The 601 sequence has been widely used in the studies of the nucleosome array for its high affinity for histone octamers (243). Incorporating the non-specific sequence in the DNA substrate allows us to characterize the internucleosomal interactions on the non-specific sequence, which provides insights into chromatin folding.

7.3.1 The assembly of oligo-nucleosome on the DNA substrate

We prepared the nucleosome sample with DNA and histone octamers mixed at the ratio of 1:5, and the AFM image of the assembled oligo-nucleosome is shown in Figure 7.1 *B*. The bright circular features are the nucleosome cores, and the strands are the unbound DNA in the nucleosomes. The compact arrangement of the nucleosomes is shown in the image, with the arrows pointing to the

compact structures. The randomness in these structures contrasts with the solenoid model, where the nucleosome arrangement is well-organized (244,245). This could be due to the incorporation of the non-specific sequence in the designed substrate; the fewer artificial sequences included, the more freedom for nucleosomes to self-assemble into compact structures.

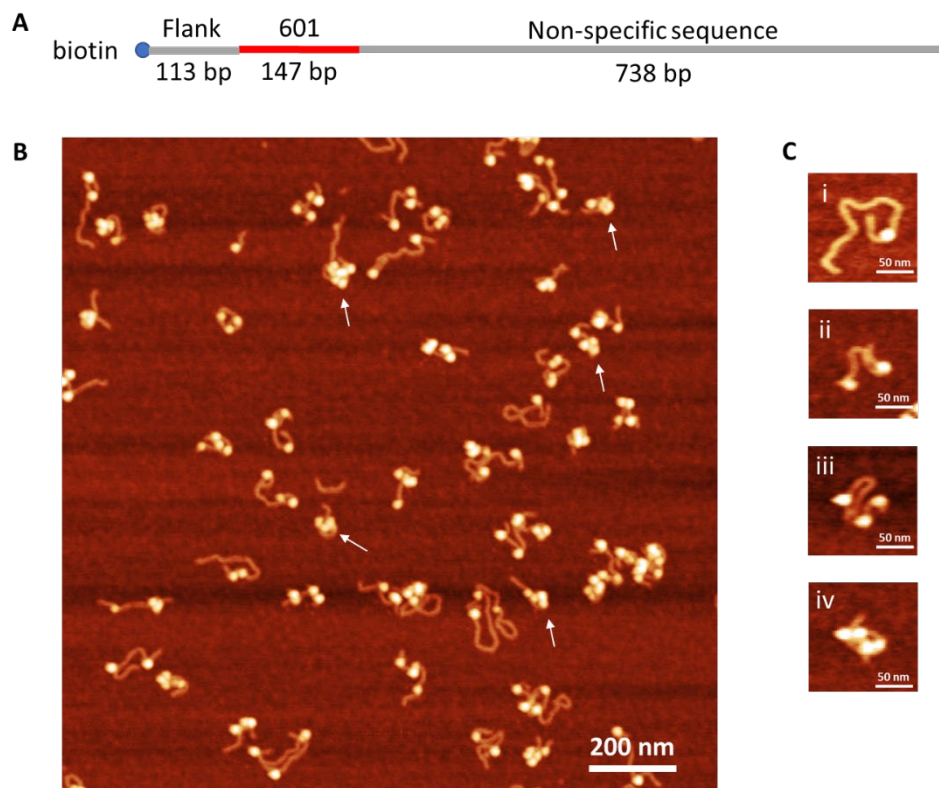


Figure 7.1. The AFM image of the nucleosome array. *A*, the design of the DNA substrate. It is a 998 bp DNA with a 601 sequence placed between the 113 bp flank and the 738 bp non-specific sequence. The length of the non-specific sequence allows three potential histone octamers to bind (147 bp for each nucleosome + 60 bp linker). *B*, the AFM image of the assembled nucleosome on the DNA substrate. The arrows point to the compact structures observed in the AFM image. *C*, gallery of the assembled oligo-nucleosome. *i*, the mononucleosome; *ii*, the dinucleosome; *iii*, the trinucleosome; *iv*, the tetranucleosome.

When the DNA substrate and histone octamers were mixed at the ratio of 1:5, the tetranucleosome, trinucleosome, dinucleosome, and mononucleosome were observed. The representative snapshots of each type of oligo-nucleosome are shown in Figure 7.1 *C*. Interestingly, there are subpopulations observed in the oligo-nucleosome; the well-separated nucleosomes and the compacted nucleosomes. The representative images of each subpopulation in the oligo-nucleosome are shown in Figure 7.2. We first calculated the yield and the sub-population of each oligo-nucleosome (table 7.1). The yields of trinucleosomes and tetranucleosomes are very close to each other. Furthermore, the well-separated nucleosomes are the minor sub-population in both trinucleosomes and tetranucleosomes, indicating that the compact structures are more favored than the well-separated structures with uniform spacing in higher-order structures.

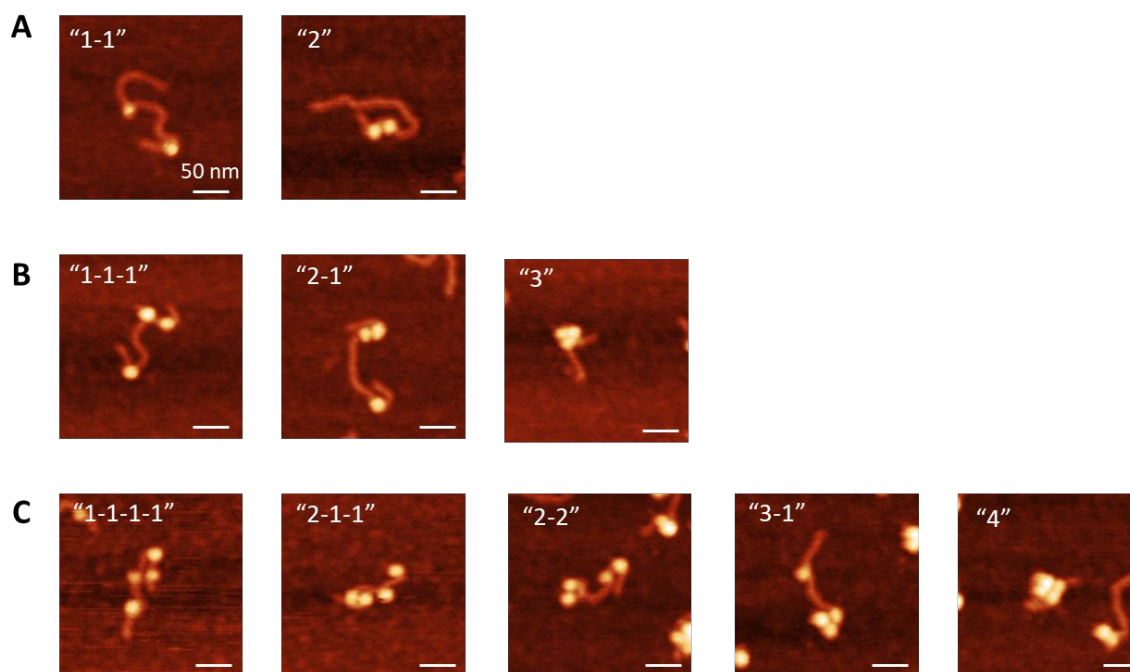


Figure 7.2. Gallery of the subpopulations in the oligo-nucleosome. The scale bar size is 50 nm, and the Z-scale is 4 nm. *A*, the subpopulations in dinucleosomes. *B*, the subpopulations in trinucleosomes. *C*, the subpopulations in tetranucleosomes.

Table 7.1. The yield of each oligo-nucleosome. In the subpopulation, “1-1”, “1-1-1,” and “1-1-1-1” are the well-separated nucleosome. The “2”, “3,” and “4” are the compacted nucleosome, depending on the number of the nucleosome in the complex.

	Yield (N=493)	Subpopulation	
Free DNA	2.8%	NA	
Mononucleosome	16.6%	NA	
Dinucleosome	20.3%	1-1	83.6%
		2	16.4%
Trinucleosome	30.9%	1-1-1	29.8%
		2-1	51.2%
		3	19.0%
Tetranucleosome	29.4%	1-1-1-1	10.7%
		2-1-1	17.5%
		2-2	14.6%
		3-1	37.9%
		4	19.4%

The compaction and various spacing of oligonucleosomes contradict most of the nucleosome array studies where the unwrapped linker DNA stays around 10-50 bp in length (246-248). In those studies, the DNA substrates typically consist of 601 sequences spaced by the linker DNA. This high thermodynamic and structural stability of 601 DNA wrapping has the practical advantage that nucleosomes are readily formed and behave homogeneously, so the 601 sequence has become near-ubiquitous as an experimental substrate. Nevertheless, this homogeneity brings disadvantages for studying nucleosome dynamics and their biological relevance in the eukaryotic genome. However, in our design, the DNA sequence is non-specific except for one 601 sequence. The 738 bp of the non-specific is adequate for three additional histone octamers to bind, considering that the mean wrapping efficiency of the nucleosome is ~147 bp and the linker length is ~60 bp. One view is that nucleosome remodeling complexes might regulate the nucleosome positions and override the sequence preference (249). Another argument is that nucleosome remodeling complexes may allow nucleosomes to search and bind the high-affinity sequences regulated by their intrinsic preferences, which results in a thermodynamic equilibrium between the nucleosomes and the site-specific DNA binding proteins (250). It has been proved that eukaryotic genomes use a nucleosome positioning code and link the resulting nucleosome positions to specific chromosome functions (251). Our observation of the various linker lengths between the nucleosomes formed on the designed DNA substrate suggests that the DNA sequence might also regulate the positioning of nucleosomes and their arrangement into chromatin.

We then turned our focus to the internucleosomal distance because we found that, among each oligo-nucleosome, the majority of the subpopulation are the ones that have a well-separated nucleosome. For dinucleosomes, the “1-1” subpopulation has a higher yield (83.6%) compared to the compacted dinucleosome (the “2” subpopulation, 16.4%). It is also the “2-1” subpopulation for trinucleosomes that has a relatively high yield (51.2%) compared to the other subpopulation. Similarly, the “3-1” subpopulation has a yield of 37.9% among tetranucleosomes. Why is the well-

separated nucleosome away from the compacted ones? Is it wrapped by the 601 sequence or the non-specific sequence? We measured the arm lengths for the “3-1” subpopulation in the trinucleosomes to assign the 601-motif nucleosome. The arm length on the well-separated nucleosome is referred to as arm length 1, while the arm length on the compacted nucleosome is arm length 2, shown in Figure 7.3 A. 10 nm was subtracted from each measured distance to account for the length contributed by the histone core in each nucleosome. From the histograms of the arm length measurements, both arm lengths 1 and 2 can be fitted with Gaussian distribution, with centered peaks at 100 ± 26.8 bp for arm length 1 and 108 ± 18.3 bp for arm length 2. Both are very close to the designed flank length (113 bp), but the distribution of arm length 2 is wider than that of arm length 1. In this case, we need to label the end of the flank to differentiate the 601 sequence from the non-specific sequence, as we did in our previous study. Since the observed size of the streptavidin-biotin complex is similar to the nucleosomes, we used rhizavidin for our oligo-nucleosome experiment, which exhibits a high affinity towards biotin with a dimeric quaternary structure (252,253). The AFM images of the rhizavidin-labeled samples have been acquired, but we are still collecting the data.

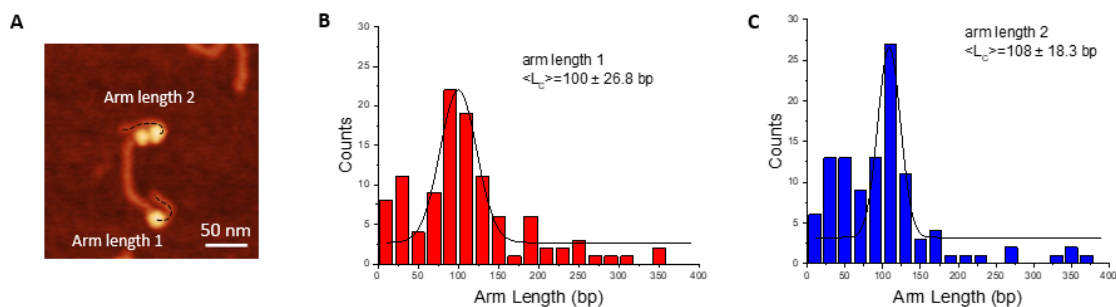


Figure 7.3. AFM analyses for the arm length of the “2-1” subpopulation in the trinucleosome. *A*, the schematic of the arm length measurements. Arm length 1 is the length measured from the center of the well-separated nucleosome to the nearest end of the arm. Arm length 2 is the distance measured from the end of the other arm, on the compacted nucleosome side, to the center of the nearest nucleosome. *B*, the histogram of the arm length 1 fitted by Gaussian distribution. *C*, the histogram of the arm length 2 fitted by Gaussian distribution. Bin size in each histogram is 20 bp.

7.3.2 The internucleosomal distance of the trinucleosome

Another question arose during data acquisition and analyses; what is the range of internucleosomal interaction? To answer that, we measured the distance between the nucleosomes in the “2-1” subpopulation of the trinucleosomes. Figure 7.4 *A* shows that the distance from the center of the well-separated nucleosome to the one closest to it in the compacted nucleosomes is terminated distance 1, while the distance between the two compacted nucleosomes is terminated distance 2. 10 nm was subtracted from each measured distance to account for the length contributed by the histone core in each nucleosome. The results shown in Figure 7.4 *B* suggest that the distance between the well-separated nucleosome from the compacted nucleosomes starts from 90 bp. In contrast, the distance of the compacted nucleosomes is in the range of 0-70 bp. This indicates that distances within 70 bp are more favorable for the internucleosomal interactions to compact the nucleosomes into proximity. However, we still need to assign the nucleosome wrapped by the 601 sequence from the one wrapped by the non-specific sequence before driving any conclusion. In addition to the rhizavidin-labeled samples, we also designed a DNA substrate containing the non-specific sequence only. The results from these experiments will further characterize the effects of the 601 sequence in the internucleosomal interaction and the nucleosome array.

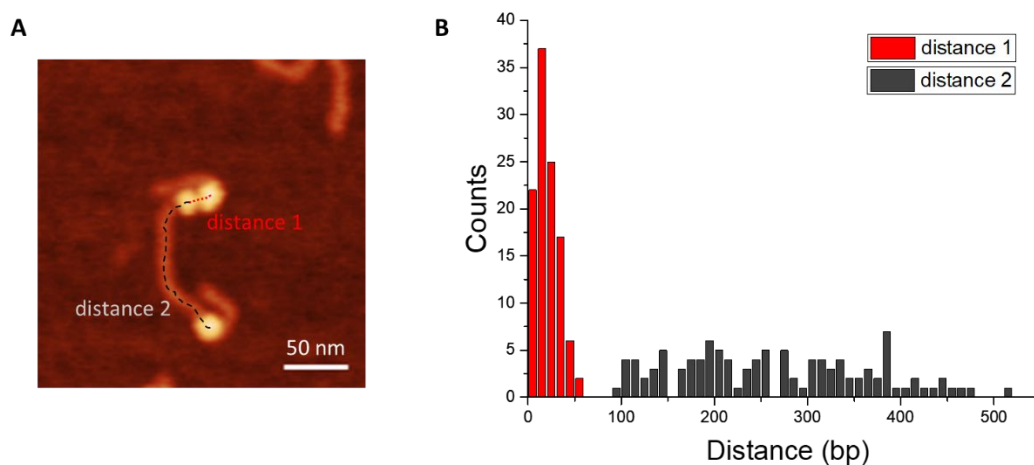


Figure 7.4. The measurement for the distance between the nucleosomes in the “2-1” subpopulation of the trinucleosome. *A*, the schematic of the distance measurements. Distance 1 is measured from the center of the well-separated nucleosome to the nearest center of the other nucleosome. Distance 2 is the distance between the centers of compacted nucleosomes. *B*, the histogram of distance 1 fitted by Gaussian distribution. *C*, the histogram of distance 2 fitted by Gaussian distribution. Bin size in each histogram is 10 bp.

7.3.3 Discussion

To test our central hypothesis that the DNA sequence is a critical factor in the interactions between nucleosomes and their assembly into higher-order structures, we designed a DNA substrate with both specific positioning DNA sequence (the Widom 601 sequence) and non-specific DNA sequence. The size of the designed DNA substrate is enough for four nucleosome core proteins to bind, allowing us to investigate the nucleosome arrangement on the basis of our dinucleosome study (111). On the DNA substrate designed for dinucleosomes, which has one 601 sequence and a non-specific sequence of the same size, we found that nucleosomes wrapped by the non-specific sequence indicate a positioning preference relative to the 601-wrapped nucleosome. Furthermore, the analyses for the internucleosomal distance suggest that the interactions between the nucleosomes are independent of the nucleosomal wrapping efficiency, an important geometrical characteristic that defines the orientation of one nucleosome relative to another.

In this chapter, we found that nucleosomes tend to be positioned close to each other on the DNA substrate designed for tetranucleosomes (Figure 7.1, Table 7.1). The analysis for the internucleosomal distance of the trinucleosome (Figure 7.4) shows a cut-off value for the distance between adjacent nucleosomes. So we suggest that the internucleosomal interaction could compact the nucleosomes within a certain range (~ 80 bp) into proximity. The preliminary analyses indicate that the nucleosome positioning is rather random on the non-specific DNA sequence, and the internucleosomal interactions might regulate nucleosome spacing and compaction. However, we need more analyses to elucidate the effects of 601-motif and internucleosomal interactions in the nucleosome array.

Chapter 8. SUMMARY

The research described above has several significant contributions for understanding the molecular mechanism of the stalled replication fork rescue and the nucleosome array assembly.

8.1 The PriA helicase at the stalled replication fork

We first demonstrated that SSB loads PriA onto the duplex arms of the fork DNA substrates, suggesting that the interaction of PriA with SSB changes the helicase conformation so that PriA becomes capable of binding to duplex DNA, which is termed as remodeling. As a result, the remodeled PriA can bind to the DNA duplex with spontaneous translocation over DNA duplexes, which may stimulate the association of PriA at the stalled replication fork in an ATP-independent way and facilitate the restart process once the ATP is available for PriA helicase activity. Furthermore, the interaction between SSB and PriA increases the binding of PriA to fork DNA substrates. This suggests that the SSB stimulation effect, as it is known on PriA helicase activity, also plays a role in the binding of PriA onto DNA substrates. In addition, the protein-protein interactions of SSB with other partner proteins, reported for RecQ (200,201,210) and RecOR (202,203), suggest that the remodeling of components of the DNA replication machinery is a new property of SSB.

The AFM approach allowed us to characterize the ATP-dependent dynamics of PriA on the fork DNA substrates (Chapter 4). In the presence of ATP, PriA was observed to bind mainly to the fork position, but it can also translocate over distances as distant as several hundred base pairs. When PriA was observed at the fork position, the unwinding of a small region of the duplex DNA could happen based on Keck's model that PriA unwinds the duplex DNA by "pulling" the DNA across the helicase domain (192). However, the non-fork-located complexes suggest that PriA can

translocate over large distances as well. We also discovered that PriA changed its translocation direction several times, revealing a previously undiscovered property of PriA- the capability to alter the direction of the translocation. We suggest that the changes in the moving direction are due to the strand-switching property of PriA, which can redirect PriA back to the fork position of a less-favored substrate, such as a substrate without an ssDNA gap on the lagging strand. After that, PriA can unwind the lagging strand to recruit DnaB onto the stalled replication fork.

8.2 The RecG helicase at the stalled replication fork

We have demonstrated that the interaction of fork-bound SSB leads to remodeling of RecG during the loading process onto a static fork DNA (72,254). As a result, RecG can translocate spontaneously ahead of the replication fork over distances as large as 200 bp. We hypothesized that duplex imperfections function as a signal to RecG that the fork structure is compromised so that instead of regressing the fork, RecG dissociates. In Chapter 5, we assembled the fork DNA substrates with duplex imperfections in the parental duplex to test our hypothesis. The results show that damages in the immediate vicinity of the fork position decrease the binding of RecG to the fork, resulting in a failure to regress the stalled fork. We then characterized the fork regression dynamics by RecG on a mobile fork substrate in Chapter 6. The AFM analysis suggests that SSB binds to the fork DNA substrate at both states and does not affect the migration of the fork position. On the contrary, the results show that RecG binds preferentially to state S1 in the absence of ATP, while in the presence of ATP, RecG regresses the fork. The fork regression is coupled with SSB displacement, and after that, SSB maintains the regressed fork structure.

8.3 The nucleosome array

In Chapter 7, we investigated our central hypothesis that the DNA sequence is essential for the interactions between nucleosomes and their assembly pattern into higher-order structures, building

on the previous results obtained for internucleosomal interactions on dinucleosomes (111). The AFM images show random arrangements in the higher-order nucleosome structures, which differ from the well-organized structures with uniform spacing in the solenoid models (245). The preliminary data show that nucleosomes are often positioned close to each other, suggesting that the non-specific sequence allows nucleosomes to communicate actively and form compacted structures. Furthermore, the internucleosomal distance of the trinucleosome shows a cut-off value for the adjacent nucleosomes. This analysis indicates that the internucleosomal interaction between nucleosomes wrapped by the non-specific DNA sequence within a certain range (~ 80 bp) could compact the nucleosomes into higher-ordered structures.

8.4 Prospects

Replication stress is a complex phenomenon that has severe implications for genome stability, cell survival, and human disease. However, the lack of knowledge on the replication fork rescue process impedes progress in the treatment of these diseases. As shown in Chapters 3-6, the characterization of the stalled replication fork processed by PriA helicase, RecG helicase, and SSB provides a fundamental step toward better understanding the eukaryotic replication fork rescue. Our long-term goals are to elucidate each step in the replication fork rescue process, explain properties of the involved proteins, and identify potential anti-rescue risks. The ultimate goal is to translate this knowledge to the eukaryotic replication rescue machinery and provide novel insights into potential diseases caused by defective responses to replication stress.

In the current project, we presented the ATP-independent PriA binding preference to the DNA substrates, the remodeling of PriA by SSB, the protein-protein interactions between PriA and SSB in the absence of ATP, and the ATP-dependent translocation of PriA. So the characterization of the PriA-mediated rescue process together with SSB in the presence of ATP will improve biological relevance since it has been discussed that SSB stimulates the ATP-dependent helicase

activity of PriA (87,197). Additionally, experiments with other enzymes, such as RecG, RecBCD, and RuvABC, added before PriA in the presence of SSB and ATP are essential towards a comprehensive understanding of the replication rescue.

Nucleosome serves three primary roles; first, it brings the first level of genomic compaction, wrapping around ~ 147 bp of DNA in 1.75 turns (255). Second, it interacts with transcription factors and displays post-translational modifications (256). Third, nucleosomes can self-assemble into higher-order compaction of chromatin (225). We have discussed the sequence-dependent nucleosome structure, interactions between the dinucleosomes wrapped by the Widom 601 sequence and the non-specific sequence (111), and the interactions between the translation factor NF- κ B and nucleosome (240). In Chapter 7, we investigate the positioning of the nucleosome and the internucleosomal interactions in a higher-order structure, tetranucleosome. As discussed in the result section, further analyses are needed for the rhizavidin-labeled samples and the non-specific DNA substrate samples to elucidate the role of DNA sequence in the positioning and internucleosomal interactions. Moreover, an extension of the current study to use HS-AFM and characterize the dynamics of the higher-order structures of nucleosome array is another potential for future studies.

It has been demonstrated that deficient rescue of the replication can cause replication fork breakdown, trigger spontaneous DNA breakage, leading to mutability and cancer (257). Further investigation of the protein-DNA and protein-protein interactions during the replication rescue process will open new venues for pharmaceutical and biomedical research. In addition, knowledge generated in the assembly of nucleosome array will shed light on the characterization of the pathogenic events caused by abnormal nucleosome dynamics, such as the aberrant chromatin remodeling in the pathology of Huntington's disease.

Chapter 9. REFERENCES

1. Kornberg, A., and Baker, T. A. (1992) *DNA replication*, Wh Freeman New York
2. Bell, S. P., and Dutta, A. (2002) DNA replication in eukaryotic cells. *Annual review of biochemistry* **71**, 333-374
3. Huberman, J. A., and Riggs, A. D. (1968) On the mechanism of DNA replication in mammalian chromosomes. *Journal of molecular biology* **32**, 327-341
4. Kunkel, T. A. (2004) DNA replication fidelity. *Journal of Biological Chemistry* **279**, 16895-16898
5. Kunkel, T. A., and Bebenek, K. (2000) DNA replication fidelity. *Annual review of biochemistry* **69**, 497-529
6. Clayton, D. A. (1982) Replication of animal mitochondrial DNA. *Cell* **28**, 693-705
7. Gilbert, W., and Dressler, D. (1968) DNA replication: the rolling circle model. in *Cold Spring Harbor Symposia on Quantitative Biology*, Cold Spring Harbor Laboratory Press
8. Burhans, W. C., Vassilev, L. T., Caddle, M. S., Heintz, N. H., and DePamphills, M. L. (1990) Identification of an origin of bidirectional DNA replication in mammalian chromosomes. *Cell* **62**, 955-965
9. Danna, K. J., and Nathans, D. (1972) Bidirectional replication of simian virus 40 DNA. *Proceedings of the National Academy of Sciences* **69**, 3097-3100
10. Bhagavan, N., and Ha, C.-E. (2015) DNA replication, repair, and mutagenesis. *Essentials of Medical Biochemistry*, 401-417
11. Jorgensen, P., and Tyers, M. (2004) How cells coordinate growth and division. *Current biology* **14**, R1014-R1027
12. Morgan, D. O. (2007) *The cell cycle: principles of control*, New science press
13. Alberts, B., Johnson, A., Lewis, J., Raff, M., Roberts, K., and Walter, P. (2002) The initiation and completion of DNA replication in chromosomes. in *Molecular Biology of the Cell. 4th edition*, Garland Science. pp
14. Dutta, A., and Bell, S. P. (1997) Initiation of DNA replication in eukaryotic cells. *Annual review of cell and developmental biology* **13**, 293-332
15. O'Donnell, M., Langston, L., and Stillman, B. (2013) Principles and concepts of DNA replication in bacteria, archaea, and eukarya. *Cold Spring Harbor perspectives in biology* **5**, a010108

16. Windgassen, T. A., Wessel, S. R., Bhattacharyya, B., and Keck, J. L. (2018) Mechanisms of bacterial DNA replication restart. *Nucleic acids research* **46**, 504-519
17. Bianco, P. R., and Lu, Y. (2021) Single-molecule insight into stalled replication fork rescue in *Escherichia coli*. *Nucleic acids research* **49**, 4220-4238
18. Chen, J., Silver, D. P., Walpita, D., Cantor, S. B., Gazdar, A. F., Tomlinson, G., Couch, F. J., Weber, B. L., Ashley, T., and Livingston, D. M. (1998) Stable interaction between the products of the BRCA1 and BRCA2 tumor suppressor genes in mitotic and meiotic cells. *Molecular cell* **2**, 317-328
19. Campisi, J. (2001) Cellular senescence as a tumor-suppressor mechanism. *Trends in cell biology* **11**, S27-S31
20. Skarstad, K., and Katayama, T. (2013) Regulating DNA replication in bacteria. *Cold Spring Harbor perspectives in biology* **5**, a012922
21. Jacob, F., Brenner, S., and Cuzin, F. (1963) On the regulation of DNA replication in bacteria. in *Cold Spring Harbor symposia on quantitative biology*, Cold Spring Harbor Laboratory Press
22. Zakrzewska-Czerwińska, J., Jakimowicz, D., Zawilak-Pawlik, A., and Messer, W. (2007) Regulation of the initiation of chromosomal replication in bacteria. *FEMS microbiology reviews* **31**, 378-387
23. Gabbai, C. B., and Marians, K. J. (2010) Recruitment to stalled replication forks of the PriA DNA helicase and replisome-loading activities is essential for survival. *DNA repair* **9**, 202-209
24. Cortez, D. (2015) Preventing replication fork collapse to maintain genome integrity. *DNA repair* **32**, 149-157
25. Mirkin, E. V., and Mirkin, S. M. (2007) Replication fork stalling at natural impediments. *Microbiology and molecular biology reviews* **71**, 13-35
26. Voineagu, I., Narayanan, V., Lobachev, K. S., and Mirkin, S. M. (2008) Replication stalling at unstable inverted repeats: interplay between DNA hairpins and fork stabilizing proteins. *Proceedings of the National Academy of Sciences* **105**, 9936-9941
27. Kreuzer, K. N. (2013) DNA damage responses in prokaryotes: regulating gene expression, modulating growth patterns, and manipulating replication forks. *Cold Spring Harbor perspectives in biology* **5**, a012674
28. Kowalczykowski, S. C. (2000) Initiation of genetic recombination and recombination-dependent replication. *Trends in biochemical sciences* **25**, 156-165
29. McGlynn, P., and Lloyd, R. G. (2002) Replicating past lesions in DNA. *Molecular cell* **10**, 700-701

30. Marians, K. J. (2004) Mechanisms of replication fork restart in *Escherichia coli*. *Philosophical Transactions of the Royal Society of London. Series B: Biological Sciences* **359**, 71-77
31. Gupta, M. K., Guy, C. P., Yeeles, J. T., Atkinson, J., Bell, H., Lloyd, R. G., Marians, K. J., and McGlynn, P. (2013) Protein–DNA complexes are the primary sources of replication fork pausing in *Escherichia coli*. *Proceedings of the National Academy of Sciences* **110**, 7252-7257
32. Henderson, M. L., and Kreuzer, K. N. (2015) Functions that protect *Escherichia coli* from tightly bound DNA-Protein complexes created by mutant EcoRII methyltransferase. *PloS one* **10**, e0128092
33. Gan, W., Guan, Z., Liu, J., Gui, T., Shen, K., Manley, J. L., and Li, X. (2011) R-loop-mediated genomic instability is caused by impairment of replication fork progression. *Genes & development* **25**, 2041-2056
34. McGlynn, P., and Lloyd, R. G. (2002) Recombinational repair and restart of damaged replication forks. *Nature reviews Molecular cell biology* **3**, 859-870
35. Cox, M. M. (2001) Recombinational DNA repair of damaged replication forks in *Escherichia coli*: questions. *Annual review of genetics* **35**, 53-82
36. Kogoma, T. (1997) Stable DNA replication: interplay between DNA replication, homologous recombination, and transcription. *Microbiology and Molecular Biology Reviews* **61**, 212-238
37. Kuzminov, A. (1999) Recombinational repair of DNA damage in *Escherichia coli* and bacteriophage λ . *Microbiology and molecular biology reviews* **63**, 751-813
38. Kreuzer, K. N. (2005) Interplay between DNA replication and recombination in prokaryotes. *Annu. Rev. Microbiol.* **59**, 43-67
39. Sogo, J. M., Lopes, M., and Foiani, M. (2002) Fork reversal and ssDNA accumulation at stalled replication forks owing to checkpoint defects. *Science* **297**, 599-602
40. Bianco, P. R. (2015) I came to a fork in the DNA and there was RecG. *Progress in biophysics and molecular biology* **117**, 166-173
41. Manosas, M., Perumal, S. K., Bianco, P. R., Ritort, F., Benkovic, S. J., and Croquette, V. (2013) RecG and UvsW catalyse robust DNA rewinding critical for stalled DNA replication fork rescue. *Nature communications* **4**, 1-12
42. Abd Wahab, S., Choi, M., and Bianco, P. R. (2013) Characterization of the ATPase activity of RecG and RuvAB proteins on model fork structures reveals insight into stalled DNA replication fork repair. *Journal of Biological Chemistry* **288**, 26397-26409
43. Constantinou, A., Chen, X. B., McGowan, C. H., and West, S. C. (2002) Holliday junction resolution in human cells: two junction endonucleases with distinct substrate specificities. *The EMBO journal* **21**, 5577-5585

44. Sharples, G. J., Ingleston, S. M., and Lloyd, R. G. (1999) Holliday junction processing in bacteria: insights from the evolutionary conservation of RuvABC, RecG, and RusA. *Journal of bacteriology* **181**, 5543-5550
45. West, S. C. (1997) Processing of recombination intermediates by the RuvABC proteins. *Annual review of genetics* **31**, 213-244
46. Singleton, M. R., Dillingham, M. S., Gaudier, M., Kowalczykowski, S. C., and Wigley, D. B. (2004) Crystal structure of RecBCD enzyme reveals a machine for processing DNA breaks. *Nature* **432**, 187-193
47. Dillingham, M. S., Spies, M., and Kowalczykowski, S. C. (2003) RecBCD enzyme is a bipolar DNA helicase. *Nature* **423**, 893-897
48. Dillingham, M. S., and Kowalczykowski, S. C. (2008) RecBCD enzyme and the repair of double-stranded DNA breaks. *Microbiology and Molecular Biology Reviews* **72**, 642-671
49. Kidane, D., Sanchez, H., Alonso, J. C., and Graumann, P. L. (2004) Visualization of DNA double-strand break repair in live bacteria reveals dynamic recruitment of *Bacillus subtilis* RecF, RecO and RecN proteins to distinct sites on the nucleoids. *Molecular microbiology* **52**, 1627-1639
50. Courcelle, J., Carswell-Crumpton, C., and Hanawalt, P. C. (1997) recF and recR are required for the resumption of replication at DNA replication forks in *Escherichia coli*. *Proceedings of the National Academy of Sciences* **94**, 3714-3719
51. Umez, K., Chi, N.-W., and Kolodner, R. D. (1993) Biochemical interaction of the *Escherichia coli* RecF, RecO, and RecR proteins with RecA protein and single-stranded DNA binding protein. *Proceedings of the National Academy of Sciences* **90**, 3875-3879
52. Anderson, D. G., and Kowalczykowski, S. C. (1997) The translocating RecBCD enzyme stimulates recombination by directing RecA protein onto ssDNA in a χ -regulated manner. *Cell* **90**, 77-86
53. Spies, M., and Kowalczykowski, S. C. (2006) The RecA binding locus of RecBCD is a general domain for recruitment of DNA strand exchange proteins. *Molecular cell* **21**, 573-580
54. Morimatsu, K., and Kowalczykowski, S. C. (2003) RecFOR proteins load RecA protein onto gapped DNA to accelerate DNA strand exchange: a universal step of recombinational repair. *Molecular cell* **11**, 1337-1347
55. Lusetti, S. L., and Cox, M. M. (2002) The bacterial RecA protein and the recombinational DNA repair of stalled replication forks. *Annual review of biochemistry* **71**, 71-100
56. Merrikh, H., Zhang, Y., Grossman, A. D., and Wang, J. D. (2012) Replication–transcription conflicts in bacteria. *Nature Reviews Microbiology* **10**, 449-458
57. Heller, R. C., and Mariani, K. J. (2006) Replication fork reactivation downstream of a blocked nascent leading strand. *Nature* **439**, 557-562

58. Lang, K. S., and Merrikh, H. (2018) The clash of macromolecular titans: replication-transcription conflicts in bacteria. *Annual review of microbiology* **72**, 71-88
59. Pomerantz, R. T., and O'Donnell, M. (2010) What happens when replication and transcription complexes collide? *Cell Cycle* **9**, 2537-2543
60. Dillingham, M. S., Tibbles, K. L., Hunter, J. L., Bell, J. C., Kowalczykowski, S. C., and Webb, M. R. (2008) Fluorescent single-stranded DNA binding protein as a probe for sensitive, real-time assays of helicase activity. *Biophysical journal* **95**, 3330-3339
61. Krauss, G., Sindermann, H., Schomburg, U., and Maass, G. (1981) Escherichia coli single-strand deoxyribonucleic acid binding protein: stability, specificity, and kinetics of complexes with oligonucleotides and deoxyribonucleic acid. *Biochemistry* **20**, 5346-5352
62. Kur, J., Olszewski, M., Długołęcka, A., and Filipkowski, P. (2005) Single-stranded DNA-binding proteins (SSBs)--sources and applications in molecular biology. *Acta Biochimica Polonica* **52**, 569-574
63. Lohman, T. M., and Ferrari, M. E. (1994) Escherichia coli single-stranded DNA-binding protein: multiple DNA-binding modes and cooperativities. *Annual review of biochemistry* **63**, 527-570
64. McEntee, K., Weinstock, G. M., and Lehman, I. (1980) recA protein-catalyzed strand assimilation: stimulation by Escherichia coli single-stranded DNA-binding protein. *Proceedings of the National Academy of Sciences* **77**, 857-861
65. Genschel, J., Curth, U., and Urbanke, C. (2000) Interaction of E. coli single-stranded DNA binding protein (SSB) with exonuclease I. The carboxy-terminus of SSB is the recognition site for the nuclease.
66. Bianco, P. R. (2017) The tale of SSB. *Progress in biophysics and molecular biology* **127**, 111-118
67. Umezu, K., and Kolodner, R. D. (1994) Protein interactions in genetic recombination in Escherichia coli. Interactions involving RecO and RecR overcome the inhibition of RecA by single-stranded DNA-binding protein. *Journal of Biological Chemistry* **269**, 30005-30013
68. Revzin, A. (1990) *The biology of nonspecific DNA protein interactions*, CRC Press
69. Mahdi, A. A., McGlynn, P., Levett, S. D., and Lloyd, R. G. (1997) DNA binding and helicase domains of the Escherichia coli recombination protein RecG. *Nucleic acids research* **25**, 3875-3880
70. Peter, M., and Lloyd, R. G. (1999) RecG helicase activity at three-and four-strand DNA structures. *Nucleic acids research* **27**, 3049-3056
71. Sun, Z., Tan, H. Y., Bianco, P. R., and Lyubchenko, Y. L. (2015) Remodeling of RecG Helicase at the DNA Replication Fork by SSB Protein. *Sci Rep* **5**, 9625

72. Sun, Z., Hashemi, M., Warren, G., Bianco, P. R., and Lyubchenko, Y. L. (2018) Dynamics of the interaction of RecG protein with stalled replication forks. *Biochemistry* **57**, 1967-1976
73. Tan, H. Y., Wilczek, L. A., Pottinger, S., Manosas, M., Yu, C., Nguyenduc, T., and Bianco, P. R. (2017) The intrinsically disordered linker of E. coli SSB is critical for the release from single-stranded DNA. *Protein Science* **26**, 700-717
74. Seigneur, M., Bidnenko, V., Ehrlich, S. D., and Michel, B. (1998) RuvAB acts at arrested replication forks. *Cell* **95**, 419-430
75. Parsons, C. A., and West, S. C. (1993) Formation of a RuvAB-Holliday junction complex in vitro. *Journal of molecular biology* **232**, 397-405
76. Iwasaki, H., Takahagi, M., Shiba, T., Nakata, A., and Shinagawa, H. (1991) Escherichia coli RuvC protein is an endonuclease that resolves the Holliday structure. *The EMBO journal* **10**, 4381-4389
77. Gregg, A. V., McGlynn, P., Jaktaji, R. P., and Lloyd, R. G. (2002) Direct rescue of stalled DNA replication forks via the combined action of PriA and RecG helicase activities. *Molecular cell* **9**, 241-251
78. Angeli, P., Pria, M. D., de Bei, E., Albino, G., Caregaro, L., Merkel, C., Ceolotto, G., and Gatta, A. (1994) Randomized clinical study of the efficacy of amiloride and potassium canrenoate in nonazotemic cirrhotic patients with ascites. *Hepatology* **19**, 72-79
79. Angeli, P., Albino, G., Carraro, P., Pria, M., Merkel, C., Caregaro, L., De Bei, E., Bortoluzzi, A., Plebani, M., and Gatta, A. (1996) Cirrhosis and muscle cramps: evidence of a causal relationship. *Hepatology* **23**, 264-273
80. Betterle, C., Rossi, A., Pria, S. D., Artifoni, A., Pedini, B., Gavasso, S., and Caretto, A. (1993) Premature ovarian failure: autoimmunity and natural history. *Clinical endocrinology* **39**, 35-43
81. Marians, K. J. (2000) PriA-directed replication fork restart in Escherichia coli. *Trends in biochemical sciences* **25**, 185-189
82. Wickner, S., and Hurwitz, J. (1975) Association of phiX174 DNA-dependent ATPase activity with an Escherichia coli protein, replication factor Y, required for in vitro synthesis of phiX174 DNA. *Proceedings of the National Academy of Sciences* **72**, 3342-3346
83. Masai, H., Tanaka, T., and Kohda, D. (2010) Stalled replication forks: making ends meet for recognition and stabilization. *Bioessays* **32**, 687-697
84. Manhart, C. M., and McHenry, C. S. (2013) The PriA replication restart protein blocks replicase access prior to helicase assembly and directs template specificity through its ATPase activity. *Journal of Biological Chemistry* **288**, 3989-3999
85. Bhattacharyya, B., George, N. P., Thurmes, T. M., Zhou, R., Jani, N., Wessel, S. R., Sandler, S. J., Ha, T., and Keck, J. L. (2014) Structural mechanisms of PriA-mediated

- DNA replication restart. *Proceedings of the National Academy of Sciences* **111**, 1373-1378
86. Yu, C., Tan, H. Y., Choi, M., Stanenas, A. J., Byrd, A. K., D. Raney, K., Cohan, C. S., and Bianco, P. R. (2016) SSB binds to the RecG and PriA helicases in vivo in the absence of DNA. *Genes to Cells* **21**, 163-184
 87. Cadman, C. J., and McGlynn, P. (2004) PriA helicase and SSB interact physically and functionally. *Nucleic acids research* **32**, 6378-6387
 88. Bailey, S., Eliason, W. K., and Steitz, T. A. (2007) Structure of hexameric DnaB helicase and its complex with a domain of DnaG primase. *Science* **318**, 459-463
 89. LeBowitz, J., and McMacken, R. (1986) The Escherichia coli dnaB replication protein is a DNA helicase. *Journal of Biological Chemistry* **261**, 4738-4748
 90. Isenberg, I. (1979) Histones. *Annual review of biochemistry* **48**, 159-191
 91. McGhee, J. D., and Felsenfeld, G. (1980) Nucleosome structure. *Annual review of biochemistry* **49**, 1115-1156
 92. Travers, A. (1987) DNA bending and nucleosome positioning. *Trends in Biochemical Sciences* **12**, 108-112
 93. Fenley, A. T., Adams, D. A., and Onufriev, A. V. (2010) Charge state of the globular histone core controls stability of the nucleosome. *Biophysical journal* **99**, 1577-1585
 94. Henikoff, S. (2008) Nucleosome destabilization in the epigenetic regulation of gene expression. *Nature Reviews Genetics* **9**, 15-26
 95. Gansen, A., Valeri, A., Hauger, F., Felekyan, S., Kalinin, S., Tóth, K., Langowski, J., and Seidel, C. A. (2009) Nucleosome disassembly intermediates characterized by single-molecule FRET. *Proceedings of the National Academy of Sciences* **106**, 15308-15313
 96. Widom, J. (2001) Role of DNA sequence in nucleosome stability and dynamics. *Quarterly reviews of biophysics* **34**, 269-324
 97. Hendrich, B., and Bickmore, W. (2001) Human diseases with underlying defects in chromatin structure and modification. *Human molecular genetics* **10**, 2233-2242
 98. Arya, G., and Schlick, T. (2009) A tale of tails: how histone tails mediate chromatin compaction in different salt and linker histone environments. *The Journal of Physical Chemistry A* **113**, 4045-4059
 99. Sanborn, A. L., Rao, S. S., Huang, S.-C., Durand, N. C., Huntley, M. H., Jewett, A. I., Bochkov, I. D., Chinnappan, D., Cutkosky, A., and Li, J. (2015) Chromatin extrusion explains key features of loop and domain formation in wild-type and engineered genomes. *Proceedings of the National Academy of Sciences* **112**, E6456-E6465

100. Ricci, M. A., Manzo, C., García-Parajo, M. F., Lakadamyali, M., and Cosma, M. P. (2015) Chromatin fibers are formed by heterogeneous groups of nucleosomes in vivo. *Cell* **160**, 1145-1158
101. Nishino, Y., Eltsov, M., Joti, Y., Ito, K., Takata, H., Takahashi, Y., Hihara, S., Frangakis, A. S., Imamoto, N., and Ishikawa, T. (2012) Human mitotic chromosomes consist predominantly of irregularly folded nucleosome fibres without a 30-nm chromatin structure. *The EMBO journal* **31**, 1644-1653
102. Li, Y., Roth, E., Agrawal, V., Eshein, A., Fredrick, J., Almassalha, L., Shim, A., Bleher, R., Dravid, V. P., and Backman, V. (2019) Quantifying three-dimensional chromatin organization utilizing scanning transmission electron microscopy: Chromstem. *bioRxiv*, 636209
103. Hsieh, T.-H. S., Weiner, A., Lajoie, B., Dekker, J., Friedman, N., and Rando, O. J. (2015) Mapping nucleosome resolution chromosome folding in yeast by micro-C. *Cell* **162**, 108-119
104. Eltsov, M., MacLellan, K. M., Maeshima, K., Frangakis, A. S., and Dubochet, J. (2008) Analysis of cryo-electron microscopy images does not support the existence of 30-nm chromatin fibers in mitotic chromosomes in situ. *Proceedings of the National Academy of Sciences* **105**, 19732-19737
105. Chen, C., Lim, H. H., Shi, J., Tamura, S., Maeshima, K., Surana, U., and Gan, L. (2016) Budding yeast chromatin is dispersed in a crowded nucleoplasm in vivo. *Molecular biology of the cell* **27**, 3357-3368
106. Moraru, M., and Schalch, T. (2019) Chromatin fiber structural motifs as regulatory hubs of genome function? *Essays in biochemistry* **63**, 123-132
107. Nuebler, J., Fudenberg, G., Imakaev, M., Abdennur, N., and Mirny, L. A. (2018) Chromatin organization by an interplay of loop extrusion and compartmental segregation. *Proceedings of the National Academy of Sciences* **115**, E6697-E6706
108. Alvarado, W., Moller, J., Ferguson, A. L., and de Pablo, J. J. (2021) Tetranucleosome Interactions Drive Chromatin Folding. *ACS Central Science*
109. Ohno, M., Ando, T., Priest, D. G., Kumar, V., Yoshida, Y., and Taniguchi, Y. (2019) Sub-nucleosomal genome structure reveals distinct nucleosome folding motifs. *Cell* **176**, 520-534. e525
110. Song, F., Chen, P., Sun, D., Wang, M., Dong, L., Liang, D., Xu, R.-M., Zhu, P., and Li, G. (2014) Cryo-EM study of the chromatin fiber reveals a double helix twisted by tetranucleosomal units. *Science* **344**, 376-380
111. Stormberg, T., Stumme-Diers, M., and Lyubchenko, Y. L. (2019) Sequence-dependent nucleosome nanoscale structure characterized by atomic force microscopy. *The FASEB Journal* **33**, 10916-10923
112. Zeman, M. K., and Cimprich, K. A. (2014) Causes and consequences of replication stress. *Nature cell biology* **16**, 2-9

113. Mazouzi, A., Velimezi, G., and Loizou, J. I. (2014) DNA replication stress: causes, resolution and disease. *Experimental cell research* **329**, 85-93
114. Liao, H., Ji, F., Helleday, T., and Ying, S. (2018) Mechanisms for stalled replication fork stabilization: new targets for synthetic lethality strategies in cancer treatments. *EMBO reports* **19**, e46263
115. McGlynn, P., and Lloyd, R. G. (2001) Action of RuvAB at replication fork structures. *Journal of Biological Chemistry* **276**, 41938-41944
116. Buss, J. A., Kimura, Y., and Bianco, P. R. (2008) RecG interacts directly with SSB: implications for stalled replication fork regression. *Nucleic acids research* **36**, 7029-7042
117. Courcelle, J., Donaldson, J. R., Chow, K.-H., and Courcelle, C. T. (2003) DNA damage-induced replication fork regression and processing in Escherichia coli. *Science* **299**, 1064-1067
118. Robu, M. E., Inman, R. B., and Cox, M. M. (2001) RecA protein promotes the regression of stalled replication forks in vitro. *Proceedings of the National Academy of Sciences* **98**, 8211-8218
119. McGlynn, P., Lloyd, R. G., and Marians, K. J. (2001) Formation of Holliday junctions by regression of nascent DNA in intermediates containing stalled replication forks: RecG stimulates regression even when the DNA is negatively supercoiled. *Proceedings of the National Academy of Sciences* **98**, 8235-8240
120. Heller, R. C., and Marians, K. J. (2005) Unwinding of the Nascent Lagging Strand by Rep and PriA Enables the Direct Restart of Stalled Replication Forks*[boxs]. *Journal of Biological Chemistry* **280**, 34143-34151
121. Sandler, S. J., and Marians, K. J. (2000) Role of PriA in replication fork reactivation in Escherichia coli. *Journal of bacteriology* **182**, 9-13
122. Liu, J., and Marians, K. J. (1999) PriA-directed assembly of a primosome on D loop DNA. *Journal of Biological Chemistry* **274**, 25033-25041
123. Binnig, G., Quate, C. F., and Gerber, C. (1986) Atomic force microscope. *Phys Rev Lett* **56**, 930-933
124. Binnig, G., and Rohrer, H. (1987) Scanning tunneling microscopy—from birth to adolescence. *reviews of modern physics* **59**, 615
125. Drake, B., Prater, C. B., Weisenhorn, A. L., Gould, S. A., Albrecht, T. R., Quate, C. F., Cannell, D. S., Hansma, H. G., and Hansma, P. K. (1989) Imaging crystals, polymers, and processes in water with the atomic force microscope. *Science* **243**, 1586-1589
126. Lyubchenko, Y. L. (2018) Direct AFM visualization of the nanoscale dynamics of biomolecular complexes. *Journal of physics D: Applied physics* **51**, 403001
127. Alessandrini, A., and Facci, P. (2005) AFM: a versatile tool in biophysics. *Measurement science and technology* **16**, R65

128. Henderson, R. M., Schneider, S., Li, Q., Hornby, D., White, S. J., and Oberleithner, H. (1996) Imaging ROMK1 inwardly rectifying ATP-sensitive K⁺ channel protein using atomic force microscopy. *Proc Natl Acad Sci U S A* **93**, 8756-8760
129. Liang, W., Shi, H., Yang, X., Wang, J., Yang, W., Zhang, H., and Liu, L. (2020) Recent advances in AFM-based biological characterization and applications at multiple levels. *Soft Matter*
130. Meyer, E. (1992) Atomic force microscopy. *Progress in surface science* **41**, 3-49
131. Garcia, R., and Perez, R. (2002) Dynamic atomic force microscopy methods. *Surface science reports* **47**, 197-301
132. Rief, M., Gautel, M., Oesterhelt, F., Fernandez, J. M., and Gaub, H. E. (1997) Reversible unfolding of individual titin immunoglobulin domains by AFM. *Science* **276**, 1109-1112
133. Rief, M., Oesterhelt, F., Heymann, B., and Gaub, H. E. (1997) Single Molecule Force Spectroscopy on Polysaccharides by Atomic Force Microscopy. *Science* **275**, 1295-1297
134. Neuman, K. C., and Nagy, A. (2008) Single-molecule force spectroscopy: optical tweezers, magnetic tweezers and atomic force microscopy. *Nat Methods* **5**, 491-505
135. Lyubchenko, Y. L., Gall, A. A., and Shlyakhtenko, L. S. (2014) Visualization of DNA and protein-DNA complexes with atomic force microscopy. *Methods Mol Biol* **1117**, 367-384
136. Howland, R., and Benatar, L. (1996) *A Practical Guide: To Scanning Probe Microscopy*, Park scientific instruments
137. SLADE, A., and YIP, C. (2005) Scanning probe microscopy—applications for the study of soft materials. in *Molecular Interfacial Phenomena of Polymers and Biopolymers*, Elsevier. pp 161-213
138. Lyubchenko, Y. L., Gall, A. A., and Shlyakhtenko, L. S. (2014) Visualization of DNA and Protein–DNA Complexes with Atomic Force Microscopy. in *Electron Microscopy*, Springer. pp 367-384
139. Wickramasinghe, H. (2012) Development of the technology and applications of the scanning probe microscope. *Microsc Anal* **26**, 27-30
140. Zhong, Q., Inniss, D., Kjoller, K., and Elings, V. (1993) Fractured polymer/silica fiber surface studied by tapping mode atomic force microscopy. *Surface Science Letters* **290**, L688-L692
141. Shih, H. J., and Shih, P. J. (2015) Tip Effect of the Tapping Mode of Atomic Force Microscope in Viscous Fluid Environments. *Sensors (Basel)* **15**, 18381-18401
142. Magonov, S., Elings, V., and Whangbo, M.-H. (1997) Phase imaging and stiffness in tapping-mode atomic force microscopy. *Surface science* **375**, L385-L391

143. Cleveland, J., Anczykowski, B., Schmid, A., and Elings, V. (1998) Energy dissipation in tapping-mode atomic force microscopy. *Applied Physics Letters* **72**, 2613-2615
144. Hansma, P., Cleveland, J., Radmacher, M., Walters, D., Hillner, P., Bezanilla, M., Fritz, M., Vie, D., Hansma, H., and Prater, C. (1994) Tapping mode atomic force microscopy in liquids. *Applied Physics Letters* **64**, 1738-1740
145. Yang, J., Takeyasu, K., and Shao, Z. (1992) Atomic force microscopy of DNA molecules. *FEBS letters* **301**, 173-176
146. Lyubchenko, Y. L., Gall, A. A., Shlyakhtenko, L. S., Harrington, R. E., Jacobs, B. L., Oden, P. I., and Lindsay, S. M. (1992) Atomic force microscopy imaging of double stranded DNA and RNA. *Journal of biomolecular structure and dynamics* **10**, 589-606
147. Allen, M. J., Dong, X. F., O'Neill, T. E., Yau, P., Kowalczykowski, S. C., Gatewood, J., Balhorn, R., and Bradbury, E. M. (1993) Atomic force microscope measurements of nucleosome cores assembled along defined DNA sequences. *Biochemistry* **32**, 8390-8396
148. Hegner, M., Wagner, P., and Semenza, G. (1993) Immobilizing DNA on gold via thiol modification for atomic force microscopy imaging in buffer solutions. *FEBS letters* **336**, 452-456
149. Shlyakhtenko, L. S., Gall, A. A., and Lyubchenko, Y. L. (2013) Mica functionalization for imaging of DNA and protein-DNA complexes with atomic force microscopy. *Methods Mol Biol* **931**, 295-312
150. Lyubchenko, Y., Shlyakhtenko, L., Harrington, R., Oden, P., and Lindsay, S. (1993) Atomic force microscopy of long DNA: imaging in air and under water. *Proceedings of the National Academy of Sciences* **90**, 2137-2140
151. Lyubchenko, Y. L., Gall, A. A., and Shlyakhtenko, L. S. (2001) Atomic force microscopy of DNA and protein-DNA complexes using functionalized mica substrates. in *DNA-Protein Interactions*, Springer. pp 569-578
152. Lyubchenko, Y., Oden, P., Lampner, D., Lindsay, S., and Dunker, K. (1993) Atomic force microscopy of DNA and bacteriophage in air, water and propanol: the role of adhesion forces. *Nucleic acids research* **21**, 1117-1123
153. Lyubchenko, Y. L., Jacobs, B., Lindsay, S., and Stasiak, A. (1995) Atomic force microscopy of nucleoprotein complexes. *Scanning Microscopy* **9**, 8
154. Lyubchenko, Y. L., Blankenship, R. E., Gall, A. A., Lindsay, S., Thiemann, O., Simpson, L., and Shlyakhtenko, L. S. (1996) Atomic force microscopy of DNA, nucleoproteins and cellular complexes: the use of functionalized substrates. *Scanning Microscopy* **1996**, 9
155. Shlyakhtenko, L. S., Gall, A. A., Weimer, J. J., Hawn, D. D., and Lyubchenko, Y. L. (1999) Atomic force microscopy imaging of DNA covalently immobilized on a functionalized mica substrate. *Biophysical journal* **77**, 568-576

156. Shlyakhtenko, L. S., Potaman, V. N., Sinden, R. R., Gall, A. A., and Lyubchenko, Y. L. (2000) Structure and dynamics of three-way DNA junctions: atomic force microscopy studies. *Nucleic acids research* **28**, 3472-3477
157. Shlyakhtenko, L. S., Gall, A. A., Filonov, A., Cerovac, Z., Lushnikov, A., and Lyubchenko, Y. L. (2003) Silatrane-based surface chemistry for immobilization of DNA, protein-DNA complexes and other biological materials. *Ultramicroscopy* **97**, 279-287
158. Shlyakhtenko, L. S., Miloseska, L., Potaman, V. N., Sinden, R. R., and Lyubchenko, Y. L. (2003) Intersegmental interactions in supercoiled DNA: atomic force microscope study. *Ultramicroscopy* **97**, 263-270
159. Lyubchenko, Y. L., and Shlyakhtenko, L. S. (2009) AFM for analysis of structure and dynamics of DNA and protein-DNA complexes. *Methods* **47**, 206-213
160. Pavlicek, J. W., Oussatcheva, E. A., Sinden, R. R., Potaman, V. N., Sankey, O. F., and Lyubchenko, Y. L. (2004) Supercoiling-induced DNA bending. *Biochemistry* **43**, 10664-10668
161. Lyubchenko, Y. L., Sherman, S., Shlyakhtenko, L. S., and Uversky, V. N. (2006) Nanoimaging for protein misfolding and related diseases. *Journal of cellular biochemistry* **99**, 52-70
162. Riener, C. K., Stroh, C. M., Ebner, A., Klampfl, C., Gall, A. A., Romanin, C., Lyubchenko, Y. L., Hinterdorfer, P., and Gruber, H. J. (2003) Simple test system for single molecule recognition force microscopy. *Analytica Chimica Acta* **479**, 59-75
163. Ando, T., Uchihashi, T., Kodera, N., Yamamoto, D., Miyagi, A., Taniguchi, M., and Yamashita, H. (2008) High-speed AFM and nano-visualization of biomolecular processes. *Pflugers Arch* **456**, 211-225
164. Ando, T., Uchihashi, T., Kodera, N., Yamamoto, D., Taniguchi, M., Miyagi, A., and Yamashita, H. (2007) High-speed atomic force microscopy for observing dynamic biomolecular processes. *J Mol Recognit* **20**, 448-458
165. Yamamoto, D., Uchihashi, T., Kodera, N., Yamashita, H., Nishikori, S., Ogura, T., Shibata, M., and Ando, T. (2010) High-speed atomic force microscopy techniques for observing dynamic biomolecular processes. *Methods Enzymol* **475**, 541-564
166. Ando, T., Kodera, N., Takai, E., Maruyama, D., Saito, K., and Toda, A. (2001) A high-speed atomic force microscope for studying biological macromolecules. *Proc Natl Acad Sci U S A* **98**, 12468-12472
167. Suzuki, Y., Higuchi, Y., Hizume, K., Yokokawa, M., Yoshimura, S. H., Yoshikawa, K., and Takeyasu, K. (2010) Molecular dynamics of DNA and nucleosomes in solution studied by fast-scanning atomic force microscopy. *Ultramicroscopy* **110**, 682-688
168. Ando, T., Uchihashi, T., and Kodera, N. (2013) High-speed AFM and applications to biomolecular systems. *Annu Rev Biophys* **42**, 393-414

169. Banerjee, S., Sun, Z., Hayden, E. Y., Teplow, D. B., and Lyubchenko, Y. L. (2017) Nanoscale dynamics of amyloid β -42 oligomers as revealed by high-speed atomic force microscopy. *ACS nano* **11**, 12202-12209
170. Liu, R., McAllister, C., Lyubchenko, Y., and Sierks, M. R. (2004) Residues 17–20 and 30–35 of beta-amyloid play critical roles in aggregation. *Journal of neuroscience research* **75**, 162-171
171. Lyubchenko, Y. L., Shlyakhtenko, L. S., and Ando, T. (2011) Imaging of nucleic acids with atomic force microscopy. *Methods* **54**, 274-283
172. McAllister, C., Karymov, M. A., Kawano, Y., Lushnikov, A. Y., Mikheikin, A., Uversky, V. N., and Lyubchenko, Y. L. (2005) Protein interactions and misfolding analyzed by AFM force spectroscopy. *Journal of molecular biology* **354**, 1028-1042
173. Miyagi, A., Ando, T., and Lyubchenko, Y. L. (2011) Dynamics of nucleosomes assessed with time-lapse high-speed atomic force microscopy. *Biochemistry* **50**, 7901-7908
174. Uversky, V. N., Yamin, G., Munishkina, L. A., Karymov, M. A., Millett, I. S., Doniach, S., Lyubchenko, Y. L., and Fink, A. L. (2005) Effects of nitration on the structure and aggregation of α -synuclein. *Molecular Brain Research* **134**, 84-102
175. Watson, D., Castaño, E., Kokjohn, T. A., Kuo, Y.-M., Lyubchenko, Y., Pinsky, D., Connolly, E. S., Esh, C., Luehrs, D. C., and Stine, W. B. (2005) Physicochemical characteristics of soluble oligomeric A β and their pathologic role in Alzheimer's disease. *Neurological research* **27**, 869-881
176. Bezanilla, M., Manne, S., Laney, D. E., Lyubchenko, Y. L., and Hansma, H. G. (1995) Adsorption of DNA to mica, silylated mica, and minerals: characterization by atomic force microscopy. *Langmuir* **11**, 655-659
177. Lonskaya, I., Potaman, V. N., Shlyakhtenko, L. S., Oussatcheva, E. A., Lyubchenko, Y. L., and Soldatenkov, V. A. (2005) Regulation of poly (ADP-ribose) polymerase-1 by DNA structure-specific binding. *Journal of biological chemistry* **280**, 17076-17083
178. Lyubchenko, Y. L., and Shlyakhtenko, L. S. (1997) Visualization of supercoiled DNA with atomic force microscopy in situ. *Proceedings of the National Academy of Sciences* **94**, 496-501
179. Stumme-Diers, M. P., Stormberg, T., Sun, Z., and Lyubchenko, Y. L. (2019) Probing The Structure And Dynamics Of Nucleosomes Using Atomic Force Microscopy Imaging. *J Vis Exp*
180. Gilmore, J. L., Suzuki, Y., Tamulaitis, G., Siksnys, V., Takeyasu, K., and Lyubchenko, Y. L. (2009) Single-molecule dynamics of the DNA-EcoRII protein complexes revealed with high-speed atomic force microscopy. *Biochemistry* **48**, 10492-10498
181. Cox, M. M., Goodman, M. F., Kreuzer, K. N., Sherratt, D. J., Sandler, S. J., and Mariani, K. J. (2000) The importance of repairing stalled replication forks. *Nature* **404**, 37-41

182. Michel, B., Sinha, A. K., and Leach, D. R. (2018) Replication fork breakage and restart in *Escherichia coli*. *Microbiology and Molecular Biology Reviews* **82**, e00013-00018
183. Allen Jr, G. C., and Kornberg, A. (1993) Assembly of the primosome of DNA replication in *Escherichia coli*. *Journal of Biological Chemistry* **268**, 19204-19209
184. Chen, H.-W., North, S. H., and Nakai, H. (2004) Properties of the PriA helicase domain and its role in binding PriA to specific DNA structures. *Journal of Biological Chemistry* **279**, 38503-38512
185. Tanaka, T., Mizukoshi, T., Taniyama, C., Kohda, D., Arai, K.-i., and Masai, H. (2002) DNA binding of PriA protein requires cooperation of the N-terminal D-loop/arrested-fork binding and C-terminal helicase domains. *Journal of Biological Chemistry* **277**, 38062-38071
186. Ouzounis, C. A., and Blencowe, B. J. (1991) Bacterial DNA replication initiation factor priA is related to proteins belonging to the 'DEAD-box' family. *Nucleic acids research* **19**, 6953
187. Tanaka, T., Mizukoshi, T., Sasaki, K., Kohda, D., and Masai, H. (2007) *Escherichia coli* PriA protein, two modes of DNA binding and activation of ATP hydrolysis. *Journal of Biological Chemistry* **282**, 19917-19927
188. Tanaka, T., Taniyama, C., Arai, K. I., and Masai, H. (2003) ATPase/helicase motif mutants of *Escherichia coli* PriA protein essential for recombination-dependent DNA replication. *Genes to Cells* **8**, 251-261
189. Windgassen, T. A., Leroux, M., Satyshur, K. A., Sandler, S. J., and Keck, J. L. (2018) Structure-specific DNA replication-fork recognition directs helicase and replication restart activities of the PriA helicase. *Proceedings of the National Academy of Sciences* **115**, E9075-E9084
190. Costes, A., Lecointe, F., McGovern, S., Quevillon-Cheruel, S., and Polard, P. (2010) The C-terminal domain of the bacterial SSB protein acts as a DNA maintenance hub at active chromosome replication forks. *PLoS genetics* **6**, e1001238
191. Cadman, C. J., Lopper, M., Moon, P. B., Keck, J. L., and McGlynn, P. (2005) PriB stimulates PriA helicase via an interaction with single-stranded DNA. *Journal of Biological Chemistry* **280**, 39693-39700
192. Windgassen, T. A., Leroux, M., Sandler, S. J., and Keck, J. L. (2019) Function of a strand-separation pin element in the PriA DNA replication restart helicase. *Journal of Biological Chemistry* **294**, 2801-5614
193. Lohman, T. M., Green, J. M., and Beyer, R. S. (1986) Large-scale overproduction and rapid purification of the *Escherichia coli* ssb gene product. Expression of the ssb gene under. lambda. PL control. *Biochemistry* **25**, 21-25
194. Ding, W., Tan, H. Y., Zhang, J. X., Wilczek, L. A., Hsieh, K. R., Mulkin, J. A., and Bianco, P. R. (2020) The mechanism of single strand binding protein–RecG binding: Implications for SSB interactome function. *Protein Science* **29**, 1211-1227

195. Bianco, P. R., Pottinger, S., Tan, H. Y., Nguyenduc, T., Rex, K., and Varshney, U. (2017) The IDL of E. coli SSB links ssDNA and protein binding by mediating protein–protein interactions. *Protein Science* **26**, 227-241
196. Liu, J., Choi, M., Stanenas, A. G., Byrd, A. K., Raney, K. D., Cohan, C., and Bianco, P. R. (2011) Novel, fluorescent, SSB protein chimeras with broad utility. *Protein Science* **20**, 1005-1020
197. Jones, J. M., and Nakai, H. (2001) Escherichia coli PriA helicase: fork binding orients the helicase to unwind the lagging strand side of arrested replication forks. *Journal of molecular biology* **312**, 935-947
198. Nurse, P., Liu, J., and Marians, K. J. (1999) Two modes of PriA binding to DNA. *Journal of Biological Chemistry* **274**, 25026-25032
199. Kozlov, A. G., Jezewska, M. J., Bujalowski, W., and Lohman, T. M. (2010) Binding specificity of Escherichia coli single-stranded DNA binding protein for the χ subunit of DNA pol III holoenzyme and PriA helicase. *Biochemistry* **49**, 3555-3566
200. Bagchi, D., Manosas, M., Zhang, W., Manthei, K. A., Hodeib, S., Ducos, B., Keck, J. L., and Croquette, V. (2018) Single molecule kinetics uncover roles for E. coli RecQ DNA helicase domains and interaction with SSB. *Nucleic acids research* **46**, 8500-8515
201. Mills, M., Harami, G. M., Seol, Y., Gyimesi, M., Martina, M., Kovács, Z. J., Kovács, M., and Neuman, K. C. (2017) RecQ helicase triggers a binding mode change in the SSB–DNA complex to efficiently initiate DNA unwinding. *Nucleic acids research* **45**, 11878-11890
202. Bell, J. C., Liu, B., and Kowalczykowski, S. C. (2015) Imaging and energetics of single SSB-ssDNA molecules reveal intramolecular condensation and insight into RecOR function. *Elife* **4**, e08646
203. Hobbs, M. D., Sakai, A., and Cox, M. M. (2007) SSB protein limits RecOR binding onto single-stranded DNA. *Journal of Biological Chemistry* **282**, 11058-11067
204. Shereda, R. D., Kozlov, A. G., Lohman, T. M., Cox, M. M., and Keck, J. L. (2008) SSB as an organizer/mobilizer of genome maintenance complexes. *Critical reviews in biochemistry and molecular biology* **43**, 289-318
205. Slocum, S. L., Buss, J. A., Kimura, Y., and Bianco, P. R. (2007) Characterization of the ATPase activity of the Escherichia coli RecG protein reveals that the preferred cofactor is negatively supercoiled DNA. *Journal of molecular biology* **367**, 647-664
206. Sandler, S. J. (2000) Multiple genetic pathways for restarting DNA replication forks in Escherichia coli K-12. *Genetics* **155**, 487-497
207. Kitazawa, M., Ohta, R., Okita, T., Tanaka, J., and Tanemura, M. (2007) Mechanical properties of single carbon nanofibers grown on tips of scanning probe microscopy cantilevers by ion irradiation. *Japanese Journal of Applied Physics* **46**, 6324

208. Jones, J. M., and Nakai, H. (1999) Duplex opening by primosome protein PriA for replisome assembly on a recombination intermediate. *Journal of molecular biology* **289**, 503-515
209. Gabbai, C. B., and Marians, K. J. (2010) Recruitment to stalled replication forks of the PriA DNA helicase and replisome-loading activities is essential for survival. *DNA Repair (Amst)* **9**, 202-209
210. Choi, S., Lee, S.-W., Kim, H., and Ahn, B. (2019) Molecular characteristics of reiterative DNA unwinding by the *Caenorhabditis elegans* RecQ helicase. *Nucleic acids research* **47**, 9708-9720
211. Dessinges, M.-N., Lionnet, T., Xi, X. G., Bensimon, D., and Croquette, V. (2004) Single-molecule assay reveals strand switching and enhanced processivity of UvrD. *Proceedings of the National Academy of Sciences* **101**, 6439-6444
212. Singleton, M. R., Scaife, S., and Wigley, D. B. (2001) Structural analysis of DNA replication fork reversal by RecG. *Cell* **107**, 79-89
213. McGlynn, P., Mahdi, A. A., and Lloyd, R. G. (2000) Characterisation of the catalytically active form of RecG helicase. *Nucleic Acids Research* **28**, 2324-2332
214. Tanaka, T., and Masai, H. (2006) Stabilization of a stalled replication fork by concerted actions of two helicases. *Journal of Biological Chemistry* **281**, 3484-3493
215. Tikhomirova, A., Beletskaya, I. V., and Chalikian, T. V. (2006) Stability of DNA duplexes containing GG, CC, AA, and TT mismatches. *Biochemistry* **45**, 10563-10571
216. Rossetti, G., Dans, P. D., Gomez-Pinto, I., Ivani, I., Gonzalez, C., and Orozco, M. (2015) The structural impact of DNA mismatches. *Nucleic acids research* **43**, 4309-4321
217. Zhu, J., and Wartell, R. M. (1999) The effect of base sequence on the stability of RNA and DNA single base bulges. *Biochemistry* **38**, 15986-15993
218. Bianco, P. R. (2021) The mechanism of action of the SSB interactome reveals it is the first OB-fold family of genome guardians in prokaryotes. *Protein Science*
219. van Holde, K., and Zlatanova, J. (1995) Chromatin higher order structure: chasing a mirage? *J Biol Chem* **270**, 8373-8376
220. Kornberg, R. D., and Lorch, Y. (1999) Twenty-five years of the nucleosome, fundamental particle of the eukaryote chromosome. *Cell* **98**, 285-294
221. Zhou, K., Gaullier, G., and Luger, K. (2019) Nucleosome structure and dynamics are coming of age. *Nature structural & molecular biology* **26**, 3-13
222. Kornberg, R. D. (1974) Chromatin structure: a repeating unit of histones and DNA. *Science* **184**, 868-871

223. Armeev, G. A., Gribkova, A. K., Pospelova, I., Komarova, G. A., and Shaytan, A. K. (2019) Linking chromatin composition and structural dynamics at the nucleosome level. *Current opinion in structural biology* **56**, 46-55
224. Wilson, M. D., and Costa, A. (2017) Cryo-electron microscopy of chromatin biology. *Acta Crystallographica Section D: Structural Biology* **73**, 541-548
225. Kornberg, R. D. (1977) Structure of chromatin. *Annual review of biochemistry* **46**, 931-954
226. Elgin, S. C., and Weintraub, H. (1975) Chromosomal proteins and chromatin structure. *Annual review of biochemistry* **44**, 725-774
227. Luger, K., Mäder, A. W., Richmond, R. K., Sargent, D. F., and Richmond, T. J. (1997) Crystal structure of the nucleosome core particle at 2.8 Å resolution. *Nature* **389**, 251-260
228. Tremethick, D. J. (2007) Higher-order structures of chromatin: the elusive 30 nm fiber. *Cell* **128**, 651-654
229. Schalch, T., Duda, S., Sargent, D. F., and Richmond, T. J. (2005) X-ray structure of a tetranucleosome and its implications for the chromatin fibre. *Nature* **436**, 138-141
230. Chien, F.-T., and van Noort, J. (2009) 10 years of tension on chromatin: results from single molecule force spectroscopy. *Current pharmaceutical biotechnology* **10**, 474-485
231. Robinson, P. J., Fairall, L., Huynh, V. A., and Rhodes, D. (2006) EM measurements define the dimensions of the “30-nm” chromatin fiber: evidence for a compact, interdigitated structure. *Proceedings of the National Academy of Sciences* **103**, 6506-6511
232. Ou, H. D., Phan, S., Deerinck, T. J., Thor, A., Ellisman, M. H., and O’shea, C. C. (2017) ChromEMT: Visualizing 3D chromatin structure and compaction in interphase and mitotic cells. *Science* **357**
233. Maeshima, K., Ide, S., and Babokhov, M. (2019) Dynamic chromatin organization without the 30-nm fiber. *Current opinion in cell biology* **58**, 95-104
234. Maeshima, K., Hihara, S., and Eltsov, M. (2010) Chromatin structure: does the 30-nm fibre exist in vivo? *Curr Opin Cell Biol* **22**, 291-297
235. Luger, K., and Hansen, J. C. (2005) Nucleosome and chromatin fiber dynamics. *Current opinion in structural biology* **15**, 188-196
236. Filenko, N. A., Palets, D. B., and Lyubchenko, Y. L. (2012) Structure and dynamics of dinucleosomes assessed by atomic force microscopy. *Journal of amino acids* **2012**
237. Lyubchenko, Y. L., and Shlyakhtenko, L. S. (2016) Imaging of DNA and Protein– DNA Complexes with Atomic Force Microscopy. *Critical Reviews™ in Eukaryotic Gene Expression* **26**

238. Pan, Y., Banerjee, S., Zagorski, K., Shlyakhtenko, L. S., Kolomeisky, A. B., and Lyubchenko, Y. L. (2018) A molecular model of the surface-assisted protein aggregation process. *bioRxiv*, 415703
239. Lyubchenko, Y. L. (2006) Atomic Force Microscopy Methods for DNA Analysis. *Encyclopedia of Analytical Chemistry: Applications, Theory and Instrumentation*, 1-31
240. Stormberg, T., Filliaux, S., Baughman, H. E., Komives, E. A., and Lyubchenko, Y. L. (2021) Transcription factor NF- κ B unravels nucleosomes. *Biochimica et Biophysica Acta (BBA)-General Subjects*, 129934
241. Stumme-Diers, M. P., Sun, Z., and Lyubchenko, Y. L. (2019) Probing the Structure and Dynamics of Nucleosomes Using AFM Imaging. *Journal of visualized experiments: JoVE*
242. Stumme-Diers, M. P., Banerjee, S., Hashemi, M., Sun, Z., and Lyubchenko, Y. L. (2018) Nanoscale dynamics of centromere nucleosomes and the critical roles of CENP-A. *Nucleic acids research* **46**, 94-103
243. Lowary, P., and Widom, J. (1998) New DNA sequence rules for high affinity binding to histone octamer and sequence-directed nucleosome positioning. *Journal of molecular biology* **276**, 19-42
244. Dorigo, B., Schalch, T., Kulangara, A., Duda, S., Schroeder, R. R., and Richmond, T. J. (2004) Nucleosome arrays reveal the two-start organization of the chromatin fiber. *Science* **306**, 1571-1573
245. Finch, J. T., and Klug, A. (1976) Solenoidal model for superstructure in chromatin. *Proceedings of the National Academy of Sciences* **73**, 1897-1901
246. Felsenfeld, G., and Groudine, M. (2003) Controlling the double helix. *Nature* **421**, 448-453
247. Routh, A., Sandin, S., and Rhodes, D. (2008) Nucleosome repeat length and linker histone stoichiometry determine chromatin fiber structure. *Proceedings of the National Academy of Sciences* **105**, 8872-8877
248. Widom, J. (1992) A relationship between the helical twist of DNA and the ordered positioning of nucleosomes in all eukaryotic cells. *Proceedings of the National Academy of Sciences* **89**, 1095-1099
249. Struhl, K., and Segal, E. (2013) Determinants of nucleosome positioning. *Nature structural & molecular biology* **20**, 267-273
250. Jiang, C., and Pugh, B. F. (2009) Nucleosome positioning and gene regulation: advances through genomics. *Nat Rev Genet* **10**, 161-172
251. van der Heijden, T., van Vugt, J. J., Logie, C., and van Noort, J. (2012) Sequence-based prediction of single nucleosome positioning and genome-wide nucleosome occupancy. *Proceedings of the National Academy of Sciences* **109**, E2514-E2522

- 252. Helppolainen, S. H., Nurminen, K. P., Määttä, J. A., Halling, K. K., Slotte, J. P., Huhtala, T., Liimatainen, T., Ylä-Herttuala, S., Airene, K. J., and Närvänen, A. (2007) Rhizavidin from *Rhizobium etli*: the first natural dimer in the avidin protein family. *Biochemical Journal* **405**, 397-405
- 253. Meir, A., Helppolainen, S. H., Podoly, E., Nordlund, H. R., Hytönen, V. P., Määttä, J. A., Wilchek, M., Bayer, E. A., Kulomaa, M. S., and Livnah, O. (2009) Crystal structure of rhizavidin: insights into the enigmatic high-affinity interaction of an innate biotin-binding protein dimer. *Journal of molecular biology* **386**, 379-390
- 254. Sun, Z., Tan, H. Y., Bianco, P. R., and Lyubchenko, Y. L. (2015) Remodeling of RecG helicase at the DNA replication fork by SSB protein. *Scientific reports* **5**, 1-7
- 255. Richmond, T. J., and Davey, C. A. (2003) The structure of DNA in the nucleosome core. *Nature* **423**, 145-150
- 256. Taverna, S. D., Li, H., Ruthenburg, A. J., Allis, C. D., and Patel, D. J. (2007) How chromatin-binding modules interpret histone modifications: lessons from professional pocket pickers. *Nature structural & molecular biology* **14**, 1025-1040
- 257. Lomonosov, M., Anand, S., Sangrithi, M., Davies, R., and Venkitaraman, A. R. (2003) Stabilization of stalled DNA replication forks by the BRCA2 breast cancer susceptibility protein. *Genes & development* **17**, 3017-3022